Space Science Reviews (2021) 217:68
https://doi.org/10.1007/s11214-021-00838-3

The Relativistic Electron-Proton Telescope (REPT) Investigation: Design, Operational Properties, and Science Highlights

Daniel N. Baker[1] · Shrikanth G. Kanekal[2] · Vaughn Hoxie[1] · Xinlin Li[1] · Allison N. Jaynes[3] · Hong Zhao[4] · Scot R. Elkington[1] · John C. Foster[5] · Richard Selesnick[6] · Binbin Ni[7] · Harlan Spence[8] · Rachel Filwett[3]

Received: 3 September 2020 / Accepted: 17 June 2021 / Published online: 27 July 2021

Abstract The Relativistic Electron-Proton Telescope (REPT) instruments were designed to measure ∼2 to >18 MeV electrons and ∼18 to > 115 MeV protons as part of the science payloads onboard the dual Radiation Belt Storm Probes (RBSP) spacecraft. The REPT instruments were turned on and configured in their science acquisition modes about 2 days after the RBSP launch on 30 August 2012. The REPT-A and REPT-B instruments both operated flawlessly until mission cessation in 2019. This paper reviews briefly the REPT instrument designs, their operational performance, relevant mode changes and trending over the course of the mission, as well as pertinent background effects (and recommended corrections). A substantial part of this paper highlights discoveries and significant advancement of our understanding of physical-processes obtained using REPT data. We do this for energetic electrons primarily in the outer Van Allen belt and for energetic protons in the inner Van Allen zone. The review also describes several ways in which REPT data were employed for important space weather applications. The paper concludes with assessments of ways that REPT data might further be exploited to continue to advance radiation belt studies. The paper also discusses the pressing and critical need for the operational continuation of REPT-like measurements both for science and for space situational awareness.

Keywords Radiation belts · Particle sensors · Space weather · Situational awareness

1 Introduction

The Relativistic Electron-Proton Telescope (REPT) instruments were proposed as part of the complement of sensor packages to be flown onboard the Radiation Belt Storm Probes (RBSP) of NASA (see Baker et al. 2013a). The two REPT instruments were identical and were mounted respectively on the payload platforms of each of the twin RBSP-A and RBSP-B spacecraft. These satellites were successfully launched into nearly identical elliptical Earth orbits on 30 August 2012 (see Mauk et al. 2013). In November 2012, the

---

Van Allen Probes: Mission and Discoveries Through Earth's Inner Magnetosphere
Edited by Sasha Ukhorskiy, David Sibeck and Howard Singer

Extended author information available on the last page of the article

RBSP mission was renamed by NASA as the Van Allen Probes mission in honor of James Van Allen the discoverer of the Earth's radiation belts. The two REPT instruments (termed REPT-A and REPT-B) were turned on 2.5 days after launch and they each operated continuously (and flawlessly) until the cessation of mission operations in 2019 (Ukhorskiy et al. 2020).

The goals of the REPT sensors were to measure the high-energy ($E \gtrsim 1$ MeV) electron populations across the entire range of geocentric radial distances explored by the RBSP spacecraft ($1.1 \lesssim r \lesssim 5.8\ R_E$). The REPT electron detectors were designed to have the sensitivity and dynamic range to observe accurately the entire relativistic electron population with energies from 1 to ∼20 MeV under all solar and geomagnetic driving conditions. The REPT sensors were also designed to measure protons at all orbital locations in the energy range from ∼18 MeV to >115 MeV. As will be summarized in this review, the REPT sensors not only met but also, in many ways, greatly exceeded the expectations laid out in the original mission requirements (Baker et al. 2013a).

The challenges inherent in making clean and suitably accurate measurements of the very energetic electrons and protons in all parts of the Earth environment are formidable (see Baker et al. 2013a). REPT had to contend with (as do all particle sensors) proton contamination of electron channels (and vice versa) as well as pulse pile-up effects and bremsstrahlung backgrounds during the most active times. In addition, there can be significant dead-time effects for the differential rate channels as well, when the ambient intensities are high. Through careful design steps, detailed instrument modeling, and exhaustive laboratory calibrations prior to launch, the REPT instruments proved to be efficient and effective in measuring energetic electrons and protons with most of the aforementioned limitations substantially mitigated. Furthermore, the instruments also were able to be pushed well beyond their basic design modes to measure protons up to extremely high energies (e.g., Selesnick et al. 2018).

The fundamental goals of this paper are to: (1) review the basic design and in-practice operational performance of the REPT sensors over the entire mission lifetime (2012–2019); (2) identify the trends and mode changes that occurred over the course of the mission; (3) clarify the known background effects, and related corrections to be applied to the REPT data products; and (4) highlight the primary science discoveries and insights that were made using the REPT sensors. In the process of presenting results relevant to the preceding list of goals, we seek to provide pointers to interested readers about many of the hundreds of scientific and technical papers published using the REPT data thus far in the Van Allen Probes program. (Note that in the rest of this paper, RBSP and Van Allen Probes are used interchangeably).

2 Instrument Design and Function

The Relativistic Electron-Proton Telescope is a classic dE/dx energetic particle spectrometer (Table 1) comprising a stack of silicon solid-state detectors in a telescope configuration, a collimation aperture, and a thick case surrounding the detector stack to shield the sensors from penetrating radiation. Full details and description of the REPT instruments, science design considerations, and data are in Baker et al. (2013a). REPT measures high-energy electrons (1.8 to >18 MeV) and protons (∼18 MeV to >115 MeV) with better than 50 keV sensitivity (the ADC data number steps are within 50 keV).

The REPT instruments point perpendicular to the spin axis of the RBSP spacecraft and sample pitch angles in 36 sectors per spin. Measured fluxes are reported in dE/E ∼25% differential bins; 11 differential channels for electrons up ∼19 MeV and one higher integral

Fig. 1 Cross section of REPT showing the detector stack, collimator and the surrounding shielding (from Selesnick et al. 2018)

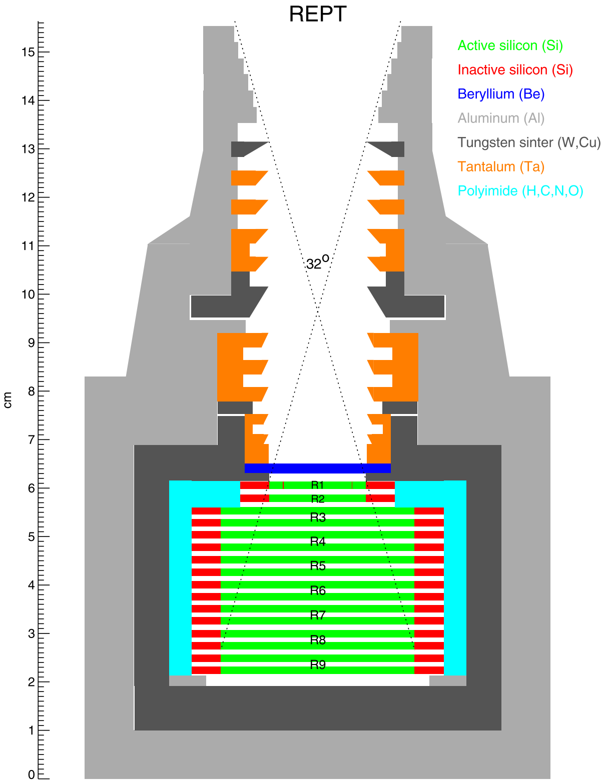

channel, and 7 differential channels for protons up to 115 MeV and an integral channel (>∼115 MeV). All channel counts are collected and reported on a spin sector basis.

A schematic representation of REPT is shown in Fig. 1. REPT has a large geometric factor of 0.2 cm^2-sr to obtain statistically significant counts at higher energies, and fast charge collection and electronics to support event rates up to 3.5×10^5 particles/s with correctable dead time and pileup correction above that flux level.

The REPT collimator is a high-Z material disk-loaded collimator design yielding a geometry factor of 0.2 cm^2-sr with a full-angle circular conical FOV (field-of-view) of 32°. At the back of the collimator there is a 2 mm thick beryllium (Be) window that excludes lower energy electrons (<1 MeV) and protons (<15 MeV).

The sensor shielding is made up of a 10 mm aluminum external housing and an inner 7 mm thick layer of sintered tungsten-copper alloy. This combination greatly reduces side penetrating electrons below ∼20 MeV and protons below ∼100 MeV while minimizing bremsstrahlung x-ray background.

The REPT sensor stack consists of 24 mm of silicon comprised of nine detector volumes, each detector volume is made up of one or more 1.5 mm thick ion implanted silicon detectors. The front two detector volumes are 1.5 mm thick and the back seven are 3 mm each (two 1.5 mm detectors back to back).

The charge left by energetic particles transiting the stack is collected from the detector volumes as a set of time correlated pulses. Charge Sensitive Amplifiers (CSA) attached to each detector element collect the pulses and feed a parallel fast trigger, and slower pulse shaped channels. Detection, pileup and digitization timing are based on the fast channels

Table 1 REPT on-orbit performance

Parameter		On-orbit performance	
Electron Energy Range		1.8 MeV to >18.9 MeV	
Electron resolution		25%	
Proton Energy Range		18 MeV to >115 MeV	
Proton resolution		30%	
Geometry Factor		0.2 cm^2-sr	
Field of View		32° (full angle)	
Integration cadence		1/36 of spacecraft spin ($\sim$1/3 s)	
Dead time losses		50% at 350 kilocounts s^{-1}, correctable to $<20\%$	
Dimensions		$11.8'' \times 11.6'' \times 9.8''$	
Mass		13.4 kg	
Power		6.2 W (operational)	
Data Volume	Science	1.3 kbps	1.3 kbps
	PHA	232 bps	10.8 kbps
	Housekeeping	11 bps	11 bps
		1.6 kbps @ launch	12.1 kbps after reserve release

while all nine of the slower channels are digitized simultaneously to produce a Pulse Height Analysis (PHA) data set (one for each valid energetic particle event).

Each PHA set represents the total energy left by the particle as well as the distribution profile in the detector stack. The process of classifying particle events by type and energy range proceeds by comparing the PHA values from individual detectors and PHA sums of select detectors against sets of energy bounds, with each set defining a species and energy bin. The energy bounding conditions are written as logic statements with multiple terms that, if all are evaluated as true, the count of the energy bin for that particle type is incremented.

The energy bin counts are tallied over each spacecraft spin into individual 36-per-spin sectors providing fine pitch angle discrimination. Sector counts are reported on a once-per-spin cadence. In addition to the energy bin data, the individual PHA data sets are also telemetered to the ground. Provided primarily as a method for verifying on-orbit energy binning, PHA reporting cadence was initially $\sim$2 per sec. In late-2013 the mission released reserved telemetry data volume at which point the PHA reporting cadence was increased to $\sim$90 per second. In addition pulse height values from each detector for 100 events are also telemetered down at a cadence of 12 ms (Baker et al. (2013a)). This increased PHA data availability then allowed detailed instrument performance analysis as well as substantially extended the energy range of measured protons (Selesnick et al. 2018).

The REPT instrument has on-board gain and offset correction for each detector channel. Correction values are uploaded from the ground, supporting uniform channel-to-channel responses and correcting any on-orbit performance shifts. An on-board calibration stimulus circuit provides charge pulses to selectable detector CSA inputs supporting tracking of electronics performance shifts. Late in the mission, it was detected that there had been a gradual decrease ($\sim$2% at end of mission) in the reported responses to the calibration signals. It was determined through a separate measurement channel, that the calibration signals themselves had decreased, most likely due to a radiation-induced shift in the gate voltage of a JFET analog switch. With this shift corrected, there were no discernible gain or offset changes in detector channel responses of either REPT instruments over the remaining ∼5 yr Van Allen Probes mission.

In order to support higher pileup-free singles event detection rates, the front detector is split into two equal areas, i.e. a bulls-eye type configuration, with individual electronic signal chains. The fast trigger channels on each have dead times of ∼200 ns, defined by the detector charge collection rates, supporting counting rates above 4×10^5 per sec with less than 10% pileup. Combining the singles counts rates from the two front detector areas gives a very good determination of actual REPT particle rate. The slower PHA channels are paralyzable but pile-up free with dead times dictated by the FPGA timing at 1100 ns, giving less than 50% pileup at 4×10^5 counts per sec. The slow channel rate is related to the actual rate by the pile-up free form of the counting rate equation $m = n\,e^{-2nt}$ where m is the measured rate and n is the actual rate and $t = 1100$ ns is the channel dead time (Knoll 2010), allowing simple differential rate correction on a spin-sector basis.

As is evident from the sections below highlighting science results from REPT, the instrument design and functionality have been proven to be highly effective and have enabled significant and far-reaching science contributions and discoveries.

3 Calibration & Validation

The REPT instrument design and performance was modeled in GEANT4 and early development testing at proton and electron accelerators was used to verify efficacy of shielding, field of view, and performance.

REPT calibration was done both at the level of each individual detectors as well as at the instrument level for the two flight models (FM) as well as for the engineering model (EM).

Each detector was calibrated using a tri-nuclide alpha source (5.15, 5.48, and 5.80 MeV) in vacuum with charge injection to establish the ADC-to-MeV relationship. The results showed excellent linearity over the entire collected energy range and established gain and offset correction values for each channel.

The two flight units, FM-A and FM-B, as well as the EM, were tested and calibrated together at both proton and electron accelerators. Proton beam tests from beam energies up to 58 MeV were carried out at Crocker Nuclear Laboratory at UC Davis. At the Indiana University Cyclotron Facility (now closed) testing was done for energies above 58 MeV. Electron test data above ∼2.6 MeV were collected at the Idaho Accelerator Center. After delivery of the flight-units, data for electron energies below 2.6 MeV were collected using the EM at the Aerospace Corporation beta spectrometer facility. The beam tests at electron and proton accelerators enabled experimental measurement of efficiencies of differential channels as modeled by the Geant4 simulations. Just prior to the launch at the NASA Kennedy Space Flight Center, the REPT instruments were oriented to collect atmosphere-generated muons and the data were successfully used to verify the REPT geometry factor. REPT instruments collected muons for a specific duration of time and the geometry factor was calculated using the observed number of counts and the known incident flux of atmospheric muons at sea level (e.g., Motoki et al. 2003).

Figures 2 and 3 show the results of accelerator calibrations for electrons and protons, respectively, compared to GEANT4 predicted efficiencies. The EM, FM-A and FM-B are all in good agreement with each other and the GEANT4 results. Note that, in order to avoid pileup during electron testing it was necessary to run at the very threshold of the LINAC dark current settings. At lower energies for this accelerator, we found the count rates and reported

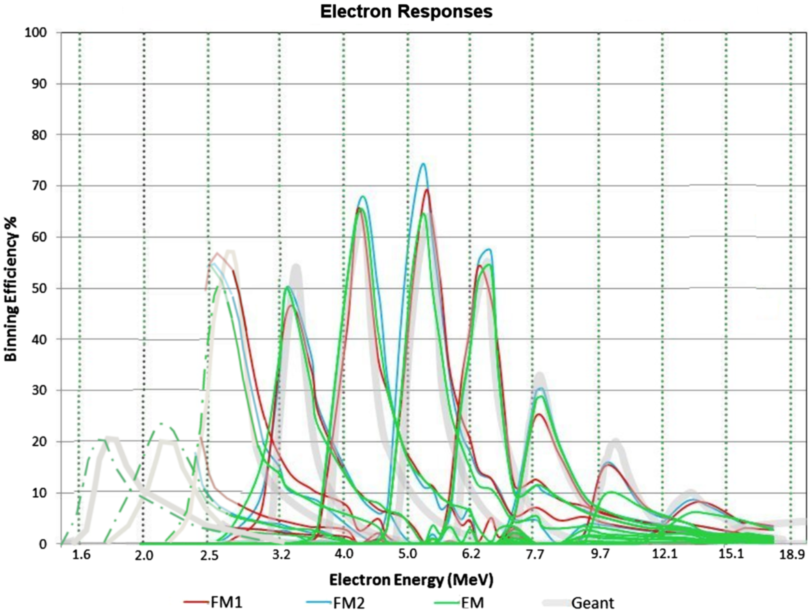

Fig. 2 REPT electron differential channel efficiencies as measured (at-beam) and from GEANT4 simulation. Responses below ∼2.5 MeV were corrected and verified at the Aerospace Corporation El Segundo CA, beta spectrometer using the cross calibrated REPT engineering model

Fig. 3 REPT proton differential channel efficiencies as measured and from GEANT4 simulation

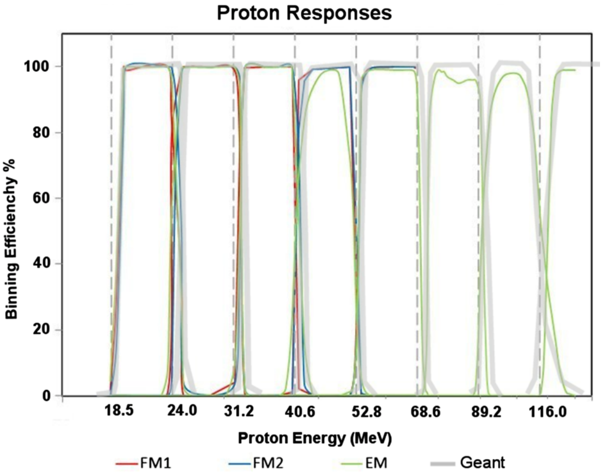

energies unreliable. In April 2013 the REPT engineering unit was taken to the Aerospace Corporation in El Segundo CA and calibrated using their ^{90}Sr/Y beta spectrometer. This cross-calibration exercise with the MagEIS high instrument allowed us to correct the lower energy REPT electron response.

As described earlier, the fast response of the REPT singles channels, combined with the deterministic timing of the PHA sampling channels was designed to support excellent counting rate determination and dead-time correction. Following delivery of the flight units

Fig. 4 Measured counting rates and dead times for REPT singles detection and captured PHA events

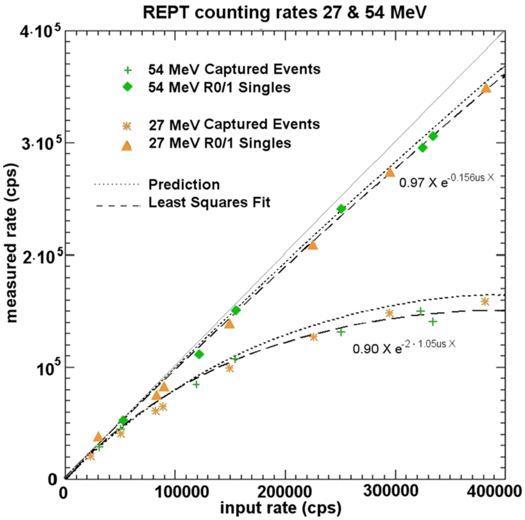

to the spacecraft, the engineering model was taken back to IUCF in Indiana where the REPT counting response was verified for protons. Technical limitations of LINAC operation prohibited electron rate measurements of this type. Since instrument count rates are defined by detector charge collection times and electronics responses, it is believed proton and electron detection rates and dead times are comparable. Figure 4 shows REPT reported front detector singles and captured PHA events over a range of incident event rates. The recorded performance is in close agreement with predictions across the entire range of input rates.

4 Operational Trends & Mode Changes

4.1 Operational Trends

The trending of REPT instrument performance parameters on board the Van Allen Probes were remarkably stable over the lifetime of the mission. Most housekeeping parameters showed expected variation and trending, such as temperature shifts. The only anomaly was a stepwise increase in the leakage current of one detector (Detector 9) on RBSP-B, identified just after launch. While the team anticipated this might necessitate changes in the detector noise threshold and potentially the energy binning equations later in the mission, no action was ever required. Note that leakage currents on all detectors onboard the RBSP-B spacecraft were higher than on RBSP-A due to elevated spacecraft temperature. Figure 5 shows the leakage current for Detector 9 in orange, riding above the other eight detectors (R0 and R1 together constitute the front detector). The higher rate of increase was evident starting shortly after instrument operations began but leveled off during subsequent years. Again, no action was required or taken due to this anomaly. Figure 6a shows the additional electronics noise present on Detector 9, in data number (or digital number), compared to the other eight detectors. The relevant curve relating ADC to MeV is given in Baker et al. 2013a. These noise levels were considered acceptable throughout the mission (see Fig. 6b) and did not initiate any changes to the binning logic.

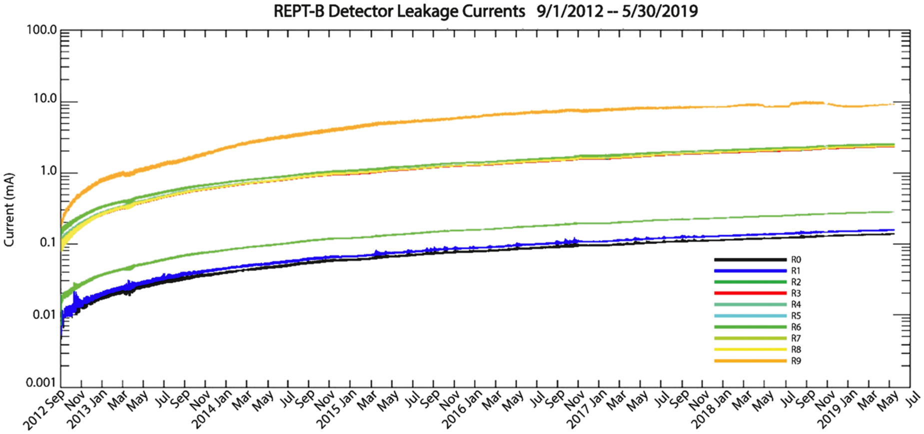

Fig. 5 Leakage currents on all nine detectors on RBSP-B over the mission lifetime. The orange trace represents Detector 9

Table 2 Summary of changes to the REPT instruments onboard Van Allen Probes A & B. The dates reflect the date that the change upload was sent to the MOC

Date	Change	Notes
September 27, 2012 18:20 UT	Changed equation 0 (first electron equation)	Not obvious in spin-averaged data
July 2, 2013 20:48 UT	Changed electron equations 2 and 3 to exclude high-energy proton contamination	Clearly seen in the spin-averaged electron data for the 2.6 and 3.4 MeV channels beginning early July 2013
May 21, 2015 21:54 UT	Changed proton equations	Clearly seen in the spin-averaged proton data; changed to reduce GCR background in binned energies

4.2 Mode Changes

The REPT instrument equations that determine onboard how each observation was counted in an energy channel were changed only three times during the lifetime of the Van Allen Probes. Table 2 summarizes these changes, noting the date, the change made, and any notes associated with the change. The date shown indicates when the change took effect onboard the spacecraft, and thus the time after which the data might show a change. Some of these changes are quite evident in the spin-average data in various energy bins. We note this, where applicable, so that any sudden features uncovered in the data can be checked against this table.

In early 2015, the REPT team made the decision to change the bow tie analysis being used to define the energy channel centers and boundaries. The team had originally used the so-called "Van Allen/Baker" bow tie method (Van Allen et al. 1974) but switched to the "Selesnick/Blake" bow tie method (Selesnick and Blake 2000) to align with the practices of the MagEIS instrument team and aid in cross-calibration efforts. All public data has been reprocessed to use the "Selesnick/Blake" bow tie method. Table 3 lists the differential channel definitions using both methods.

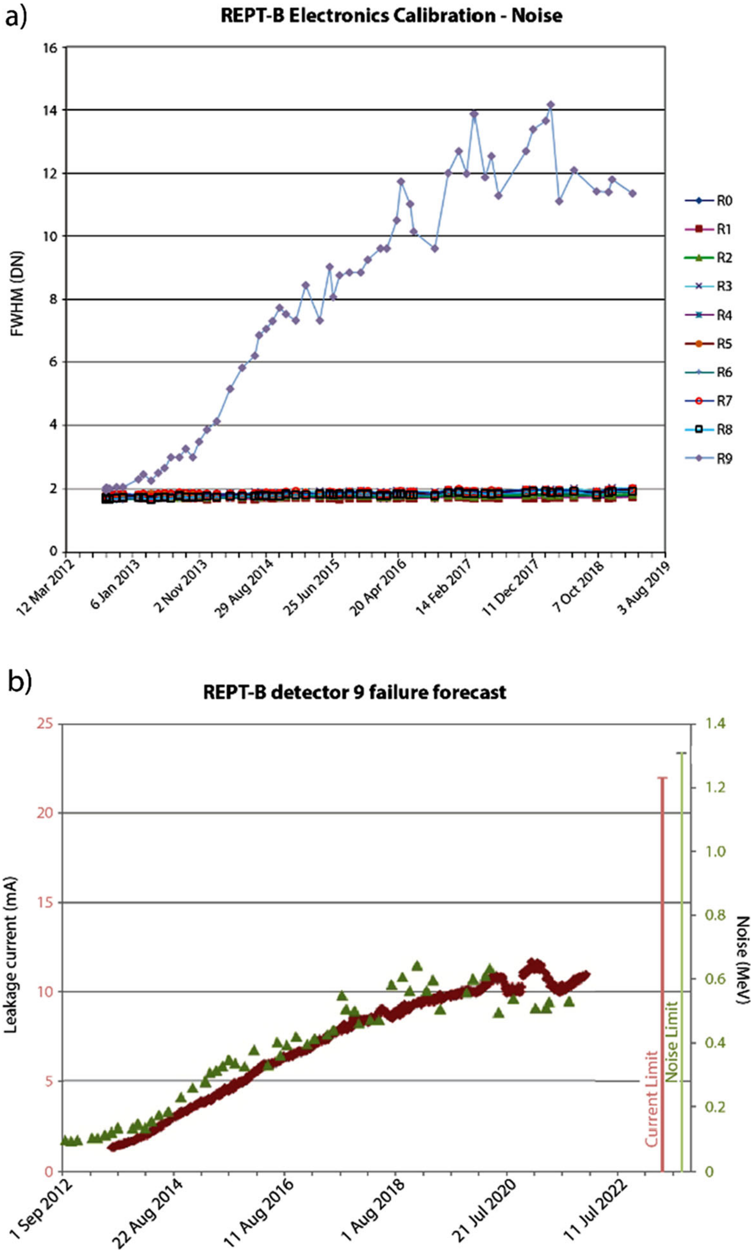

Fig. 6 (**a**) Noise level, in data number, for all detectors over time. The gray diamonds represent Detector 9 (DN = 38 keV); (**b**) REPT-B Detector 9 failure forecast determined that no action would be required until approximately 2022

This change only affected *energy channel definition labels* as contained in the publicly available CDF data files. There was no change to the actual instruments onboard (e.g., differential channel logic) as a result of this decision. Therefore, the change was applied retroac-

Table 3 Differential channel characteristics of REPT for the Van Allen/Baker and the Selesnick/Blake methods. The bow tie efficiencies were calculated for power law spectra indices of -2, -3, -4, -5 and e-folding energies of 0.2, 0.4, 0.6, 0.8, and 1.0 MeV

Van Allen/Baker (power law)			Selesnick/Blake (power law)		Selesnick/Blake (exponential)	
Nominal channel	Effective efficiency $\langle\eta\rangle$	Bow tie bin (MeV)	Bow tie Energy $\langle E\rangle$ (MeV)	Bin width δE (MeV)	Bow tie Energy $\langle E\rangle$ (MeV)	Bin width δE (MeV)
1.6-2.4	0.070	1.6-2.2	1.9	0.11	1.8	0.09
2.0-2.5	0.162	2.0-2.5	2.2	0.16	2.1	0.13
2.5-3.2	0.364	2.5-3.2	2.8	0.51	2.6	0.35
3.2-4.0	0.322	3.2-4.0	3.5	0.49	3.4	0.41
4.0-5.0	0.574	4.0-5.0	4.4	1.10	4.2	0.85
5.0-6.2	0.450	5.0-6.4	5.6	1.24	5.2	0.75
6.2-7.7	0.380	6.2-8.1	6.9	1.45	6.3	0.70
7.7-9.7	0.265	7.7-9.9	8.5	1.16	7.7	0.52
9.7-12.1	0.132	9.7-13.6	11.2	0.97	9.9	0.30
12.1-15.1	0.079	12.1-18.6	14.1	0.93	12.3	0.17

tively to all CDF files prior to 2015. REPT data users are cautioned not make use of files from before 2015 that were downloaded to a local machine prior to mid-2015. To update the energy channel labels, users must again download any data prior to mid-2015 from the Project Gateway, ECT data portal served by the New Mexico Consortium, or CDAweb.

5 Background Effects & Corrections

Main sources of background for REPT include side-penetrating particles, galactic cosmic rays (GCR) and mis-identified particles. The latter can be, for example, protons classified as electrons and "out of bin" particles. Another source of background can be bremsstrahlung photons from high-energy particles striking the REPT sensor shielding. Corrections to measured raw particle counts include corrections for dead time and pile up. Post-processing corrections are applied to account for protons being classified as electrons. Due to the fact that protons deposit larger amount of energy in detectors (dE) than electrons, it is somewhat rare (except in the inner zone as discussed below) that electrons are classified as protons.

Two aspects of REPT design help reduce the background due to side-penetrating particles, bremsstrahlung, and GCR. These include the dual material shielding comprising inner tungsten-copper alloy and outer aluminum. The outer Al shielding prevents protons <110 MeV from entering the SSD stack, while bremsstrahlung photons are absorbed by the high-Z tungsten layer. Only about 0.01%(1%) of electrons of energy 10(30) MeV enter the stack (see Fig. 25 of Baker et al. 2013a). Extensive studies carried out using Geant4 with complete instrument geometry have shown that these backgrounds are negligible. Additionally, these studies were complemented with the flight and engineering models exposed to high-energy proton and electron beams at accelerator facilities (Sect. 3, Calibration and Validation).

The second important aspect of the REPT design that helps reduce these backgrounds is the use of multi-detector coincidence and vetoes from the detector stack for the differential channels. The differential channels not only rely on logic conditions that use energy deposition patterns in multiple detectors but also require a trigger of sequential detector hits within a short coincidence window of 250 ns.

The scientific findings and discoveries made using REPT data, highlighted in the following sections, have amply confirmed the robust and mostly background free nature of the data. However, cross comparisons between MagEIS and REPT spectra have shown a discrepancy, in the overlapping energy regions of the two instruments. This discrepancy is likely due to the incorrect application of bin efficiencies applied to the REPT dataset during ground processing. The upcoming release of the data files will include the corrected bin efficiencies as well as the background correction described next. This correction will not completely address the discrepancy between MagEIS and REPT, particularly during changing overall counting rates in the two instruments, but it will bring the REPT spectra more in family with MagEIS spectra on average. It must be noted that the bin efficiency discrepancy was uniform across all bins and did not affect any spectral breaks, but only absolute values, which does not affect the science results. The REPT and MagEIS teams continue to fine tune any effects that lead to spectral discrepancies and updated Level-2 data are released as the corrections are improved. Note that combined data covering electron energies from 15 eV to 20 MeV, using data from HOPE, MagEIS and REPT instruments comprising the ECT suite, incorporates MagEIS background corrections and is available at 3-minute resolution (Boyd et al. 2019).

It is well known that the inner zone is comprised mostly of protons. Due to their high intensities, some of these protons are misidentified as electrons and populate REPT electron differential channels. Recently, a correction algorithm was developed by examining the energy and pitch angle summed totals of both protons and electrons for each spacecraft's pass through the inner zone (Filwett, private comm.). Full details of the correction algorithm will be described in a forthcoming publication. The need for data-based correction resulted from the fact that Geant4 studies showed the background to be very small ($\ll 1\%$) while in-situ measurements indicated it to be at a level of a few percent outside of $L=2.8$ and much higher within the high-energy proton belt. The corrected data will be available as a distinctly named variable in the CDF files, in addition to the existing REPT data, and their usage is left to users' discretion. Figure 7 shows 1.6-2.0 MeV electron counts for a three-day interval during the year 2015. The top panel shows the uncorrected counts, and the bottom panel shows the background corrected data.

6 Science Highlights: Outer Zone

As noted in the preceding sections of this paper, the REPT-A and REPT-B instruments were both turned on and configured in their normal operating modes on 1 September 2012. This commissioning and establishing of full science operations for the REPT packages was several weeks ahead of the nominal instrument commissioning phase that had been planned for REPT. However, the early turn on of the instruments was undertaken in order to maximize the temporal overlap of REPT data collection with the Solar, Anomalous, and Magnetospheric Particle Explorer (SAMPEX) mission (Baker et al. 1993). SAMPEX was destined to re-enter Earth's atmosphere in the autumn months of 2012 due to satellite drag effects (Baker et al. 2012).

In this section we will describe several of the earliest science results from analysis of REPT data. This includes unique features associated with highly relativistic ($1 \sim 2$ MeV)

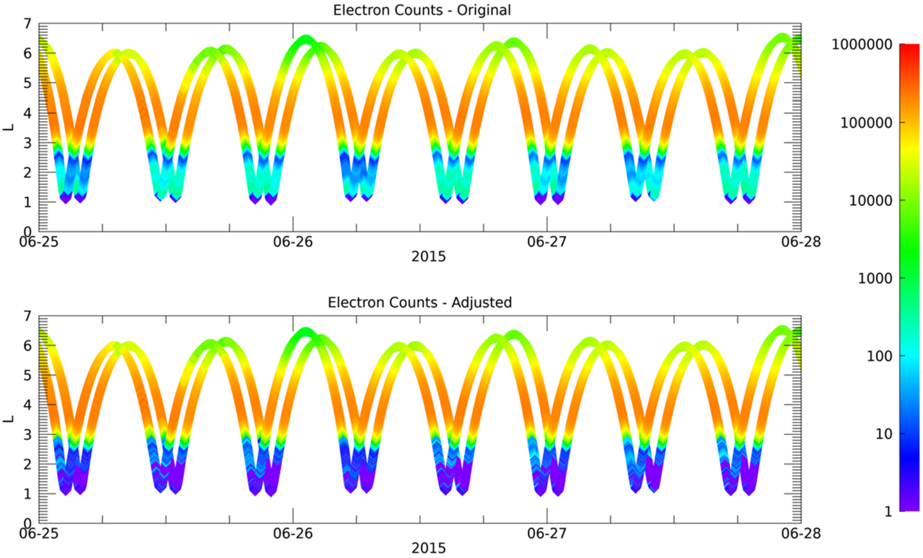

Fig. 7 The in-situ, uncorrected, electron counts for 1.6-2.0 MeV are shown (top panel) along with the corresponding background corrected (bottom panel) electron counts for June 25-27, 2015. The correction algorithm is applied to $L < 2.8$ and uses an observed electron-proton relationship to subtract electron counts caused by penetrating particles. The correction algorithm removes nearly 2 orders of magnitude of background while leaving intact orbit-to-orbit variations

electrons as well as the ultrarelativistic electron population ($3 \sim 10$ MeV) in Earth's magnetosphere. This section will focus largely on the outer (Van Allen) radiation zone that stretches from roughly 3 to about 7 Earth radii in equatorial geocentric distance. We will note some of the novel findings of the Van Allen Probes mission with respect to radiation belt morphology, temporal trends, acceleration and loss characteristics, and evident transport of energetic electrons. The latter kind of transport is due both to radial diffusion as well as prompt compressional effects associated with coronal mass ejection (CME) forcing events and interplanetary shock impacts.

We note explicitly here that many of the discoveries made with the REPT instruments and insights obtained with these sensors were only possible because of the comprehensive suite of instruments that were part of the RBSP payloads. The magnetic field data (Kletzing et al. 2020), plasma wave measurements plus electric field information (Breneman et al. 2020), and the comprehensive low (Skoug et al. 2020; Gkioulidou et al. 2020) and medium (Claudepierre et al. 2020) energy particle data from each RBSP spacecraft allowed the very energetic electron and proton data of REPT to be put into its proper geophysical context. This complete sweep of particle and field information (Manweiler et al. 2020) from the dual RBSP spacecraft was and remains the great and enduring legacy of the Van Allen Probes mission (Ukhorskiy et al. 2020).

6.1 Outer Belt Morphology

Figure 8 shows color-coded flux information for the 4.0-5.0 MeV channels for REPT-A and REPT-B combined for the period 1 September through 16 October of 2012. The horizontal axis is the time scale and the vertical axis is effectively radial distance from Earth center (here shown as the L^* parameter). The color scale shown to the right side of the figure is a

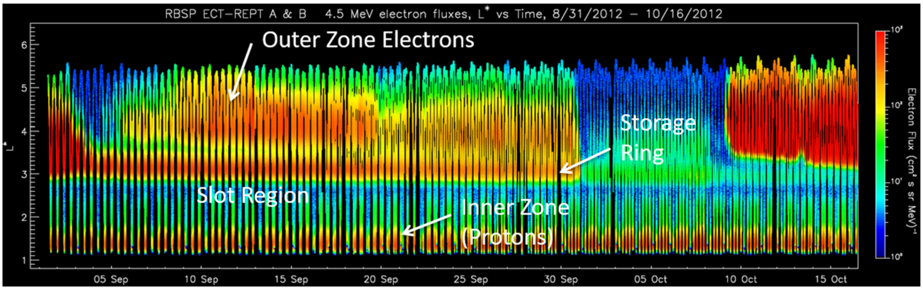

Fig. 8 Combined REPT-A and REPT-B measurements of ultra-relativistic electron intensities ($E = 4.5$ MeV) during September and October 2012. The time is indicated along the horizontal axis and the electron intensity scale is indicated by the color bar to the right of the panel. The various regions of the radiation belts are labeled in the figure. This is adapted from Baker et al. (2013b) and represents the discovery image for the relativistic electron "storage ring" or third Van Allen belt

logarithmic representation of the differential flux of the 4-5 MeV electrons (electrons/cm2-s-sr-MeV). Fortuitously, the REPT instruments were switched on during the height of a strong relativistic electron enhancement event (1-4 Sept.). The electrons were enhanced across a broad radial range ($2.8 \lesssim L^* \lesssim 5.0$) at the start of the data acquisition. However, fluxes diminished across much of the outer radiation belt by 5 September leaving a band of intense electron fluxes over the range of $2.8 \lesssim L^* \lesssim 3.4$. As described by Baker et al. (2013b) in the discovery paper of the phenomenon, this relativistic electron "storage ring" or "third" Van Allen belt could persist for days or weeks at a time. In the case shown in Fig. 8, the storage ring lasted for some four weeks until it abruptly dissipated on $\sim$ 1 October 2012.

Figure 8 shows that the magnetosphere has an inner zone (comprised mostly of very energetic protons and low energy electrons of $<\sim$ 700 keV), a "slot" region around $L \sim 2.5$, and an outer belt that is complex, often consisting of the storage ring relatively closer to the Earth embedded in a highly variable outer Van Allen zone proper. Baker et al. (2013b) noted that this storage ring structure was probably a remnant of strong electron acceleration and Earthward transport often left intact until an IP shock or CME event dissipated the storage ring.

Figure 8 demonstrates that a strong acceleration event must have occurred sometime before the RBSP launch in late August of 2012. The figure also shows a very strong acceleration event that occurred on $\sim$ 10 October 2012. This event was described in detail by Reeves et al. (2013) and it showed that electrons often may be accelerated deep within the outer radiation belt ($L \sim 4.0$) by strong wave-particle interaction processes. These acceleration events often produce multi-MeV electrons across much of the outer zone on short timescales (Reeves et al. 2013; Thorne et al. 2013b; Foster et al. 2014; Baker et al. 2014a).

Examination of long runs of REPT data revealed the common occurrence of the three-belt structure described by Baker et al. (2013b). Figure 9 from Baker (2014) shows more REPT data ($\sim$4.5 MeV) extending from 1 September 2012 to 1 July 2013. Obviously, in periods such as September 2012, March 2013, and April-May 2013 the multiple belt configuration was often clearly displayed. The diagram to the left side of Fig. 9 turns the radiation belt diagram "on its side" to drive home the morphological reality that the canonical "two-belt" structure usually portrayed in the textbooks has had to be revised in light of the better spatial, temporal, and energy resolution data from the REPT/RBSP data. Over the course of the Van Allen Probes lifetime, numerous theory and modeling papers (e.g. Shprits et al. 2016;

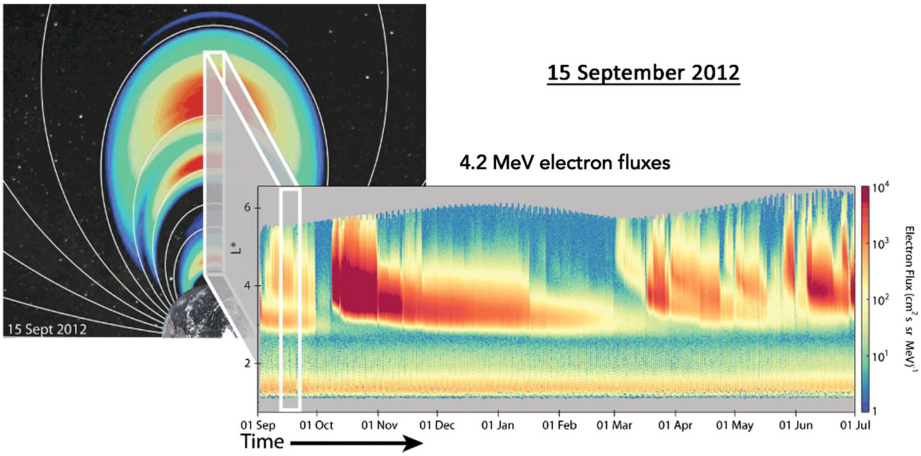

Fig. 9 A 10-month-long plot of electron fluxes ($E = 4.2$ MeV) from the REPT-A and -B instruments on board the Van Allen Probes shows large increases and rapid losses of particles that occur on abrupt time scales. The plot to the left represents an image of the distribution of particles in a cross-section of the Van Allen belts. The flux of electrons is measured in units of particles/cm^2-s-sr-MeV according to the logarithmic color bar. (From Baker (2014))

Mann et al. 2016) have addressed how and why the multiple belt structure exists in the magnetosphere.

Another portrayal of the outer belt structure and how rapidly it changes came from a study by Baker et al. (2019a). Examining in detail the acceleration event in mid-March of 2013 shown above in Fig. 9 (see Foster et al. 2014 and Baker et al. 2014a), Baker et al. (2019a) used a polar-view projection of the data as shown here in Fig. 10; i.e., the authors used in situ REPT measurements along the elliptical trajectory of the RBSP spacecraft. Baker et al. recognized that multi-MeV electrons drift around the Earth on essentially dipolar magnetic field drift paths and they do so much faster than the spacecraft move across the L-shells. Thus, it is reasonable to map the fluxes measured along the spacecraft track all around the Earth to give a picture (from a top or polar view) of the entire radiation belt electron population.

In Fig. 10, the data for an event period (March 2013) are shown: (a) just shortly before the CME and related shock wave hit the magnetosphere (17 March 2013); (b) just shortly after the CME/shock hit the magnetosphere (about 9 hours later on 17 March); and (c) another RBSP orbital period later ($\sim$2300 UT on 17 March) when the radiation belt was replenished. From this sequence of images (or radiation belt maps), Baker et al. (2019a) noted that before the CME/shock impact there was a clear pattern of the outer belt separated from the storage ring feature near $L \sim 3.0$. Right after the shock wave struck the magnetosphere the outer part of the Van Allen belt was stripped away leaving only the storage ring. Just a few hours later (panel c), the entire outer belt was powerfully regenerated and restored to much higher fluxes than had been present before the CME impact.

Figure 11 is a composite of the three separate times shown in Fig. 10 placed together in one image (also taken from Baker et al. 2019a). This shows how persistent the storage ring around $L = 3.0$ can be even as the rest of the outer zone undergoes huge flux changes.

Yet another morphological feature is evident from all of the Figs. 8-11, namely, that the outer zone high-energy electrons extend inward toward the Earth to about $L = 2.8$, but never

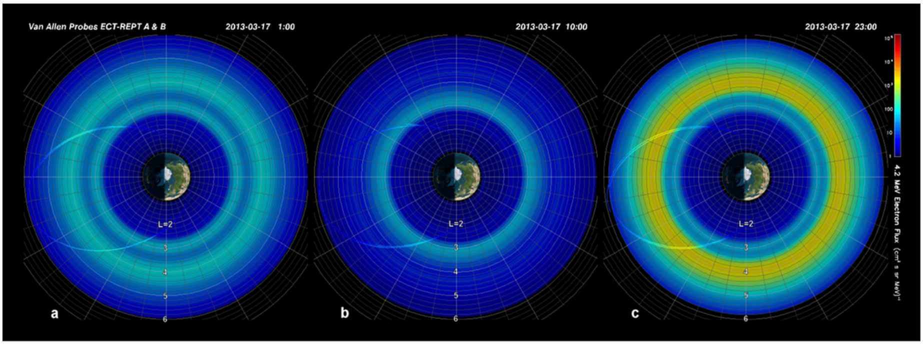

Before IP Shock Right After Shock Half Day Later

Fig. 10 Polar view, color-coded plots of electron fluxes for the 4.2-MeV channels of REPT for 17 March 2013. (**a**) Pattern for ∼0100 UT. (**b**) For ∼1000 UT. (**b**) For ∼2300 UT for times shown. The plot shows outer belt structure before, right after, and a few hours after a CME impact on the radiation belt electron population. (From Baker et al. 2019a)

Fig. 11 Merged polar plots for 4.2-MeV channel for 17 March 2013 comparing the several periods shown in Fig. 10. (From Baker et al. 2019a)

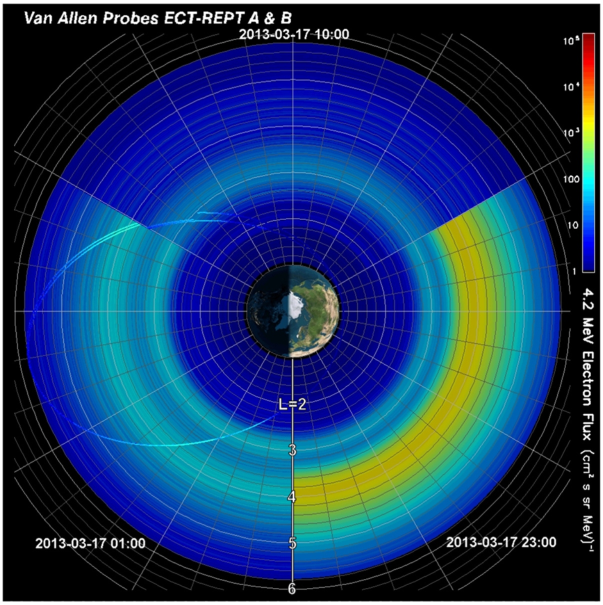

(during the RBSP lifetime) closer. This was termed “the impenetrable barrier” by Baker et al. (2014b). Figure 12 from that paper shows $E \sim 7.2$ MeV electrons for two separate several-week periods. The data show that the inner (or Earthward) edge of the outer belt stays fixed for days and weeks on end.

Baker et al. (2014b) speculated that this “impenetrable” barrier was mostly due to radial diffusion processes for the multi-MeV electrons slowing dramatically as high-energy electrons reached the radial distance near $L \sim 3.0$. However, Foster et al. (2016) added a fascinating layer to the story of the impenetrable barrier when they noted that the Earth is shrouded in an intense very-low frequency (VLF) “bubble” of plasma waves. As shown

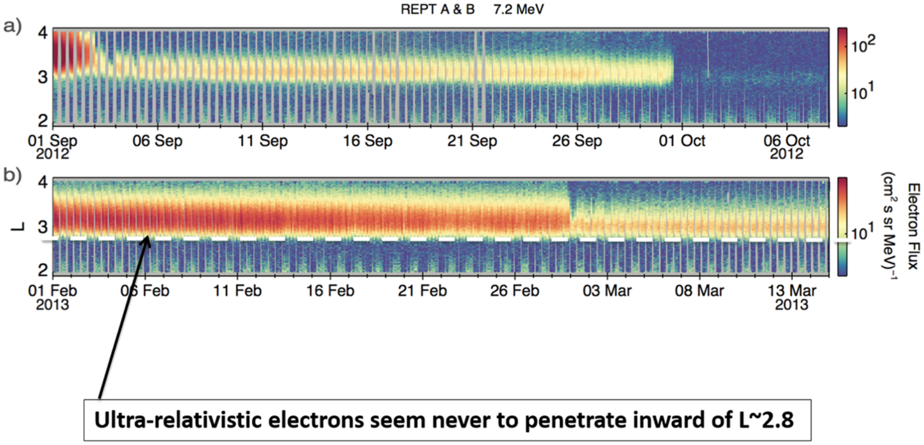

Ultra-relativistic electrons seem never to penetrate inward of L~2.8

Fig. 12 Color-coded electron flux data ($E = 7.2$) from the combined REPT-A and REPT-B sensors for two periods in the L vs. time format. The upper panel shows data for Sept.-Oct. 2012 and the lower panel shows data for Feb. – Mar. 2013. Both data show the sharp and persistent inner edge of the ultra-relativistic electron population termed the "impenetrable barrier". (From Baker et al. 2014b)

in Fig. 13 from Foster et al., the outer edge of the VLF bubble coincides closely with the location of the impenetrable barrier.

This has led to substantial theoretical work that the sharp inner edge of the outer zone electron belt (and storage ring) is controlled in important ways by VLF wave-particle interactions as seen in Fig. 14. The effects of VLF transmitter signals, wave-wave coupling, and chorus band suppression were discussed by Foster et al. (2016). Nonlinear acceleration by VLF chorus rising tones (cf. Sect. 6.4.3) is important to the local acceleration of MeV electrons outside the plasmapause (Foster et al. 2017, 2020; Omura et al. 2019).

A final note to be made is that when REPT electron channel backgrounds in the inner zone region due to inner zone protons are removed, there is no measurable flux of energetic electrons in the inner zone for electron energies $E \gtrsim 1.5$ MeV. This fact was driven home by careful analysis based on REPT and MagEIS data (Li et al. 2015b; Fennell et al. 2015; Baker et al. 2016a, 2018; Greeley et al. 2019). Thus, for the epoch 2012 to 2019, there were no highly relativistic electrons in the region $L \lesssim 2.8$. It should also be noted that STRV-1a and -1b, in a similar orbit as Van Allen Probes, had also observed various dynamic features of the outer radiation belt electrons (e.g., Daly et al. 1999; Desorgher et al. 2000; Iles et al. 2002).

6.2 Long-Term Trends

Due to the relatively benign solar cycle during which the Van Allen Probes operated, the two REPT instruments were able to obtain ∼7-year-long, high-resolution observations of the energetic radiation belt environment with no disruption or major degradation to the sensors. This allowed for a long-term look at the outer belt during mild solar wind conditions, punctuated with moderate geomagnetic storms. Figures 15, 16, and 17 depict the large-scale dynamics of 1.8 MeV, 4.2 MeV, and 7.7 MeV electrons respectively over the lifetime of the mission.

Many different features previously reported upon are clearly identifiable in these long-term plots, including: the impenetrable barrier near $L = 2.8$ (Baker et al. 2014b); the remnant belt structure first identified in October 2012 (Baker et al. 2013b) but since observed

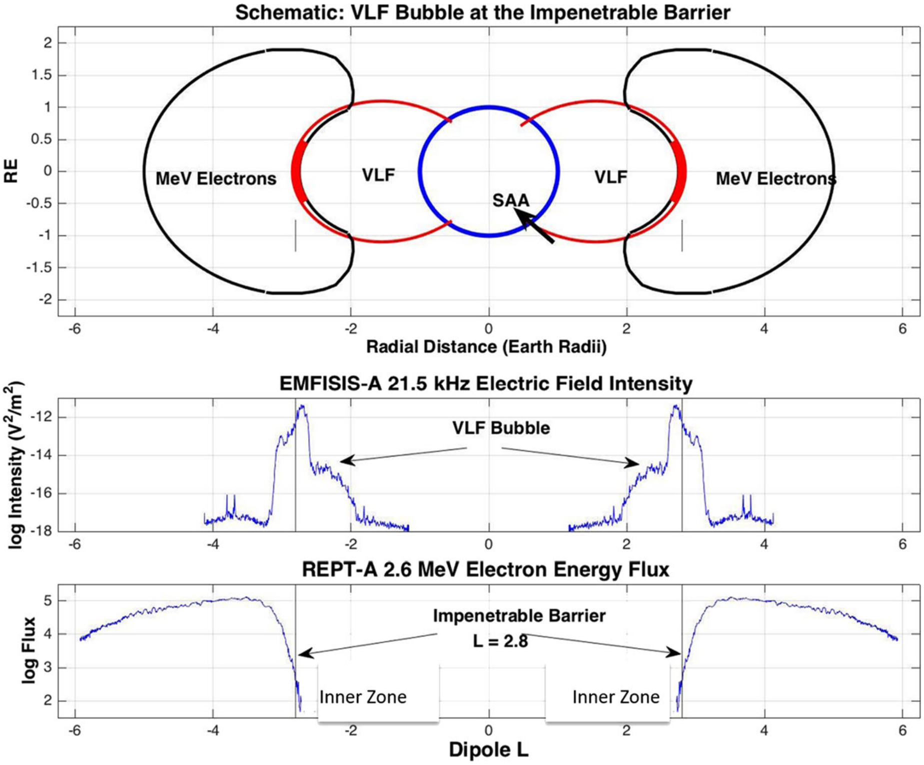

Fig. 13 Schematic representing the overlap of the inner edge of the electron radiation belt with the strong VLF transmitter signals at the outer edge of the VLF bubble in the region surrounding Earth. The L-space profiles of VLF transmitter signal intensity and 2.6 MeV electron flux observed during the 18 March 2015 event are shown. (After Foster et al. 2016, Fig. 8)

multiple times throughout the mission (Pinto et al. 2018); and numerous sudden flux-dropouts of high-energy particles down to very low L-shells (Turner and Ukhorskiy 2020). Figure 17, showing very few events comprising 7.7 MeV electrons, is especially striking and illustrates how unique the solar-driving was during this past solar cycle.

Zhao et al. (2017) investigated the correlation of various solar wind parameters and geomagnetic indices with radiation belt electron phase-space density (PSD) and PSD enhancements at a range of μ values and L-shell values. The study found that energetic electrons were most highly correlated with the AL index, a proxy for substorm activity. Figure 18, from Zhao et al. (2017) shows the results of the correlation study for the SYM-H (geomagnetic storm) index (panels a-b) and the AL index (panels c-d). Panels on the left show the time lag for a PSD enhancement and panels on the right show the highest correlation coefficient. Panel d clearly shows a cluster of higher correlation coefficients for high μ values, revealing a connection between acceleration of ultra-relativistic electrons and substorm activity.

6.3 Plasma Boundary/Electron Relationships

The plasmasphere, the cold, dense plasma population corotating with the Earth and located predominantly at low L-shells, has been shown to be closely correlated with the morphol-

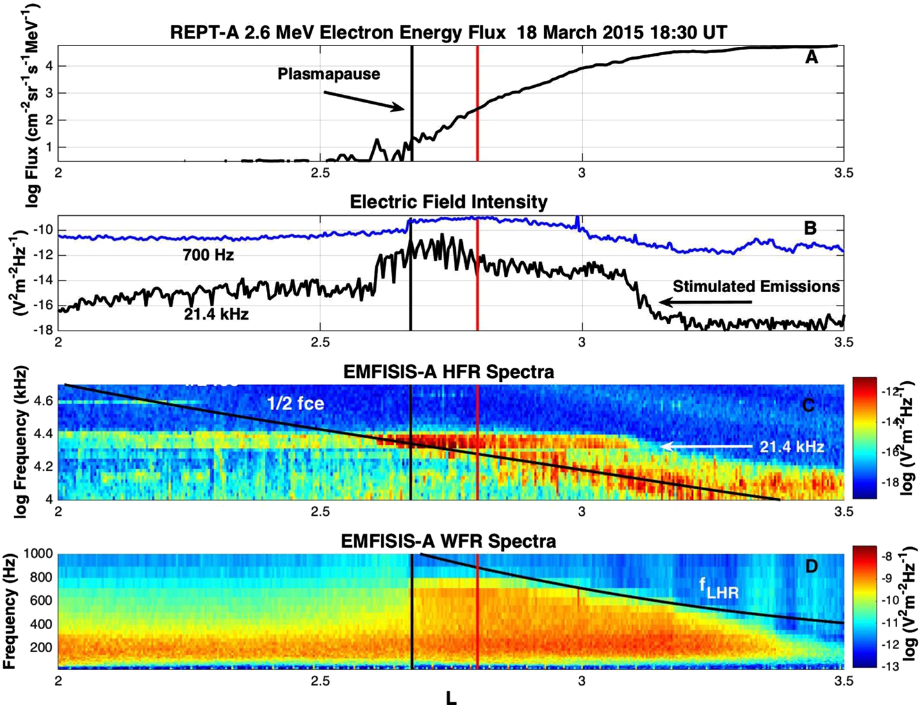

Fig. 14 A composite picture is shown of the interrelationship plasma waves at the outer edge of the VLF bubble and the 10,000x decrease in REPT 2.6 MeV electron flux between $L \sim 3.2$ and $L \sim 2.8$ during the 18 March 2015 event (after Foster et al. 2016). $L = 2.8$ is indicated by the vertical black lines and the plasmapause location marked in red. Amplification of a 21.4 kHz VLF transmitter signal outside the plasmapause and the suppression of VLF chorus band emissions below the transmitter frequency are noted

ogy of the radiation belts (Baker et al. 2004; Goldstein et al. 2005; Li et al. 2006). For example, Baker et al. (2004) examined the dynamical changes in the radiation belts during the so-called "Halloween solar storm", noting the concurrent inward motion of both the plasmapause and the inner edge of the outer radiation belts in response to the compression and subsequent geomagnetic activity induced by this event. Li et al. (2006) noted that an energy-dependence for the relationship between plasmapause location and outer zone radiation belts held most strongly during the main and recovery phases of a geomagnetic storm.

There are myriad physical mechanisms that may contribute to this correlation between the plasmasphere and outer zone radiation belt. They include wave-particle scattering by chorus mode hiss (Thorne et al. 1973; Meredith et al. 2006; Ni et al. 2013; Zhao et al. 2019), electromagnetic ion cyclotron (EMIC) waves (Millan and Thorne 2007; Summers et al. 2007; Su et al. 2017; Tetrick et al. 2017); plasma waves associated with electron energization include whistler-mode chorus wave (e.g. Horne et al. 2005; Li et al. 2007; Thorne et al. 2013b; Foster et al. 2017), fast-mode Alfven waves (Li et al. 1993; Hudson et al. 1997), and Alfven waves at mHz frequencies (e.g. Elkington et al. 1999, 2003; Hudson et al. 2000). The propagation and trapping of this variety of plasma waves are affected by the plasma density, e.g., plasmasphere (e.g. Claudepierre et al. 2016; Li et al. 2016c; Ren et al. 2018; and Goldstein et al. 1999; Yu et al. 2019; Yuan et al. 2017).

Plasmaspheric morphology is complex, and often complicates analyses of the plasmapause-outer zone relationship (e.g., Bruff et al. 2020; Malaspina et al. 2016; Goldstein et al.

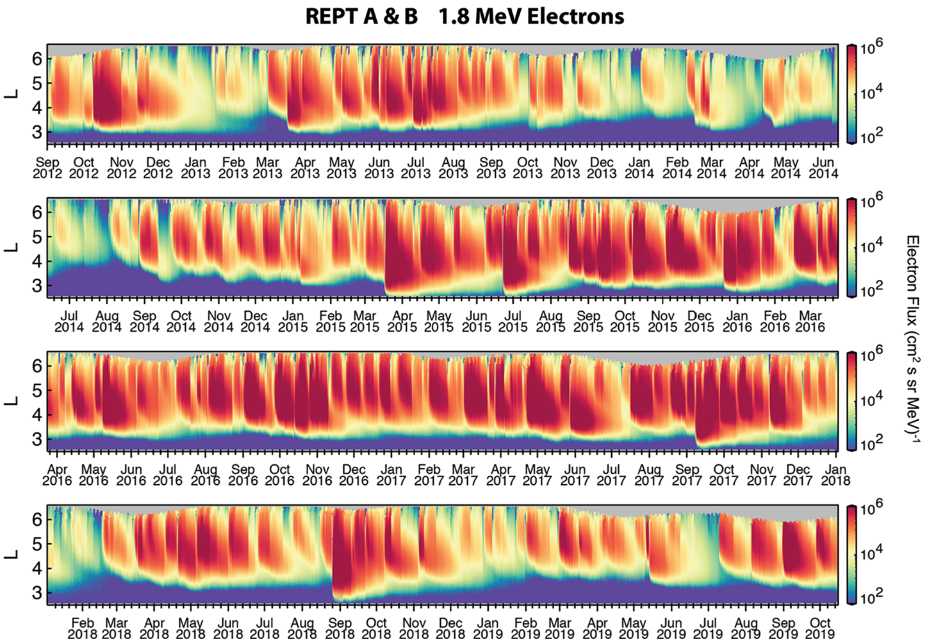

Fig. 15 1.8 MeV electron data from REPT-A and -B over the mission lifetime in L vs. time format (same color scale for each panel)

2005, 2014). Khoo et al. (2018, 2019) looked at a number of CME and CIR-driven geomagnetic storms that occurred over the Van Allen Probes era to examine the relationship between the minimum plasmapause location and the radial location of the initial enhancement of outer zone radiation belts. In these studies, they used two distinct models of the plasmapause location, those of Goldstein et al. (2014) and of Liu et al. (2015). Figure 19, from Khoo et al. 2019 shows evidence that the initial enhancements of energetic (30keV-2 MeV) electrons are persistently outside the innermost plasmapause location in either plasmapause model. They also suggested that energy-dependent processes dictated the distance between the plasmapause and outer zone locations, with lower-energy electrons (<200 keV) being driven inward primarily by enhanced magnetospheric convection, and higher-energy electrons being affected primarily by local acceleration via chorus waves. They noted a "turning point energy" that differed between CME- and CIR-driven storms: electrons below the turning point energy were consistently seen within 1 R_E of the innermost plasmapause location, with the distance from the plasmapause increasing with energy beyond the turning point to a maximum distance of $\sim 2\ R_E$.

A detailed examination of the radiation belt energy spectra by Zhao et al. (2019) and Ni et al. (2019) in the plasmasphere and near the plasmapause showed reversed energy spectra, with abundant high-energy and fewer low-energy electrons commonly existing inside the plasmasphere. Figure 20 shows the energy-dependent evolution of the energy spectrum many days after a magnetic storm in March 2015, with electrons of energy <2 MeV forming a bump-on-tail distribution and higher-energy electrons maintaining a kappa-like distribution. Fokker-Planck simulations indicated that the predominant mechanism for this unusual distribution was a result of electron scattering by hiss waves.

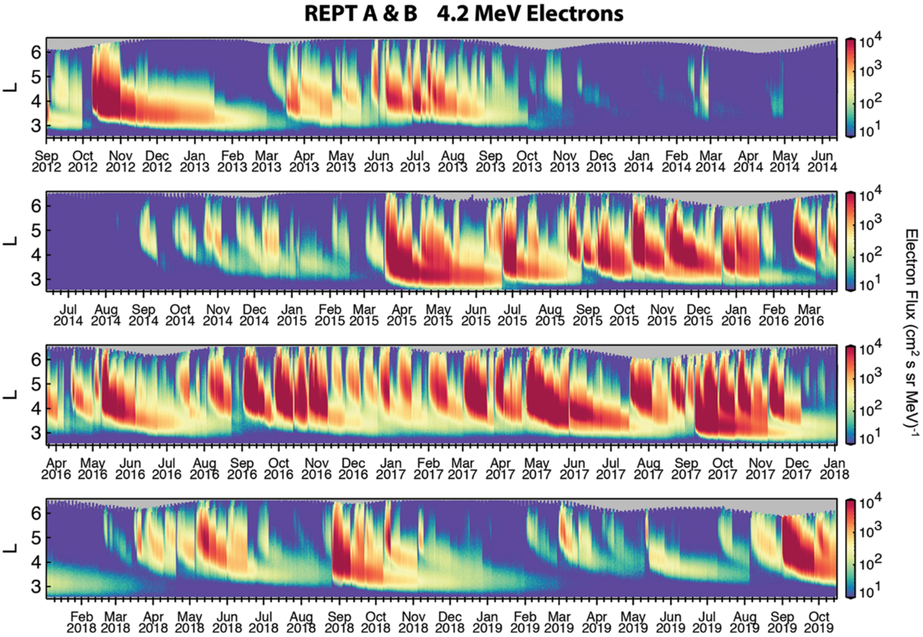

Fig. 16 4.2 MeV electron data from REPT-A and -B over the mission lifetime in L vs. time format (same color scale for each panel)

6.4 Electron Acceleration

Figure 21 from Baker et al. (2019a) provides a snapshot of radiation belt variability for 1.8 MeV to 6.3 MeV electron energies at radial distances Earthward of $L \sim 6$. Time scales from hours to years are apparent, with the dynamic outer radiation belt MeV electron loss and recovery during storms being a striking and persistent feature. Despite drastic changes in the geomagnetic field configuration during solar storms that result in an almost total depletion of the MeV outer belt electrons, a rapid recovery of the outer zone can subsequently take place in a matter of a few hours (e.g., Baker et al. 2014a). Wave-particle interactions (e.g., Reeves et al. 2013), radial diffusion (e.g., Elkington et al. 1999, 2003; Hudson et al. 2000) and impulsive shock response (e.g., Foster et al. 2015; Kanekal et al. 2016) comprise the variety of physical processes that energize electrons.

REPT observations of all these varieties of energization processes (for reviews see, for example, Thorne 2010; Reeves et al. 2013) during a wide range of geophysical conditions have led to a significant increase in our understanding of the acceleration mechanisms that shape radiation belt dynamics.

6.4.1 Local Acceleration

Despite drastic changes in the geomagnetic field configuration during solar storms that result in an almost total depletion of the MeV outer belt electrons, a rapid recovery of the outer zone can subsequently take place in a matter of a few hours (e.g., Baker et al. 2014a). The month-long observations of the evolution of the outer radiation belt electron fluxes shown in Fig. 22 show the effect of two storm-associated acceleration events on 01 and 17

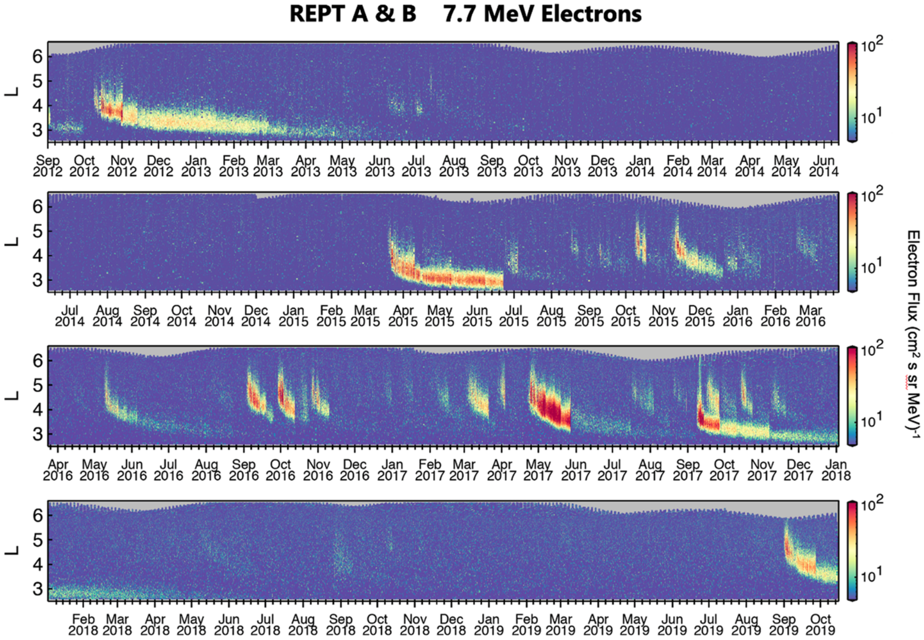

Fig. 17 7.7 MeV electron data from REPT-A and -B over the mission lifetime in L vs. time format (same color scale for each panel)

March 2013. Each event involves a rapid increase in MeV fluxes followed by periods of slow inward diffusion accompanied by adiabatic acceleration. This occurs as the electrons move into the region of higher magnetic field strength nearer the Earth. Of particular note is the sharp reduction (dropout) of electron fluxes at all energies during the 17 March event. This was followed by the rapid reappearance strong fluxes at energies up to $E > 5$ MeV in the innermost regions of the outer zone at $L < 4$.

Such rapid radiation belt recovery in the inner magnetosphere involves local acceleration of 100s of keV seed electrons to multi-MeV energies in the low-density region outside the plasmapause (Reeves et al. 2013) through interactions with whistler-mode very low frequency (VLF) chorus waves (Thorne et al. 2013b; Foster et al. 2014; Li et al. 2016c). Jaynes et al. (2015) have shown that magnetospheric substorm activity produces two distinct electron populations that are essential to the acceleration of highly relativistic electrons in the outer belt: a source population of 10s keV electrons that drive VLF wave growth, and a seed population at 100s keV that are then accelerated by the VLF waves to MeV energies.

Li et al. (2016c) simulated the evolution of storm time radiation belt recovery following a large storm and accentuated the critical role chorus plays in accelerating electrons up to several MeV. Their simulation underestimated the observed electron acceleration when only radial diffusion was included. Plasmaspheric hiss was found to provide efficient pitch angle scattering losses for hundreds of keV electrons, while scattering >1 MeV electrons at a slower rate. Their simulation found that the combined physical processes of radial diffusion and pitch angle and energy diffusion by chorus and hiss reproduced the observed electron dynamics quite well. They suggested that quasi-linear diffusion theory provided a reasonable means for evaluating radiation belt electron dynamics during such storms.

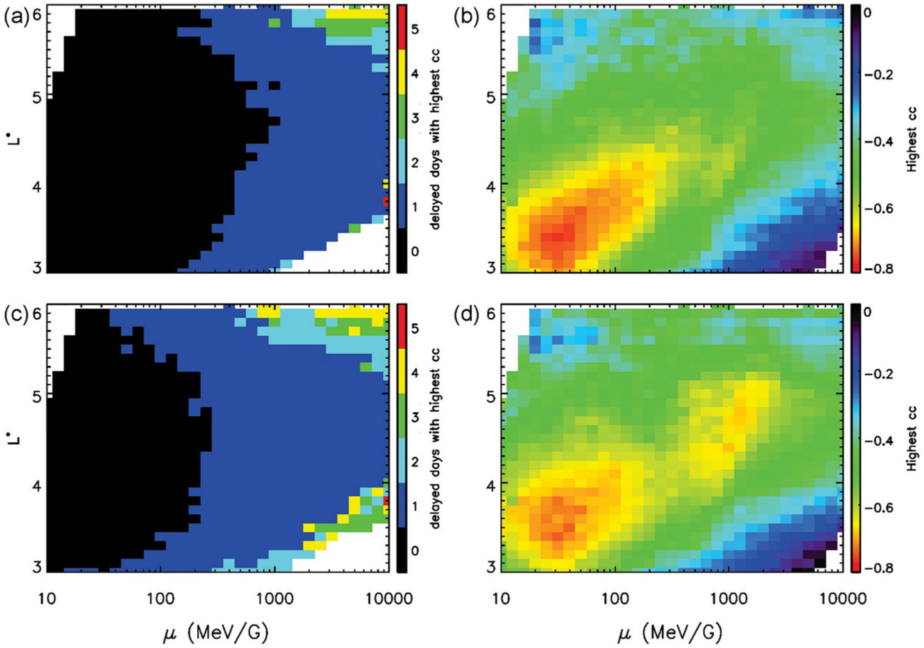

Fig. 18 Reprinted from Zhao et al. (2017). Figures 18a and 18b are for SYM-H index, and Figs. 18c and 18d are for AL index. Panels a and c depict the time lag of radiation belt electron PSD enhancements corresponding to the best correlation coefficient with geomagnetic indices, and panels b and d depict the corresponding highest correlation coefficients, as a function of μ and L^*

During events such as seen on 17 March 2013, the recovery of multi-MeV electrons at $L \sim 3$ - 5 can take place significantly more rapidly (30-60 min) than can be explained by diffusive processes, indicating the importance of nonlinear processes (Foster et al. 2014). Figure 23 shows the L-space evolution of outer zone 2.6 MeV electrons observed by the REPT. At $L \sim 4.2$, pre-storm fluxes fell by ~100x during the storm-induced flux dropout discussed in Fig. 22. Over the subsequent 12 hours 2.6 MeV fluxes increased by factors of 30x during each of two impulsive substorm events at 16 UT and 22 UT, as described by Foster et al. (2014, 2017). As shown in Fig. 24, consecutive observations by the dual Van Allen Probes in the region of flux dropout and local acceleration at $L \sim 4.2$ characterize the evolution of the event.

Highly relativistic (>~4-5 MeV) electrons are accelerated locally in rapid nonlinear interactions with very low frequency (VLF) chorus rising tone waves in the region of low cold plasma density outside the plasmapause. Electron injections and VLF chorus enhancement associated with the 1550 UT substorm are shown in Fig. 25. Chorus risers grow through interactions with the 10s of keV electrons injected Earthward from the outer magnetosphere during storm conditions. The 100s of keV electrons and intense VLF waves provide a seed population and energy source for the radiation belt enhancements. Electron interactions with the VLF rising tones are strongly nonlinear, such that a fraction of the near-relativistic seed electrons at resonant energies are trapped by waves, leading to significant nonadiabatic energy exchange. In effect, nonlinear interactions directly transfer energy from the injected electrons to the high-energy tail of the electron distribution through the intermediary of the VLF waves in a fraction of a second.

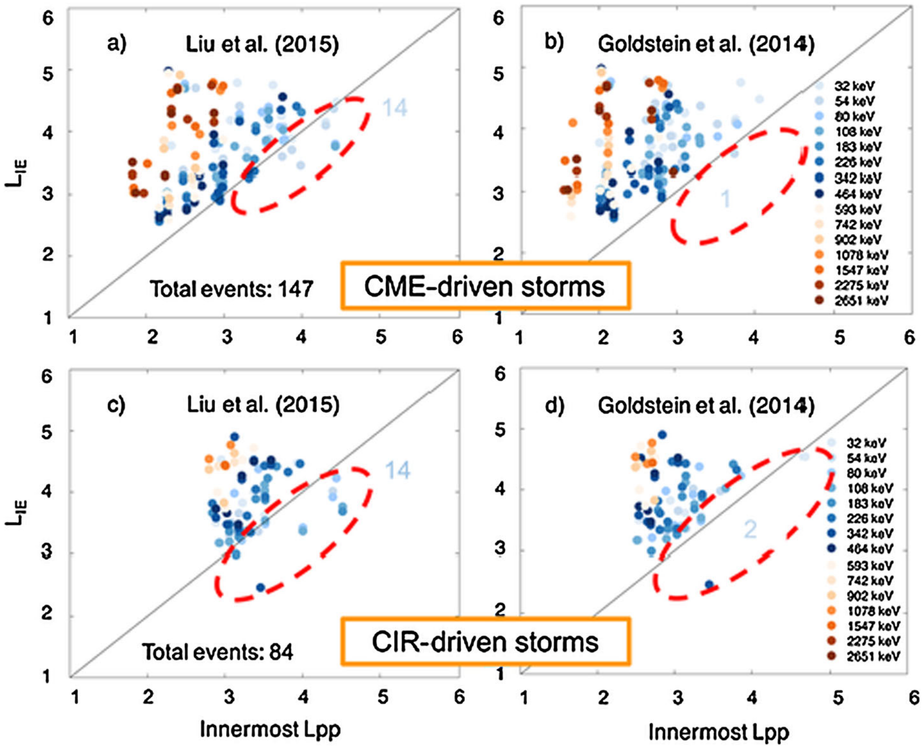

Fig. 19 Relationship between the innermost plasmapause location (as predicted by two distinct models) and the initial enhancement location of radiation belt electrons. The results show that nearly all enhancement events occurred outside the plasmapause in either plasmasphere model, and the enhancement location L_{IE} showed a distinct energy dependence. After Khoo et al. 2019

During this event Probe A followed Probe B by ∼60 min inbound along the same orbital path at ∼ 01 MLT. At the 1550 UT time of the substorm injection A was at $L \sim 4.5$ and B at $L \sim 4$. During the subsequent hour Probe A sampled the evolving MeV electron population across the $L = 4.5$–4.0 region where Probe B had observed the background fluxes one hour earlier. Figure 26 presents the REPT 2.6 MeV flux observations and the ratio of the post-injection (A) to pre-injection (B) for the complete range of energies sampled by the MagEIS and REPT instruments. The rapid onset of strong (>10x) enhancements of ∼1–3 MeV electron flux characterize the effects of local acceleration processes during the event.

Through detailed examination of VLF chorus and electron fluxes observed by the Van Allen Probes, Foster et al. (2017) and Omura et al. (2019) have investigated the efficiency of nonlinear processes for acceleration of electrons to MeV energies. Through subpacket analysis of observed chorus waveforms and the application of nonlinear theory (e.g. Hsieh and Omura 2018) those studies found that electrons with initial energy of hundreds of keV to 3 MeV can be accelerated by 50 keV–200 keV in resonant interactions with a single VLF rising tone on a time scale of 10–100 ms. The results of the calculations presented by Omura et al. (2019) are presented in Fig. 27. While cyclotron acceleration is significant, that study found that relativistic electrons can be accelerated more efficiently through Landau resonance with obliquely propagating chorus waves. Both the nonlinear Landau and cyclotron

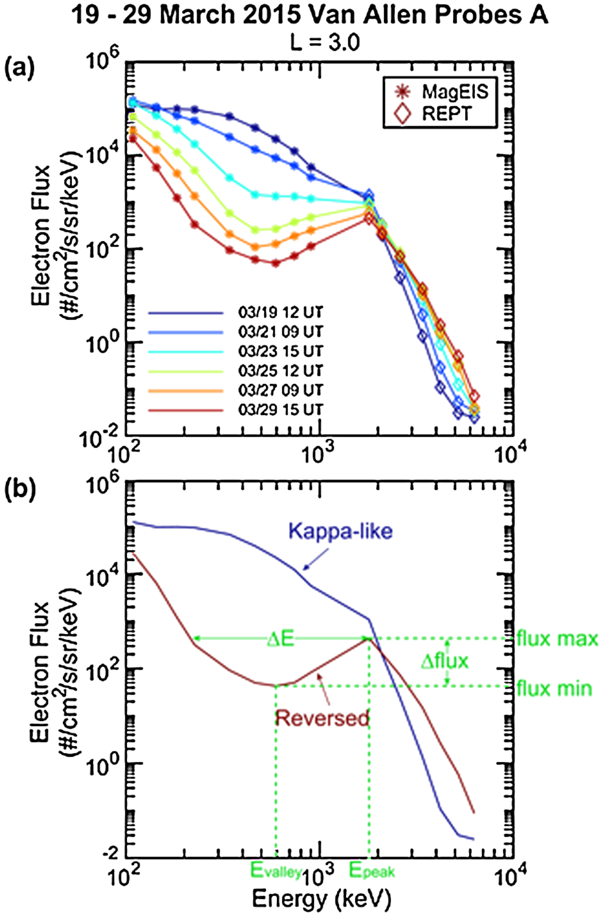

Fig. 20 Reversed energy spectrum evolving due to interaction with plasmaspheric hiss waves. After Ni et al. (2019)

interactions produce maximum energy gain for 1–3 MeV electrons, as was shown in the REPT and magEIS observations for that event as presented in Fig. 26.

6.4.2 Diffusion and Adiabatic Ultrarelativistic (> 5 MeV) Acceleration

Radial diffusion has long been recognized as a critical acceleration mechanism for radiation belt electrons. Since the launch of Van Allen Probes, the important role of radial diffusion in accelerating multi-MeV electrons has been further demonstrated. Using data from the REPT instrument on the Van Allen Probes, Baker et al. (2014a) showed classic signatures of inward radial diffusive acceleration of $\sim$2–6 MeV electrons in the outer radiation belt in March 2013. Su et al. (2015), focusing on a radiation belt event of 15 February 2014, showed that inward radial diffusion alone could enhance multi-MeV electron fluxes by up to one order of magnitude in the outer belt within 10 hours. Li et al. (2016), using a three-dimensional diffusion model and comparing simulation results to Van Allen Probes measurements, showed that radial diffusion plays an important role in accelerating electrons to multi-MeV energies during an intense storm of 17 March 2015. Focusing on the same event, Jaynes et al. (2018) showed that relatively fast radial diffusion could be mainly responsible for the multi-MeV electron flux enhancements during this storm in the core of the outer belt. Further studies

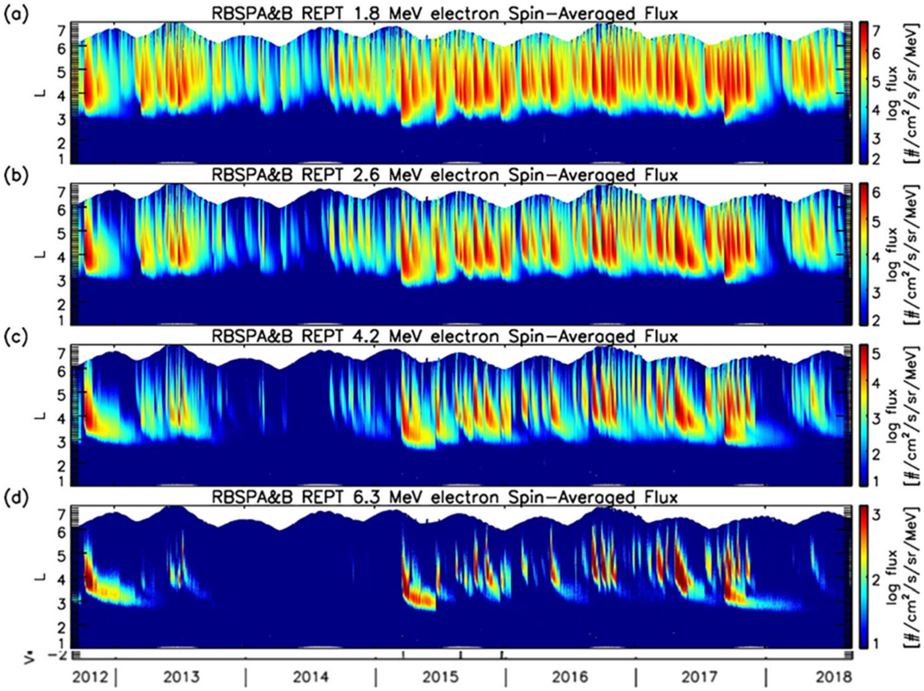

Fig. 21 Spin-averaged fluxes of electrons with energies of 1.8, 2.6, 4.2, and 6.3 MeV from 1 September 2012 to 1 September 2018, using data from both Van Allen Probes

on the radiation belt electron acceleration also suggest the role of radial diffusion on the multi-MeV electron acceleration in the center of the outer belt is energy-dependent. Zhao et al. (2018), using data from the REPT instruments on the Van Allen Probes, studied multi-MeV electron flux enhancements during one small-to-moderate geomagnetic storm of April 2017. Detailed analysis of the electron phase space density during this storm, as shown in Fig. 28, showed that for $\mu = \sim 4000$–1000 MeV/G, K=0.01 $G^{1/2}$Re electrons ($\sim$3–5 MeV in the center of the outer belt), clearly growing peaks in electron PSDs suggest local heating as the main acceleration mechanism. However, as the electron energy gets higher, inward radial diffusion becomes more dominant; for $\mu = 16000$ MeV/G, $K = 0.01$ $G^{1/2}$Re electrons ($\sim$7 MeV in the center of the outer belt), positive electron PSD radial gradients suggests that inward radial diffusion is the main acceleration mechanism during this storm. Combining this with radial diffusion modeling, they demonstrated that inward radial diffusion alone could well explain the acceleration of $\sim$7 MeV electrons in the core of the outer belt. A statistical analysis of electron phase space density evolution during 19 multi-MeV electron flux enhancement events in the Van Allen Probes era by Zhao et al. (2019) also suggested the existence of such an energy-dependent role of radial diffusion in accelerating electrons into multi-MeV energies.

6.4.3 ULF Acceleration

The interaction of energetic particles with waves satisfying a drift-resonant condition results in radial diffusion in which stochastic radial motion tends to move particles in the direction opposite the prevailing gradients of the local phase space density. Processes violating the

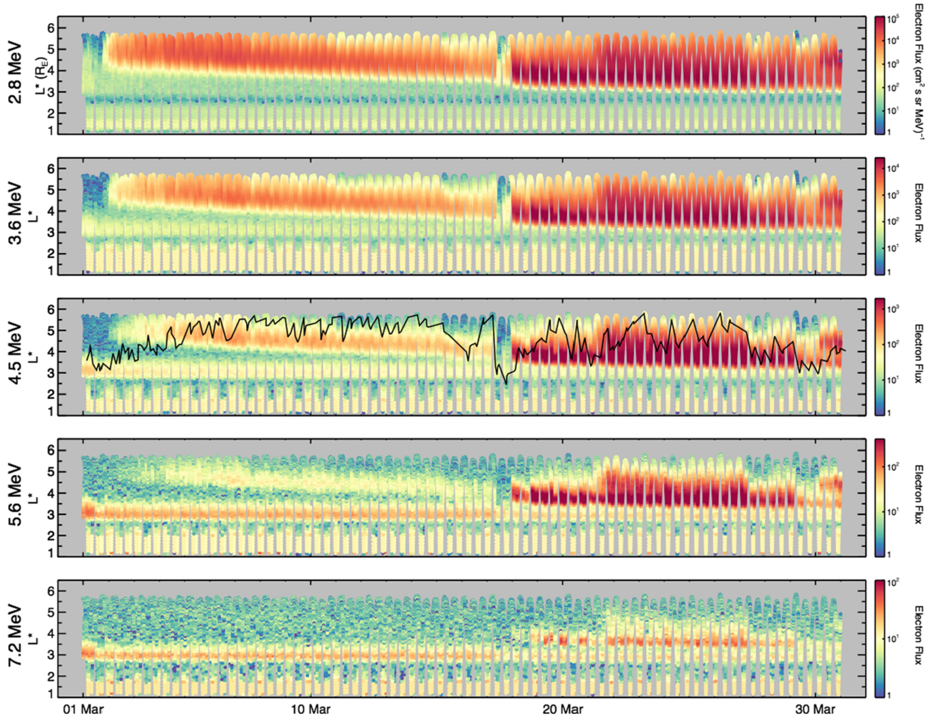

Fig. 22 Details of multi-MeV electron flux variations for the month of March 2013. The black trace (middle panel, 4.5 MeV) represents the plasmapause location derived from EFW spacecraft density measurements. Of note is the sharp MeV electron flux dropout and prompt recovery on 17 March 2013

drift invariant (i.e., occurring on a time scale short with respect to particles' drift periods) will transport electrons into regions of larger or smaller magnetic field strength. Inward transport of energetic particles will lead to an increase in energy of that population due to the conservation of their gyro- and bounce- invariants. Waves satisfying the drift resonance condition for MeV electrons in the inner magnetosphere are Pc-5 waves with frequencies in the mHz range. Ali et al. (2016) found that diffusion due to electric fields was statistically the dominant driver of stochastic radial transport in the radiation belts. Adiabatic acceleration associated with inward radial diffusion can produce significant energization as reported by Jaynes et al. (2018) who reported the acceleration of MeV electrons to ultra-relativistic energies in a matter of days driven by strong ULF waves. Section 7.3 of this report describes such diffusive acceleration in more detail.

6.4.4 Direct Injection of MeV Electrons into the Inner Magnetosphere

Substorm electron injections accompanied by the transient and intense substorm electric fields can directly lead to rapid enhancements of the seed populations in the heart of the outer radiation belt (Tang et al. 2018). In addition to such 10s–100s keV sub-relativistic seed electron populations, substorms can inject relativistic 'killer' electrons (≥ 1 MeV) directly into the outer radiation belt (e.g. Dai et al. 2014). Enhancements of hundreds of keV electrons during dipolarizations in the magnetotail can account for such injected MeV electrons through Earthward transport. Injected particles are trapped on closed orbits as the

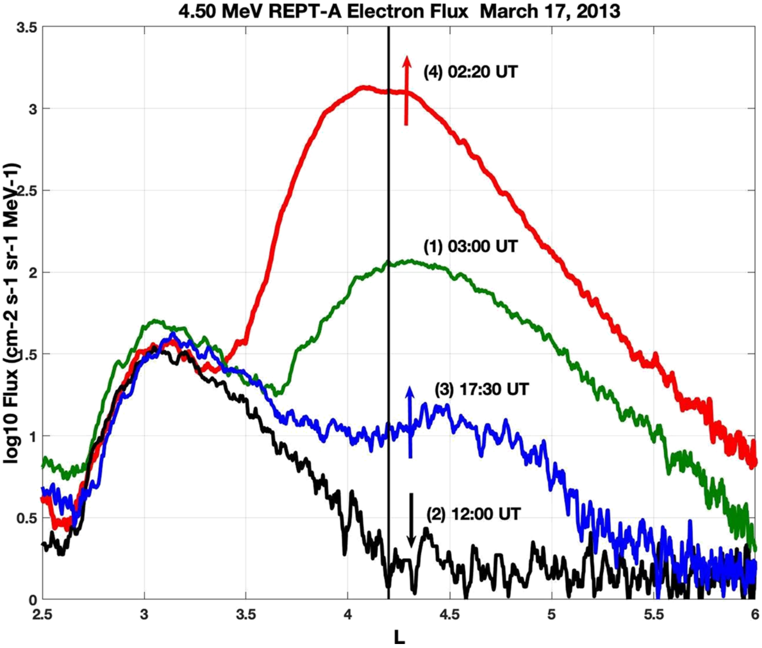

Fig. 23 The L^* variation of REPT A 2.6 MeV electron fluxes during the 17–18 March 2013 storm are shown for passes across the outer radiation belt by Van Allen Probe A. Passes are labeled with the time of crossing $L^* = 4.2$ (vertical black line). Arrows denote whether the 2.6 MeV fluxes were increasing or decreasing in the inner magnetosphere at that time. The prestorm L^* profile is shown in green (#1 at 2:55 UT). Storm time depletion of the outer belt is shown in black (#2 at 12:05 UT) when 2.6 MeV flux was decreased by a factor of $\sim$100. The blue curve (#3 at 16:55 UT) reflects the effects of the substorm injection at 15:50 UT that resulted in a partial recovery ($>$10X) of the outer belt relativistic electron flux. A second substorm onset at 22:15 UT was followed by a further $\sim$30X increase in the 2.6 MeV flux (#4 red curve; 02:15 UT on 18 March)

dipolarization electric field is diminished. As a result, deep injections can directly supply energetic particles to the center of the outer radiation belt. In a survey of the first nightside season of NASA's Van Allen Probes mission (December 2012 to September 2013), Turner et al. (2015) found 47 energetic (tens to hundreds of keV) electron injection events at L-shells $\leq$4. For these injections of seed electrons to $L \leq 4$, electron energies were limited to $\leq$250 keV. Tang et al. (2016) pointed out that the higher-energy seed electrons injected more deeply into the outer radiation belt can reach relativistic energy much faster, e.g., in interactions with chorus waves.

Dai et al. (2015a) reported observations of a substorm injection in the premidnight sector at $L \sim 5.5$ during which RBSP-A observed a large dipolarization electric field (50 mV/m) over $\sim$40 s and a dispersionless injection of electrons up to $\sim$3 MeV. Pitch angle observations indicated betatron acceleration of the MeV electrons at the dipolarization front. Similarly, Tang et al. (2016) have shown that substorm electron injections can be a direct external source of MeV electrons at the outer edge of the outer radiation belt ($L^* \sim 5.4$) in addition to providing intense seed populations of sub-relativistic electrons in the outer radiation belt. For the event on 16 August 2013, RBSP-A located in the outer radiation belt observed enhancements of MeV electrons accompanying substorm dipolarizations. The phase space density of MeV electrons at $L^* \sim 5.4$ increased by 1 order of magnitude in 1 h resulting in a local peak in MeV electron PSD.

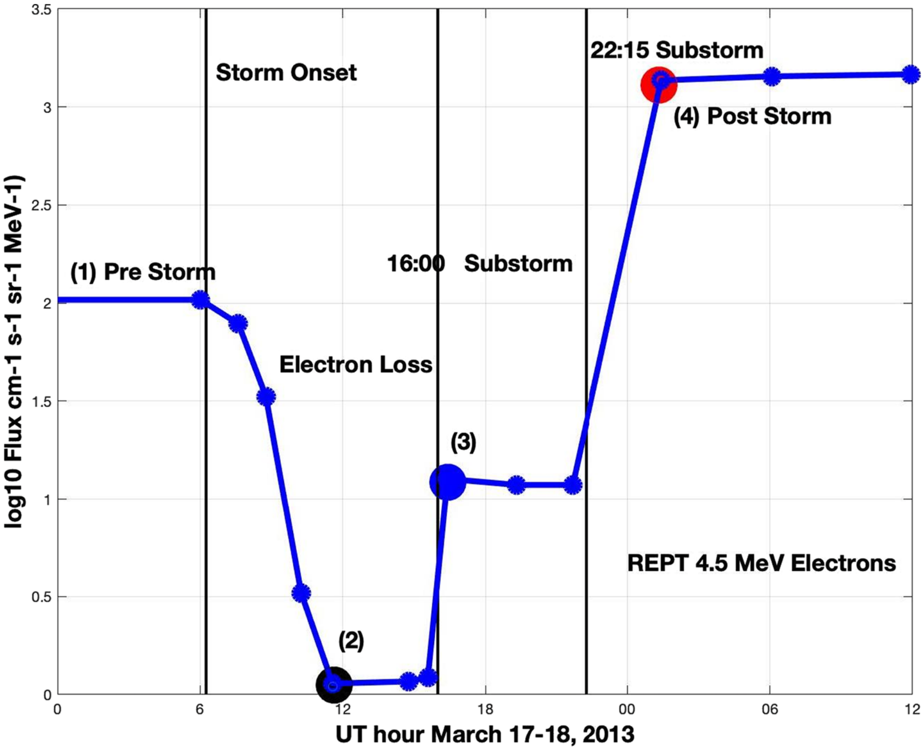

Fig. 24 Storm time changes in the 2.6 MeV electron fluxes observed at $L^* = 4.2$ with the REPT instruments on both Van Allen Probes A and B delineate the event time history of relativistic electron loss and recovery. Storm onset was at ∼06:15 UT on 17 March 2013 and prompt stepwise radiation belt energization accompanied substorm injections at 1550 UT and 2215 UT. Data points indicate the sequential observations by Probes A and B at $L^* = 4.2$. Larger colored data points indicate measurements taken during passes (2), (3), and (4) shown in Fig. 23

Just as the Van Allen Probes mission revealed in exquisite detail the mechanism and time scales of electron acceleration, so has the mission revealed details of the MeV electron loss. As is evident from many prior figures shown in this review (e.g., Fig. 8 and Fig. 10), the entire outer zone electron population ($E \gtrsim 1$ MeV) can be lost on timescales of a few hours (or less). Having the dual RBSP spacecraft has allowed observation of multi-MeV electron loss down to times of tens of minutes (Foster et al. 2014; Baker et al. 2016a, 2019a). Moreover, since the RBSP spacecraft operated very near the magnetic equator (and they covered all relevant energy ranges), it is clear that the disappearance of electrons across essentially all L-values is absolute and genuine. There is no recourse claiming apparent loss as might be attributed to adiabatic spectral changes or energetic electrons remaining in some narrow pitch angle band, trapped near the magnetic equator.

Much work – to be reviewed briefly here – with the RBSP sensor suite has shown two distinctive mechanisms for electron loss. The first is associated with magnetospheric compression and subsequent electron drift path distortions and outward radial diffusion, often related to CME impacts on the magnetosphere. Powerful interplanetary shock waves incident on the magnetosphere can cause the magnetopause to move inward by several Earth radii in just a matter of minutes (e.g., Dmitriev et al. (2014)). This in turn can allow multi-MeV electrons throughout much of the outer radiation belt to drift azimuthally into the

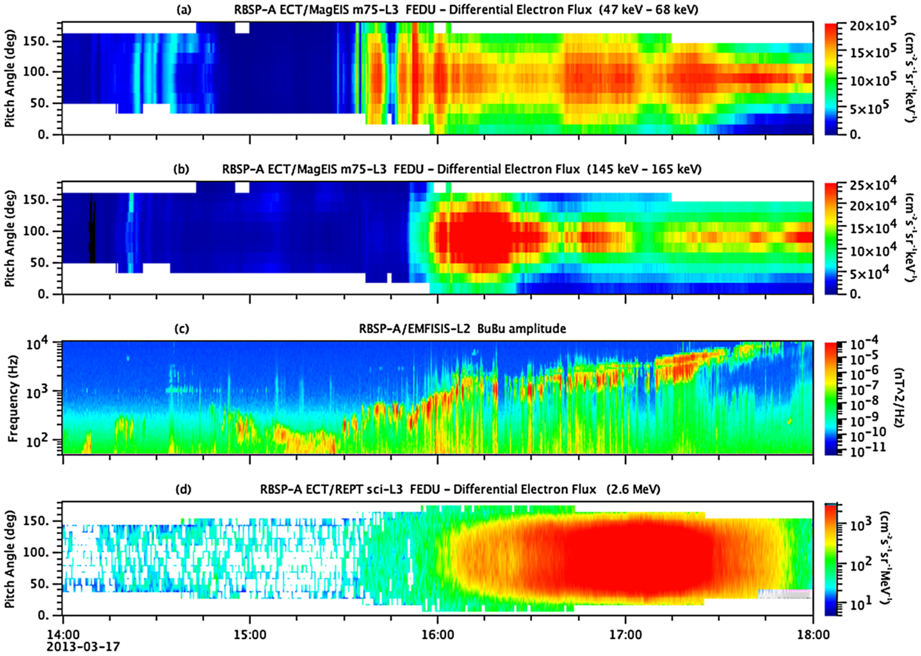

Fig. 25 Local acceleration involves the enhancement of VLF chorus by lower energy injected electrons and the subsequent energization of a seed population of higher-energy electrons by the amplified waves. (**a**) RBSP A MagEIS observations of injected ∼50 keV and (**b**) ∼150 keV electrons and (**c**) associated chorus emissions observed by EMFISIS A are shown for the 15:50 UT substorm interval. (**d**) The growing enhancement of 2.6 MeV electrons resulting from the local acceleration of the near-relativistic seed population

repositioned magnetosphere boundary. Losses of electrons that had previously been trapped on dipole L-shells $\gtrsim$4.0 have been observed to be lost on timescales of just a few minutes.

The second principal loss process for MeV electrons is due to scattering of previously trapped electrons either into the atmospheric bounce loss cone (e.g., Tu et al. 2010) or onto paths in the drift loss cone (e.g. Kim et al. 2008). As will be shown in this review, many wave modes such as magnetospheric chorus, hiss radiation, and EMIC waves all can cause significant scattering and loss of electrons $E \gtrsim 1$ MeV. Such losses can be somewhat gradual at times, or the wave-induced scattering can be abrupt. In either case, losses into the atmosphere by electron precipitation can represent an important coupling mechanism with the Earth's neutral atmosphere that can have crucial chemistry effects (see Sect. 6.8).

6.4.5 Landau Parallel Acceleration and Butterfly PA Distributions Due to Magnetosonic Waves

In addition to whistler-mode chorus, magnetosonic waves have been regarded as another viable candidate to accelerate radiation belt electrons (Horne et al. 2007). A detailed study of Xiao et al. (2015) demonstrated that the combined acceleration by chorus and magnetosonic waves can reasonably account for the relativistic electron flux evolution and the occurrence of electron butterfly pitch angle distribution measured by REPT during the 28 June 2013 geomagnetic storm, thereby providing a great support for the mechanism of wave-driven butterfly distribution of relativistic electrons (Zhao et al. 2014; Ni et al. 2020). A subsequent

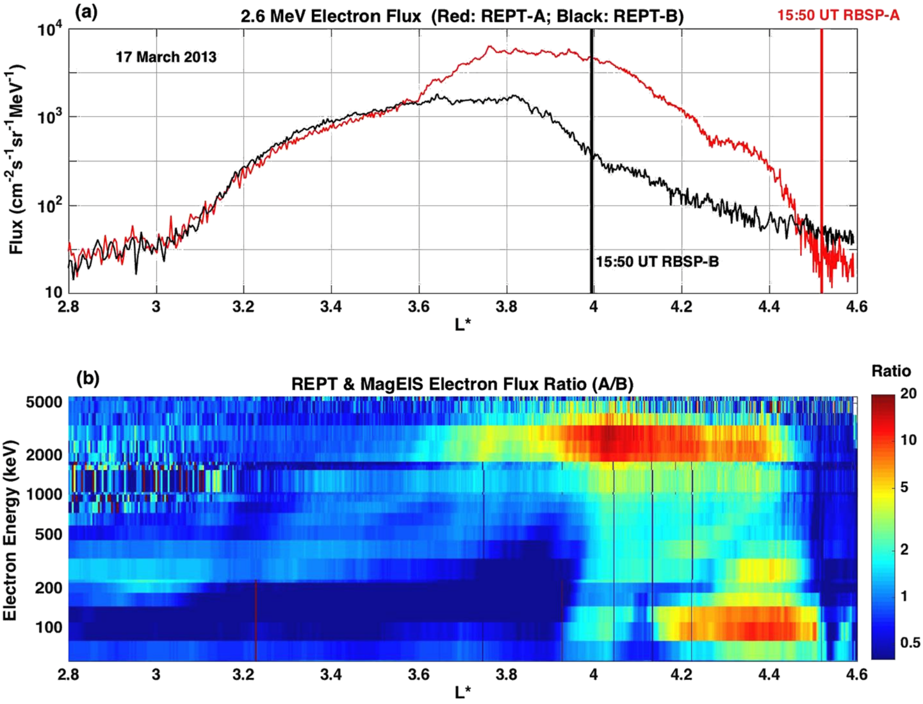

Fig. 26 (**a**) Sequential profiles of 2.6 MeV electron flux measured by the dual Van Allen Probes are shown. During the event, RBSP A followed RBSP B by ~1 h along the same orbital trajectory. RBSP B was at $L^* \sim 4.0$ at the 1550 UT substorm onset, while RBSP A was at $L^* \sim 4.5$. On its inbound orbit RBSP B observed presubstorm background fluxes over $L^* \sim 4.5$–4.0, while RBSP A observed postsubstorm enhancements. The plasmapause was observed at $L^* \sim 2.5$ at 1710 UT. (**b**) Ratios of electron flux (RBSP A (post substorm)/RBSP B (presubstorm)) are shown up to ultrarelativistic energies using MagEIS and REPT combined data (REPT data $\geq$1.8 MeV). Injected ~50–150 keV electrons were seen at 31 RBSP A between $L^* \sim 4.5$ and 4.1. The prompt onset of strong (>10x) enhancements of ~1–3 MeV electron flux characterize the effects of local acceleration processes during the event

study of Li et al. (2016b) reported Van Allen Probes observed close association between relativistic electron butterfly distributions and strong magnetosonic waves that occurred in the same regions and at the same time periods during the 17 March 2015 storm. By combining test particle calculations and Fokker-Planck diffusion simulations, they further reproduced the formation of ultrarelativistic electron butterfly distributions mainly attributed to the parallel acceleration caused by Landau resonance with magnetosonic waves as schematically illustrated in Fig. 29 (Li et al. 2016a).

6.5 Electron Loss

6.5.1 Magnetopause Shadowing: Storm-Time Geomagnetic Reconfiguration

As an extreme phenomenon of radiation belt electron losses, in particular during periods of strong geomagnetic disturbances, relativistic electron flux dropouts are generally thought to be attributed to non-adiabatic, irreversible processes including magnetopause shadowing and associated outer radial diffusion, and wave-particle interactions (e.g., Baker et al. 2019a;

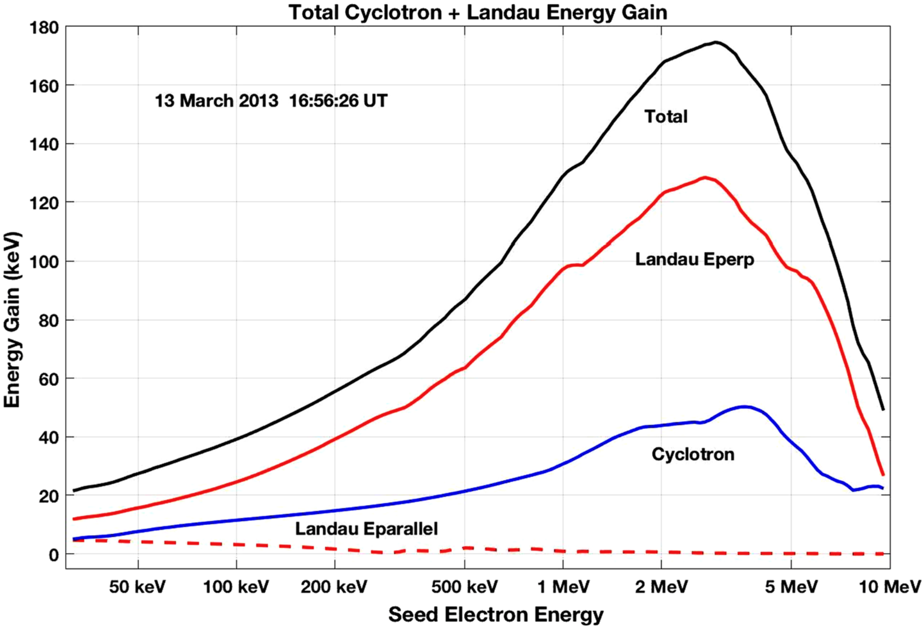

Fig. 27 Electron energy gain through nonlinear trapping in a single 60 ms interaction with a rising tone chorus element. Contributions by the parallel and perpendicular electric fields at Landau (n=0) and cyclotron ($n = 1$) resonances, and the total gain are plotted in different colors (after Omura et al. (2019)). Both the Landau and cyclotron interactions produce maximum energy gain for 1–3 MeV electrons, as was shown in the REPT and magEIS observations presented in Fig. 26

Millan and Thorne 2007; Gu et al. 2020). In terms of detailed analyses of a number of radiation belt flux dropout events seen by REPT, Hudson et al. (2014, 2015) performed MHD simulations to indicate that inward motion of the magnetopause and subsequent magnetopause shadowing effect, along with enhanced ULF wave power affecting radial transport, can explain the losses of relativistic electrons both in energy and pitch angle dependence. On basis of the Van Allen Probes observations, Zhang et al. (2016) performed a detailed analysis regarding the physical mechanism responsible for the pronounced depletion of ultra-relativistic electron fluxes by over 1 order of magnitude within 6 hours and the rapid changes in their electron pitch angle distributions right after a shock arrival on 27 February 2014. By modeling the electron pitch angle distribution under a compressed magnetic field topology based on actual solar wind conditions, they found that it is not the EMIC wave scattering but the drift-shell splitting closely related to the distorted, asymmetric geomagnetic field configuration that is more likely to account for the rapid changes in ultra-relativistic electron pitch angle distributions. Implementing a careful combination of identification of EMIC wave activity, computation of last closed drift shell and magnetopause standoff location, and construction of electron phase space density versus L* profiles and their dependence on the first two adiabatic invariants, a more comprehensive investigation was conducted by Xiang et al. (2017) to understand the underlying mechanisms of distinct radiation belt dropout events observed by Van Allen Probes. Their findings suggested that the radiation belt electron dropouts can be classified into three classes in terms of dominant loss mechanisms: magnetopause shadowing dominant, EMIC wave scattering dominant, and combination of both mechanisms. This therefore shed important light on the complex nature of radiation

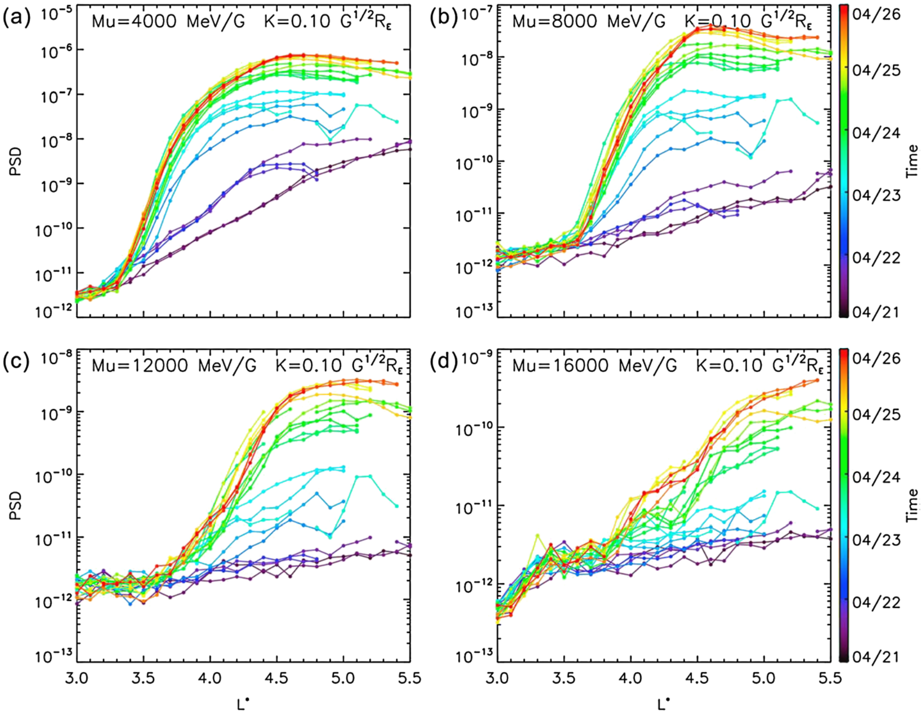

Fig. 28 (Fig. 3 of Zhao et al. 2018) The evolution of phase space density radial profile of electrons with different energies, during a small to moderate storm of April 2017

belt electron dropouts. A recent study of Tu et al. (2019) selected the 22-23 June 2015 relativistic and ultra-relativistic electron fast dropout event observed during an intense CME driven geomagnetic storm, and implemented the event-specific last closed drift shell (LCDS) model and the input of improved radial diffusion coefficients to simulate the consequence of magnetopause shadowing (Fig. 30). They found that accurate evaluation of LCDS along with the well evolving storm-time reconfiguration of the geomagnetic field is critical to reproduce the detailed dropout features observed by REPT, while the effect of EMIC wave scattering cannot be ruled out.

6.5.2 Fast Losses by EMIC Waves

It has been well recognized that EMIC waves act as an important mechanism for rapid losses of radiation belt relativistic electrons on timescales of hours or less (e.g., Summers and Thorne 2003; Ni et al. 2015). Based on Van Allen Probes EMFISIS and REPT data, Su et al. (2017) reported from both observational and numerical perspectives on EMIC wave-driven local precipitation loss of relativistic electrons in the heart of the outer radiation belt, showing that the spatially limited EMIC waves could cause the decrease of off-equatorially mirroring relativistic electron fluxes by up to 2 orders of magnitude within ∼1.5 h on 27 February 2014. Using >3 years of simultaneous Van Allen Probes and THEMIS (Time History of Events and Macroscale Interactions during Substorms) measurements, Zhang et al. (2017) found that MeV electron lifetimes are frequently strongly reduced by the combined

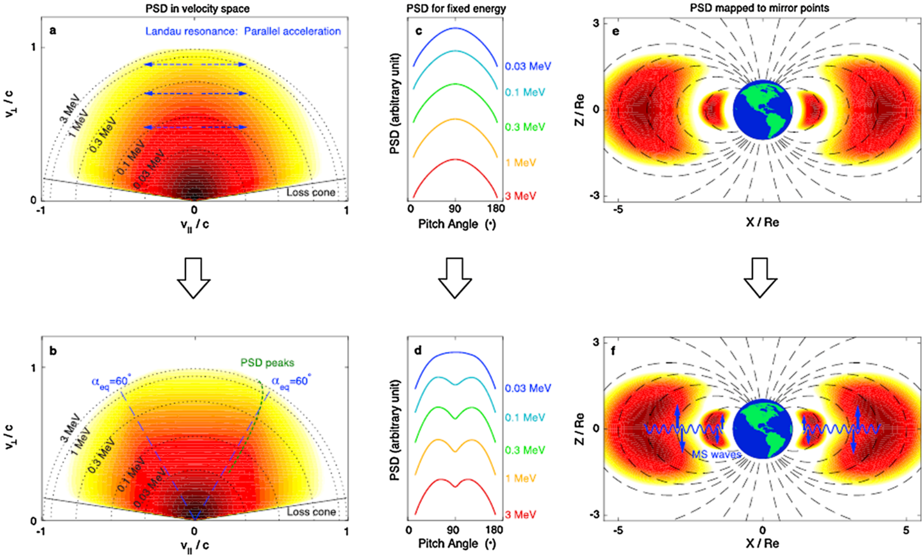

Fig. 29 Schematic illustrations of butterfly distribution formation caused by magnetosonic waves (after Fig. 6 of Li et al. 2016a)

scattering of the contemporaneous presence of EMIC and whistler mode waves and suggested that H^+-band EMIC waves may be more important to impact globally on multi-MeV electron lifetimes than previously assumed. Through a case study of the close conjunction between Van Allen Probes and THEMIS, Bingley et al. (2019) provided further observational evidence to support the hypothesis that EMIC waves are an important mechanism to drive the distinct energy-dependent "bite-out" scattering signature in the relativistic electron pitch angle distribution captured by REPT measurements (see Fig. 31), while no effort was performed to numerically quantify the relationship between the EMIC wave activity and the evolution of the pitch angle bite-out feature.

6.5.3 Losses Caused by Plasmaspheric Hiss

Plasmaspheric hiss waves, generally existing inside the cold, dense plasmasphere, play a critical role in radiation belt electron losses. The wave-particle interaction between plasmaspheric hiss waves and relativistic electrons can scatter electrons to the loss cone and precipitate them into the atmosphere in hours to days. Thorne et al. (2013a) performed quantitative analysis on the decay of a radiation belt electron remnant belt at energies above 2 MeV, following the September 2012 storm. They showed that these multi-MeV electrons were subject to slow decay due to pitch angle scattering by plasmaspheric hiss on timescales of $\sim$10–20 days. The L- and energy-dependent features of hiss wave scattering have also been well recognized (e.g., Reeves et al. 2016; Ripoll et al. 2016), which lead to the formation of a reversed energy spectrum inside the plasmasphere. Zhao et al. (2019), using data from REPT and MagEIS instruments on the Van Allen Probes, reported this reversed energy spectrum of radiation belt electrons generated by the wave-particle interaction between electrons and plasmaspheric hiss waves. As Fig. 32 shows, after an intense geomagnetic storm of March 2015, the energy-dependent loss of radiation belt electrons carved a local minimum at an energy of around a few hundreds of keV in the traditional steep-falling energy spectrum in a

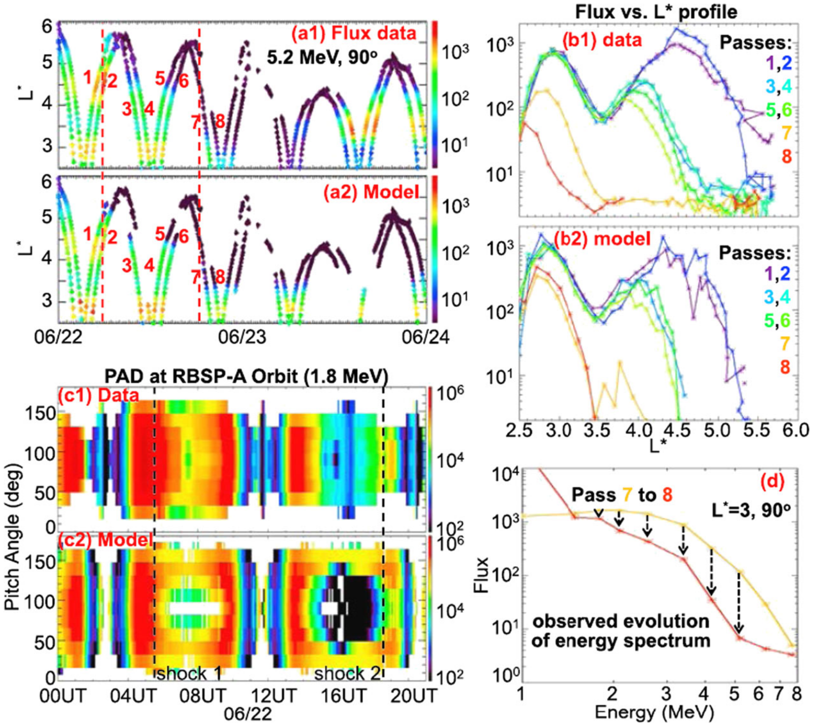

Fig. 30 Observations and simulations of relativistic and ultrarelativistic electron flux distributions during the period of 22-23 June 2015 that covered two shock intervals. The event-specific last closed drift shell (LCDS) model and the input of improved radial diffusion coefficients are implemented to simulate the consequence of magnetopause shadowing (After Fig. 3 of Tu et al. (2019))

few days. Through the statistical analysis, Zhao et al. (2019) reported that this reversed energy spectrum, or so-called "bump-on-tail" energy spectrum, is actually the most prevalent energy spectrum inside the plasmasphere at $L >\sim 2.6$. Moreover, using a two-dimensional Fokker-Planck simulation with a data-driven, time-varying plasmaspheric hiss wave model, they well reproduced the formation and main signatures of the bump-on-tail energy spectrum, as shown in the bottom panels of the Fig. 32. The correspondence between observations and simulations demonstrated that the plasmaspheric hiss waves are responsible for the generation of this reversed energy spectrum, which also has important implications at magnetized planets in the heliosphere and beyond. In the follow-up studies, through a detailed parametric study and a more thorough statistical study, Ni et al. (2019) and Zhao et al. (2019) further highlighted the critical role of hiss waves in causing the energy-dependent loss of radiation belt electrons inside the plasmasphere and shaping the energy spectrum under various conditions.

6.5.4 ULF Driven Loss

Another important loss process of radiation belt electrons is the outward radial diffusion driven by ULF waves. With negative radial gradients in electron phase space density, the radial diffusion process, commonly driven by ULF pc4-5 waves in Earth's inner magnetosphere, moves radiation belt electrons outward to the regions with lower magnetic field

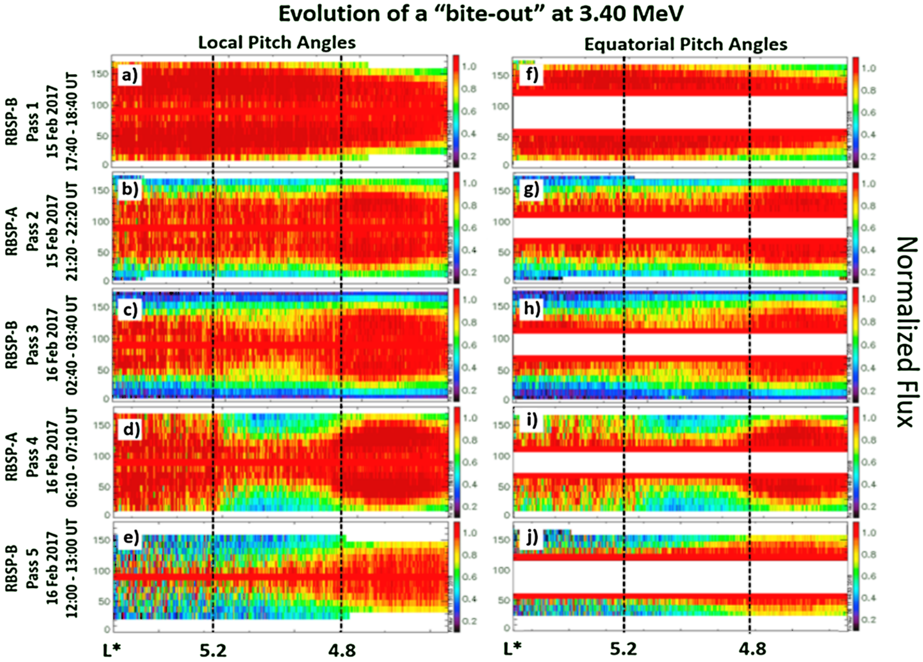

Fig. 31 Comparison of the development of the local (left) pitch-angle distribution through five consecutive passes through the region of $L^* = 4.8$–5.2 and the equatorial (right) pitch angle distribution captured in situ by the Van Allen Probes on 15–16 February 2017 as the signature of EMIC wave driven scattering of ultrarelativstic electrons (after Fig. 4 of Bingley et al. (2019))

strength and decreases their energies. The magnetopause shadowing effect can also accelerate this loss process. More detailed reviews on the ULF wave driven losses of radiation belt electrons can be found at Sect. 6.7.

6.5.5 Combined Scattering Effect of Chorus, MS Waves and Exo-Hiss

Different types of magnetospheric waves can occur simultaneously in space. In contrast to the concurrent occurrence of two wave modes, e.g., chorus and MS waves (Xiao et al. 2015) and EMIC and whistler waves (Zhang et al. 2017), Hua et al. (2018) reported a representative event of simultaneous magnetosonic waves, exohiss and two-band chorus emissions observed by EMFISIS on the dayside (Fig. 33). They further performed a detailed analysis to demonstrate that resonant interactions with simultaneous magnetospheric waves need careful treatment to interpret MagEIS and REPT measurements of dynamic variations of both energy spectrum and pitch angle distribution of radiation belt electrons, in which the competition and cooperation between various waves with different wave amplitudes can play an essential role (e.g., Ni et al. 2017; Hua et al. 2019).

A full picture of interacting wave modes and their effects on the relativistic and ultrarelativistic electron populations is not yet complete, although the Van Allen Probes mission has made considerable progress in our understanding of the complex wave-particle interactions that combine to create the observed particle dynamics.

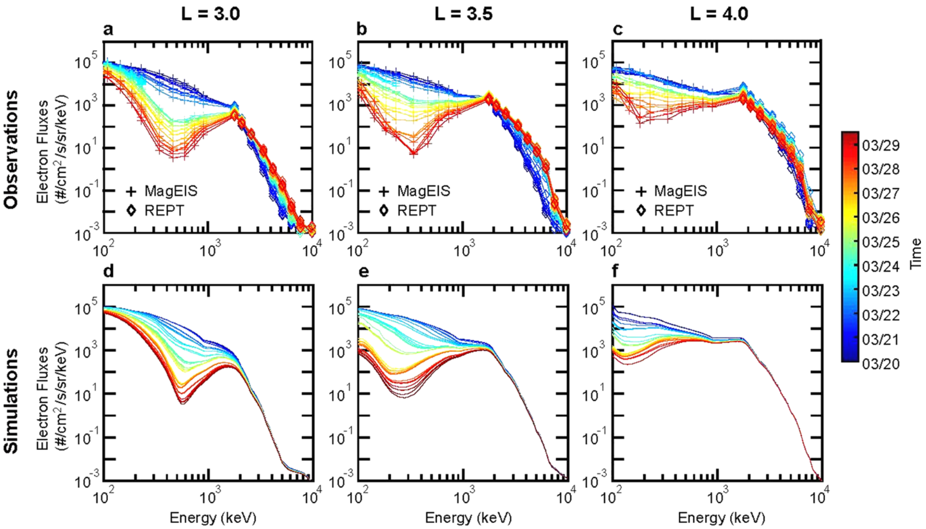

Fig. 32 (Fig. 4 of Zhao, Ni et al. 2019 Nature Physics paper). (Top panels) Observations and (bottom panels) simulation results of the evolution of radiation belt electron energy spectrum at three different L-shell, after an intense storm of March 2015

6.6 IP Shock Effects

Electron energization in the magnetosphere can be driven by sporadic and abrupt solar phenomena such as coronal mass ejections (CME), high-speed streams (HSS), and interplanetary (IP) shocks (Baker et al. 2019a). The characteristic time scales of these dynamical processes are however very different, with the most rapid energization being that due to IP shocks that can inject electrons deep into the magnetosphere within a few minutes (e.g. Blake et al. 1992; Kanekal et al. 2016; Foster et al. 2015). The most dramatic example of such an event was observed by the CRREs spacecraft during March 1991 (Blake et al. 1992) and resulted in the injection of >13 MeV electrons into the inner belt ($L \sim< 2$).

Recent observations from Van Allen probes have confirmed that prompt acceleration by impulsive shock-induced electric fields and subsequent ULF wave processes comprise a significant mechanism for the acceleration of highly relativistic electrons deep inside the outer radiation belt. There were numerous examples of Coronal Mass Ejections/Interplanetary Shocks leading to the prompt injection and energization of radiation belt particles during the lifetime of the Van Allen Probes mission. These events occur when coronal material ejected from the sun propagates super-Alfvenically through the heliosphere and impacts the Earth's magnetosphere, sending a fast-mode wave tailward from the magnetopause. This propagating wave will preferentially transport and accelerate particles with drift velocities that allow them to stay in phase with the wave as it moves through the inner magnetosphere (e.g. Li et al. 1993; Wygant et al. 1994; Elkington et al. 2003). Some examples of CME/IPS injections observed by the Van Allen Probes include (but are not limited to) events occurring in March 2013 (e.g. Li et al. 2015a; Hudson et al. 2015); October 2013 (e.g. Foster et al. 2015); March 2015 (e.g. Kanekal et al. 2016; Hudson et al. 2017); and July 2017 (e.g. Hao et al. 2019; Patel et al. 2019).

The REPT instrument is very well suited to measure high energy electrons (see Sect. 2) and the Van Allen Probes carry a full suite of fields and waves instrumentation (Breneman

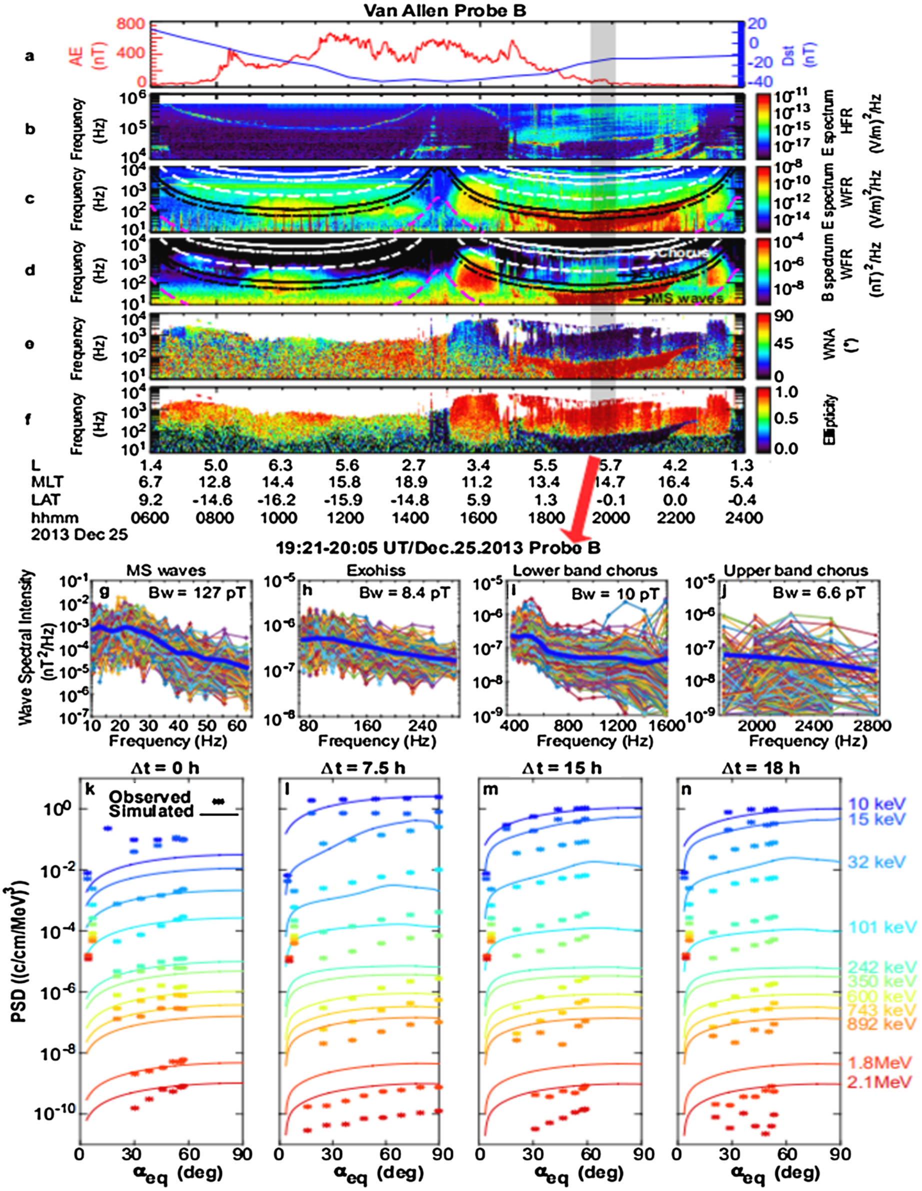

Fig. 33 (Top) Simultaneous occurrence of magnetosonic waves, exohiss and (lower- and upper-band) chorus waves observed by Van Allen Probe B on 25 December 2013, and (bottom) comparison between the temporal evolution of simulated electron PSDs (solid curves) and electron PSDs observed by MagEIS and REPT (star sign data points) under the impact of combined scattering of the three wave modes (modified version of Figs. 1 and 4 from Hua et al. (2018))

et al. 2020; Kletzing et al. 2020) to support investigations of electron acceleration processes. Although solar cycle 25 has been relatively less active than its predecessor, multiple IP shock events have been observed by Van Allen Probes during its lifetime. Some examples of CME/IPS injections observed by the Van Allen Probes include (but are not limited to) events occurring in March 2013 (e.g. Li et al. 2015a; Hudson et al. 2015); October 2013 (e.g. Foster et al. 2015); March 2015 (e.g. Kanekal et al. 2016; Hudson et al. 2017); and July 2017 (e.g. Hao et al. 2019; Patel et al. 2019).

6.6.1 IP Shock Driven Rapid Energization

The twin Van Allen Probes (A and B) provided in situ observations of shock effects in the dayside magnetosphere at the location where shock-induced acceleration of relativistic electrons occurs during the 8 October 2013 event reported by Foster et al. (2015). Simultaneous dayside observation at $L \sim 3$ and $L \sim 5$ quantified the spatial extent and duration of the shock-induced electric field and the spatial region over which acceleration took place.

EFW measurements provided evidence that a substantial portion of the dayside equatorial magnetosphere was occupied for periods of 1-2 minutes with a strong dusk-dawn/azimuthal component of the electric field. Those measurements determined a 850 km/s azimuthal propagation velocity for the shock-induced magnetosonic pulse and a $\sim$60 s duration for maximum acceleration of the electrons in drift resonance with the shock-induced wave. The 60 s resonance time is short with respect to the $\sim$350 s resonant electron drift period indicating that the 3rd (drift) invariant would be broken. Electron energization follows from first invariant conservation and inward transport of the electron source population in L space over a fraction of an electron drift period. Following this scenario, a preferred range of energies for the initial shock enhancement can be predicted. The analyses of the magnetosonic pulse for this event indicated that the resonant electrons should be centered in the REPT 3.4 MeV energy channel.

As resonant electrons are accelerated, they are adiabatically displaced to lower L where they continued to circle the earth forming discrete energy dependent drift echoes. REPT observations of the energy and temporal extent of the relativistic electron drift echoes observed by Van Allen Probes A are shown in Fig. 34. Significant shock response was observed across a two-decade electron energy range interval 50 keV to $>$5 MeV, as determined by combined MagEIS and REPT observations. Drift echoes with energy and L-dependent drift periods are characteristic features of the impulsive electron acceleration associated with IP shock events (e.g. Blake et al. (1992)).

Dual spacecraft observations afforded by the Van Allen Probes provided a unique viewpoint of the shock effects as functions of time, L, and energy. During the 8 October event, Probe A followed Probe B across L space by $\sim$1 hour with both spacecraft traversing essentially the same orbital path. Figure 35 presents an overlay of the Probe A and Probe B L^* profiles of 3.6 MeV REPT electron energy flux along the outbound orbits during which the shock effects were observed. Arrows indicate the $\sim$2022 UT time of shock observation at each spacecraft. With this orbital configuration, Probe B observed the pre-shock background for electron flux and phase space density (PSD) out to $L^* \sim 5$ (i.e. prior to its position at 2022 UT) $\sim$1 hour before Probe A observed the post-shock conditions across that range of L^*. In good agreement with calculations based on the shock electric field analyses, comparison of the Probe A and Probe B REPT phase space density measurements indicated that the source population lay about $\sim$0.3 R_E tailward of the accelerated population.

Figure 36 presents the change in the electron PSD at each observation point determined as the ratio of the post-shock observations by Probe A to the pre-shock (background) observations by Probe B. The accelerated population at 1000-5000 MeV/G centered at $L^* \sim 3.8$ was observed within 20 min of the shock arrival as Probe A traveled outward across that range of L^*. Figure 36 illustrates the promptness ($<$20 min) and both the spatial extent

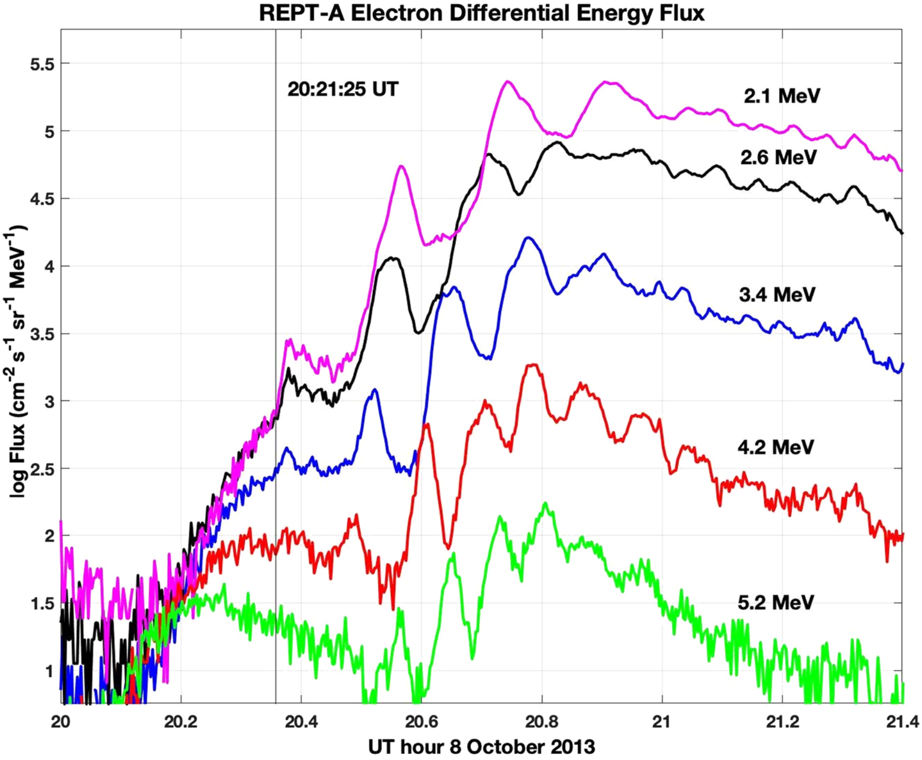

Fig. 34 The REPT instrument on Probe A observed the energy and temporal extent of relativistic electron drift echoes across several discrete detector channels. The variations in drift period apparent in the figure depend both on electron energy and the spatial variation of $|\mathbf{B}|$ as Probe A moves outward to a greater radial distance. Shock arrival at Probe A at 20:21:25 UT is indicated

($L^* \sim 3.5$ to 4.0) and energy range (2.0 to 5.0 MeV) of the inner region enhancement. This enhanced region remained essentially unchanged in that location for many hours following the shock impact. At higher L^* (≥ 4.5) significant (>10x) loss of the relativistic electron population in the outer regions was observed within ~1 hour of the time of shock onset.

For this event, REPT observations indicate that the shock effects promptly created a new, enhanced relativistic electron population with peak in phase space density on the inner radial gradient of the pre-shock outer radiation belt where the strong drift echo pulses observed by Van Allen Probe A were seen. Under the effects of the shock-induced electric field, the source population electrons E × B drifted radially inward, conserving the first and second adiabatic invariants and preserving phase space density along their trajectory. The enhancement near $L^* \sim 3.8$ identifies the freshly accelerated population of electrons, providing an important check on the shock energization scenario.

The March 2015 IP Shock event:

One of the largest geomagnetic storms observed during solar cycle 25 occurred during March 2015 and was driven by a CME preceded by an IP shock (Baker et al. 2016a). While the CME by itself was responsible for a strong long-duration (~days) electron energization and enhancement, the IP shock that preceded it injected relativistic and ultra-relativistic electrons, which resulted in drift echoes within minutes of the shock impact. REPT observed

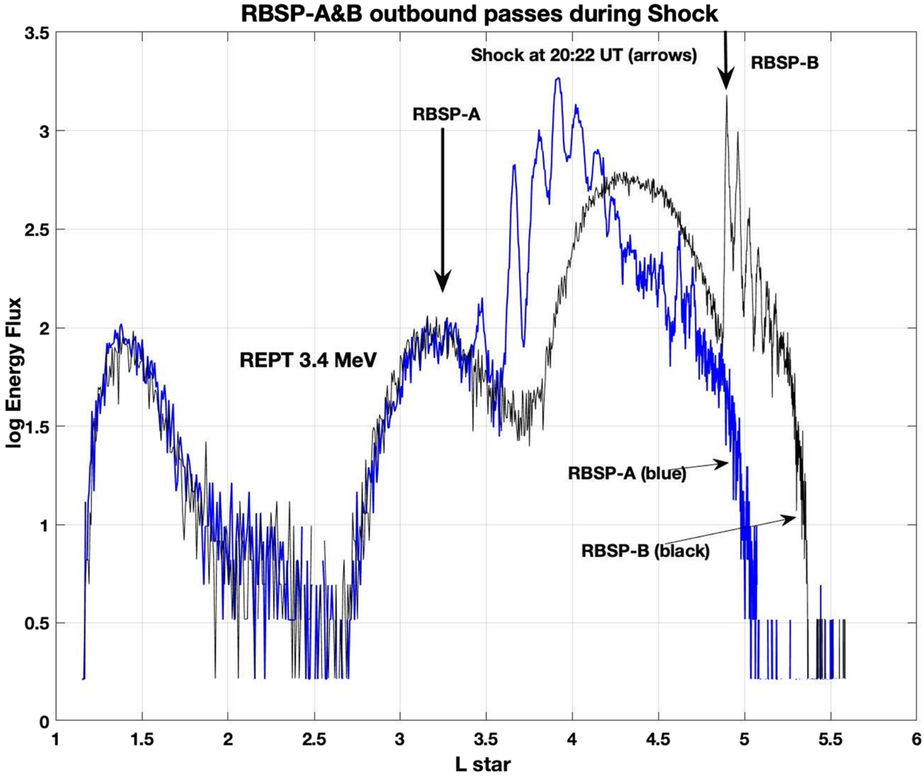

Fig. 35 Overlay of the Probe A and Probe B L^* profiles of 3.4 MeV REPT electron energy flux along the outbound orbits during which the shock effects were observed is shown. Arrows indicate the 20:22 UT time of shock observation at each spacecraft. At shock time, Probe B was at $L^* \sim 5$ and Probe A was further inward near $L^* \sim 3.3$

ultra-relativistic electrons of energies >6 MeV deep within the magnetosphere at $L \sim 3$ within 2 minutes of the shock impact.

The IP shock arrival and the relativistic electron response is shown in Fig. 37. The Figure shows REPT-A pitch angle resolved electron intensities. The figure shows electron intensities for the same energies as in Fig. 34 from 0430 UT to 0500 UT on 17 March 2015. During this event, the THEMIS probes were fortuitously located close to the magnetopause and observed the shock passage at the magnetopause. The time of IP shock arrival is indicated by the vertical line in Fig. 37. Velocity dispersed electron intensity increases are observed within about 3 minutes of shock arrival. As for the March 1991 event, electrons are injected locally and are energized by a electric field pulse travelling through the magnetosphere and has been modeled accurately by Li et al. (1993). Injected electrons stay bunched together for several drift periods even while slowly dispersing and result in drift echoes. The pitch angle resolved measurements by REPT clearly show that energetic electron intensities increased across all observed pitch angles, albeit the highest increases occurred for electrons at 90° pitch angles. REPT observations show that energization due to IP shocks is largely pitch angle independent, since the enhancements occur on times comparable to drift time scales. The drift time for an equatorially mirroring electron at $L \approx 3$ of energy $= 5.2$ MeV is about 5 min.

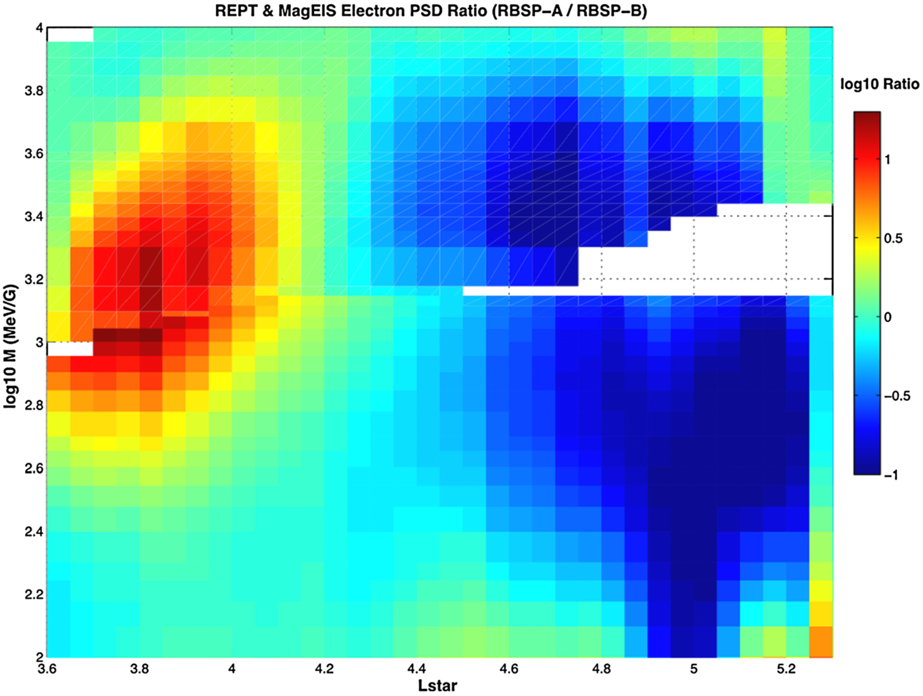

Fig. 36 Combined REPT and magEIS observations illustrate the change in the electron PSD determined as the ratio of the post-shock observations by Probe A to the pre-shock (background) observations by Probe B. The log of the ratio (Probe A PSD / Probe B PSD) for constant K (2nd invariant) is shown plotted against log μ (1st invariant) over a two-decade range of μ from 100 MeV/G to 10000 MeV/G and for L^* between 3.6 and 5.2

Figure 38 shows spin-averaged (top panel) and spin-resolved (bottom panel) electron spectra resulting from the IP shock as well those just prior to the shock arrival, the latter being measured at 04:40:02 UT. The dashed line show fits to exponential spectra of the form $j = j_0 \exp(-E/E_0)$ and yielded e-folding values of 0.48 MeV for the spin averaged and 0.70 MeV and 0.74 MeV for spectra of electrons at 90° and combined 60° and 120° respectively. The data show a clear spectral hardening for both spin-averaged and pitch angle resolved electrons. Details of the fits and statistical significance are discussed in Kanekal et al. (2016).

Knowing the drift velocity (Lew 1961) and electron energies, we can derive the location and the timing of the injection (see Kanekal et al. 2016). Figure 39 shows the azimuthal location of the peak values of 90° electron fluxes as a function of time of day for electrons of 2.6, 3.4, 4.2, 5.2, and 6.3 MeV. The drift speeds of electrons of each energy obtained from

$$< \dot{\phi} >= 0.12E\left(\frac{2+E}{1+E}\right)$$

(Kanekal et al. 2016, Equation (2)) are shown as solid color-coded lines at the times of observation of each energy respectively. The location and the time of the injection point is then given by the area of intersection of all the lines and yields an injection time of 286.2 ± 0.3 min, or 04:46:18 UT, and the injection location of -1.50 ± 0.15 rad, or $274.0° \pm 9°$. Using THEMIS probes measurement of the IP shock arrival at the magnetosheath it can be concluded that energetic electrons were injected and accelerated to ultra-relativistic in $\lesssim$2 min.

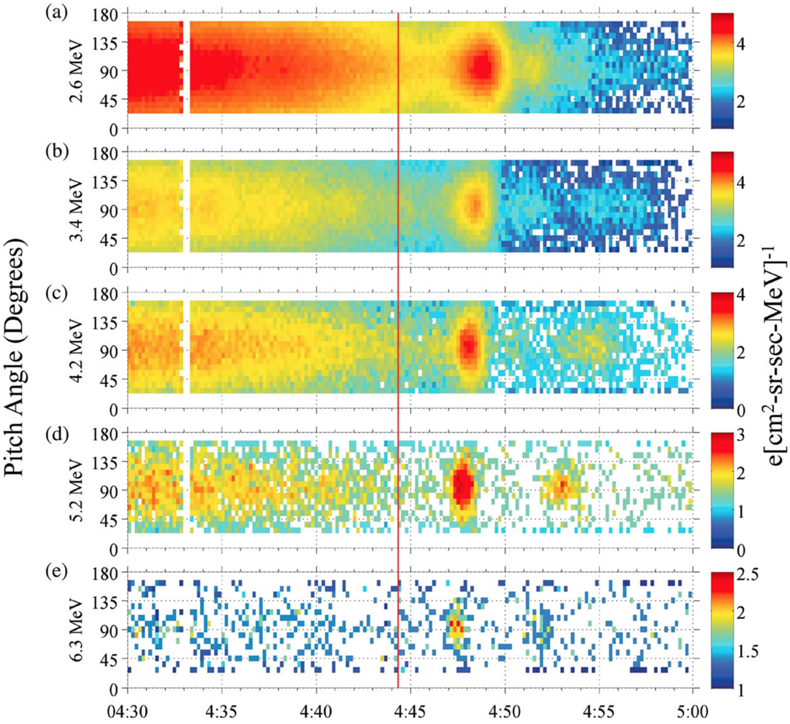

Fig. 37 Pitch angle-resolved energetic electron intensities measured by REPT-A on 17 March 2015 from 04:30:00 UT to 05:00:00 UT. The shock arrival time at the magnetopause as measured by the THEMIS probes is indicated by the vertical line

Van Allen probes measurements of electrons clearly show that the injected electrons were observed $\lesssim$2 min after the shock. The location of the initial shock impact as well as the time were determined using the velocity dispersion of energetic electrons observed by the REPT instrument. MagEIS measurements of electrons covering the energy range $E \approx 100$ keV to $E \approx 2$ MeV show that the IP shock had no effect on the lower energy end of the electron spectrum (~250-900 keV), which implies these electrons did not resonantly interact with the induced electric field. Both the spin-averaged and pitch angle resolved spectra show a clear spectral hardening and suggest that IP shock energization affects electrons over a broad range of pitch angles.

6.6.2 IP Shock Driven Advective Transport

An example from Hudson et al. (2017) is shown in Fig. 40, an MHD/particle simulation of the injection of particles during interplanetary shock occurring in March 2015 when the Van Allen Probes spacecraft were located in the nightside magnetosphere. In these simulations, upstream solar wind conditions are used as a boundary condition driving a magnetohydrodynamic (MHD) simulation of the solar wind/magnetospheric interaction. Test particles representing trapped energetic populations are then driven by the simulation results to provide a global picture of the physics of the injection. In Fig. 40, observations of the initial energetic particle distribution (bottom panel) were used to weight test particle results from 3d simulations of the radiation belt response at RBSP-B. The results of the interaction of the

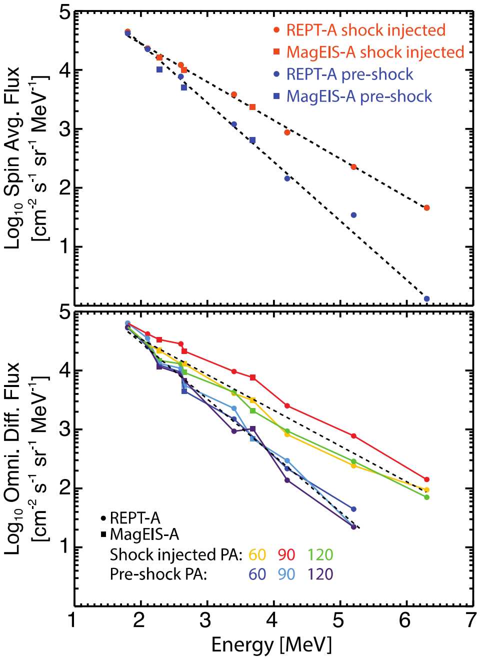

Fig. 38 Electron spectra measured by REPT-A (solid circles) and MagEIS-A sensors (solid squares). Shock-injected spectra are shown in red and pre-shock spectra are shown in blue. The top panel shows spin-averaged spectra and the bottom panel shows spectra of electrons at 60°, 90°, and 120° pitch angles and are color coded as shown in the panels. The dashed lines indicate exponential fits to the spectra. It is evident that IP shocks rapidly energize electrons to ultra-relativistic energies and inject them deep into the magnetosphere. Furthermore, the observations show that the injection mechanism is pitch angle independent and injects particles over a range of pitch angles

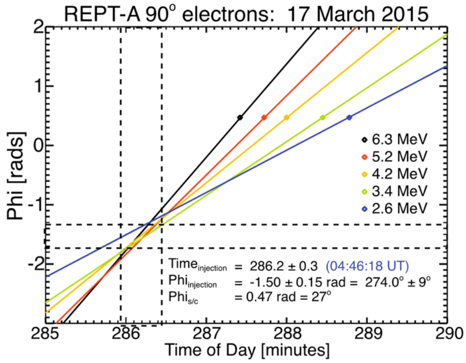

Fig. 39 REPT-A measurements of 90° peak electron fluxes as a function of time of day on 17 March 2015. Solid lines have slopes corresponding to the respective drift speeds and passing through the observed locations and times

initial trapped population with the shock are indicated in the top panel. Clear drift echoes are observed at the time of the shock. Lower-energy particles take longer to drift from the dayside injection region to the nightside location of the spacecraft, resulting in the characteristic energy dispersion signatures (longer period drift echoes at lower energies) evident in the top panel of Fig. 40.

6.7 Radial Transport and Diffusion

6.7.1 Drift Effects

Processes acting on trapped energetic particles on timescales commensurate with their drift period may violate the 3rd (drift) adiabatic invariant while conserving the gyro- and bounce-invariants. The third invariant is commonly used to order the particle distribution in terms

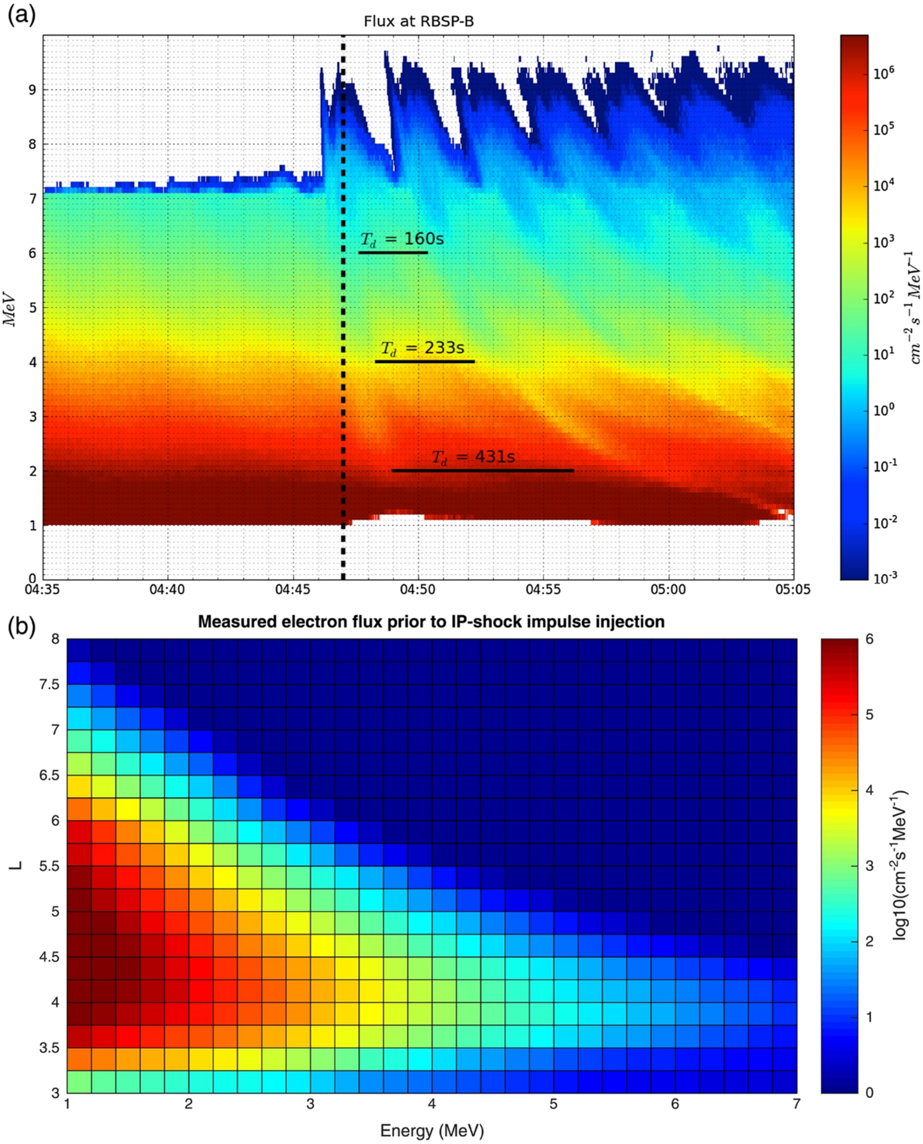

Fig. 40 MHD/test particle simulations of the prompt injection and transport of particles during the March 2015 injection event, showing the characteristic energy dispersion associated with such injections. The observed initial conditions used to weight the simulated particles is shown in the bottom panel. After Hudson et al. 2017

of radial distance through the Roederer L^* parameter (Roederer 1970), inversely related to the total flux enclosed by the drift orbit of the particle. The gyro- and bounce- invariants provide a measure of the particle energy perpendicular and parallel to the local magnetic field, respectively. Thus, processes violating the drift invariant will lead to transport into regions of larger or smaller magnetic field strength, while the concurrent conservation of the gyro- and bounce- invariants lead to proportional changes in energy. In most circumstances inward transport of energetic particles will lead to an increase in energy of that population.

There are numerous processes which might lead to radial transport. Broadly, they may be distinguished as either advective processes, whereby a population is coherently transported from one region of the magnetosphere to another; or diffusive processes, in which the stochastic radial motion of particles leads to the evolution of the distribution function in a manner that tends to smooth out gradients in that distribution (Schulz and Lanzerotti 1974). An early example of the advective transport of particles occurred during the March 24, 1991 Storm Sudden Commencement (Blake et al. 1992; Li et al. 1993). Here particles were promptly (on a timescale of minutes) injected into low L-shells, forming a persistent new radiation belt near the nominal radiation belt slot region. While dramatic, such events are relatively rare. More common are the episodic injection of particle from the near-Earth magnetotail into the inner magnetosphere (e.g. Reeves and Henderson 2001). These particles may enhance the ring current (e.g. McPherron 1997; Elkington et al. 2005), provide source and seed populations for subsequent acceleration through high-frequency (kHz) wave-particle interactions (e.g. Jaynes et al. 2015), and may directly contribute to the energetic populations of the radiation belts themselves (Kim et al. 2000; Ingraham et al. 2001; Dai et al. 2015a).

Stochastic radial transport, more commonly referred to as radial diffusion, results from the interaction of particles with a spectrum of waves with frequencies commensurate with the drift frequency of the particles (e.g. Elkington et al. 2003), although repetitive advective processes such as substorms may lead to the diffusive radial transport of particles over long-enough timescales (Chen et al. 1992; Sarris et al. 2017, 2020). Radial diffusion will tend to move particles in aggregate in the direction opposite the prevailing gradients of the local phase space density. That is, particles will be transported Earthward in situations where the distribution function increases at higher L shells, and transported outward towards the magnetopause in regions where the particle distribution decreases as higher L. Thus radial diffusion may act to either energize particles (inward transport from larger L) or act as a loss of particles in the radiation belts (outward transport to the magnetopause), depending on the functional dependence of the phase space density with L.

The REPT instrument on the Van Allen Probes mission provided an opportunity to study the radial transport of particles in the radiation belts. Here we review a few of the highlights from the Van Allen Probes era.

6.7.2 Stochastic Transport

Radial diffusion results from the interaction of energetic particles with a spectrum of waves satisfying a drift-resonant condition $\omega = m\omega_d$, where ω is the wave frequency, ω_d is the particle drift frequency, and m represents the azimuthal structure of the waves (Elkington et al. 2003, 2006). The waves satisfying this condition are categorized as Pc-5 waves (Jacobs et al. 1964), and have frequencies in the mHz range. These waves are ubiquitous in the magnetosphere, but the power spectral density of these waves can vary over orders of magnitude with magnetospheric activity (e.g. Ali et al. 2015). Waves at Pc-5 frequencies are often characterized as resulting from convective-type electric fields based on an electrostatic potential (electric diffusion coefficients); resulting from fluctuations in the magnetic field alone (magnetic diffusion coefficients); or both magnetic field fluctuations and the electric field induced by these fluctuations through Faraday's Law (electromagnetic diffusion). Analytic forms for each of these types have been developed, allowing estimates of the rates of diffusive radial transport based on measurements of the power in the wave spectrum (Falthammar 1966, 1968; Cornwall 1968; Fei et al. 2006). Rates of radial diffusion in the magnetosphere are commonly expressed as the inverse of the diffusion coefficient with units of time.

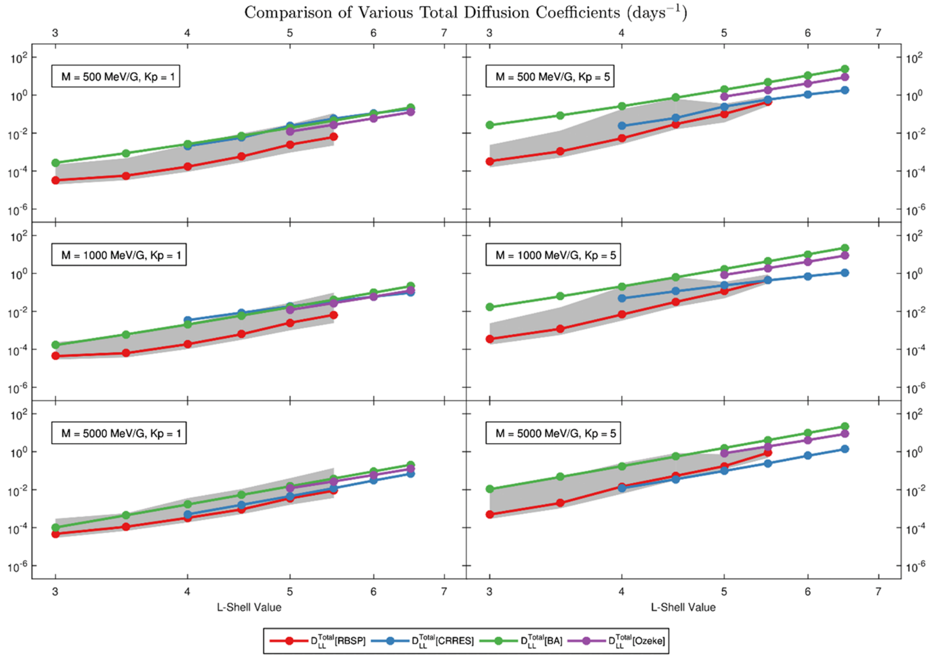

Fig. 41 Radial diffusion coefficients at a number of first invariants as observed over the Van Allen Probes' lifetime (red line), as compared to those observed during the CRRES mission and via two popular empirical models. The grey shaded region shows the 5th and 95th percentile estimates for the Van Allen Probes' measurements. After Ali et al. (2016)

Ali et al. (2016) undertook a statistical study of diffusive transport in the radiation belts. Figure 41 shows the total (electric plus magnetic) radial diffusion coefficients at REPT energies, based on electric and magnetic field measurements from the Van Allen Probes, along with comparisons to CRRES estimates of the diffusion (Ali et al. 2015) and to two popular empirical models (Brautigam and Albert 2000; Ozeke et al. 2014). The Van Allen Probes REPT-energy estimate (red line) was based on measurements taken from September 2012 to August 2015, binned according to radial distance and magnetospheric activity (via the Kp index). The grey shaded regions indicate the 5th and 95th percentile estimates of the diffusion coefficient during this period, which can be seen to span an order of magnitude or more at most *L* values. The large variation in magnitudes and the underlying log-normal distribution of wave power suggests that the proper measurement of central tendency in these calculations is a median measure, rather than a measure of the mean. The study indicated that diffusion due to magnetic field fluctuations was only weakly dependent on energy, while the electric field coefficients were essentially independent of energy. The authors also found that diffusion due to electric fields was statistically the dominant driver of stochastic radial transport in the radiation belts, often exceeding that due to magnetic field fluctuations by as much as two orders of magnitude.

Ozeke et al. (2019) modeled the flux dropouts and subsequent acceleration of REPT electron observations during the March 2013 and March 2015 events. They found that the simulations accurately reproduced particle dynamics during both events, but only if the simulation inputs included event-specific diffusion coefficients inferred from measurements rather than from a statistically derived diffusion formulation. This is consistent with some previous

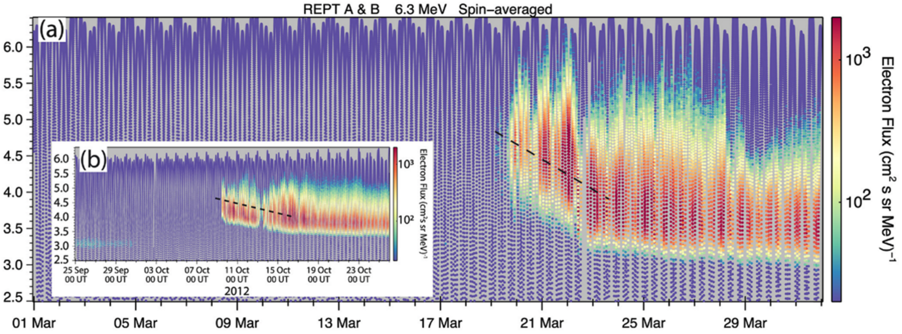

Fig. 42 (**a**) Inward diffusive transport and acceleration of ultrarelativistic (6.3 MeV) electrons during the March 2015 geomagnetic storm. (**b**) Inset shows previous strong storm of October 2012 with a much lower rate of transport. (Jaynes et al. 2018)

estimates of the effect of diffusion during geomagnetic storms (e.g. Riley and Wolf 1992), and follows from the wide range of possible radial diffusion rates at a given level of magnetospheric activity as found by Ali et al. (2015, 2016). Olifer et al. (2019) looked specifically at the March 2015 event, and found a relationship between the phase of the storm and rates of radial diffusion. In particular, rates of electric diffusion were reduced from those expected by statistical studies during the main phase of the storm, leading (in contrast to the results of Ali et al. (2016)) to periods of time where the magnetic diffusion exceeded the effects of electric diffusion.

The overall effect of radial transport on the distribution of energetic particles depends on the radial gradient of the distribution's phase space density. Examples of energization and flux increases result when the radial gradient points outward from Earth, leading to inward transport of particles in accordance with Fick's First Law (Green and Kivelson 2001). Examples of inward transport and acceleration at REPT energies were observed for both electrons (e.g. Kress et al. 2014; Li et al. 2016d, 2017c; Su et al. 2015; Ozeke et al. 2018; Zhao et al. 2019a, 2019b) and protons (e.g. Selesnick et al. 2016).

An example of the fast-inward diffusion of ultra-relativistic electrons measured by REPT for a population injected during the large March 2015 geomagnetic event is shown in Fig. 42, via Jaynes et al. (2018). This study looked at electrons up to ∼8 MeV accelerated in the absence of high-frequency (kHz) wave activity, suggesting that the inward transport and acceleration was primarily or entirely the result of ULF wave-driven diffusion. The inward transport of 6.3 MeV electrons over ∼1.5 R_E indicated in Fig. 42 occurred on a time scale of approximately two days. Concurrent electric and magnetic field observations were applied to the diffusion results suggested by Ali et al. (2016) shown in Fig. 41 above. The power spectral density in the ULF waves acting on electrons during this period of time was more than sufficient to produce the inward diffusive transport indicated in Fig. 42.

Zhao et al. (2018) examined the ultra-relativistic electron response measured by REPT during a much more moderate storm occurring in April 2017. They too saw inward radial transport of electrons at a range of energies >3 MeV, as indicated in Fig. 28. The motion of the phase space density front inward in time in opposition to the radial gradient of phase space density suggests that inward transport and acceleration of electrons at these energies may be a dominant effect at a range of geomagnetic activity levels.

Local acceleration of electrons (due to, for example, wave-particle interactions with whistler-mode chorus) can produce a peak in the phase space density in the heart of the radiation belts (e.g. Thorne et al. 2013b; Reeves et al. 2013). Inward incursions of the magnetopause due to solar wind pressure increases can lead to “magnetopause shadowing”, where particles’ drift orbits intersect the magnetopause and are lost to the solar wind. This effect can similarly produce a peak in the phase space density at lower L values by depleting populations nearer to the magnetopause. In the case of either local acceleration or magnetopause shadowing, the resultant peak in the phase space density distribution can lead to outward radial transport of particles, with populations losing energy as they move outward in accordance with conservation of the drift invariant. These effects at REPT energies were studied in the Van Allen Probes era by Turner et al. (2014); Hudson et al. (2014); Mann et al. (2016); Schiller et al. (2017); Xiang et al. (2018); and Olifer et al. (2018), among others.

In Fig. 43 we show diffusive simulations of an extended (>10 days) dropout of ultrarelativistic radiation belt electrons that was observed in September 2014 (Ozeke et al. 2017). This study compared Van Allen Probes observations of the electron flux with simulations that variously included or excluded known radiation belt loss and acceleration mechanisms such as wave-particle interactions with plasmaspheric hiss or whistler-mode chorus, and rapid extinction due to magnetopause shadowing. The authors of this study showed that the morphology of the extended dropout was best described in terms of the boundary conditions and diffusive action of ULF waves alone, without the need for hiss or chorus effects.

6.8 Atmospheric Coupling Studies

One important loss mechanism of energetic electrons from the radiation belts is through precipitation into the Earth atmosphere (Thorne 1974; Baker et al. 1987). The depth into the atmosphere that particles can penetrate and produce ionization of neutral atmospheric constituents is quite dependent on the particle species and on the kinetic energy. Figure 44 illustrates in broad terms where in altitude energy electrons, solar protons, and very energetic galactic cosmic rays would be expected to have their principal energy deposition and ionization effects (from Baker et al. 2001). As the diagram makes clear, the high-energy electrons detected in the radiation belts by the REPT sensors ($E \gtrsim 1.5$ MeV) would largely be expected to deposit their precipitated energy below 70-80 km altitude.

The consequence of precipitating particle energy in the middle atmosphere can be quite important, especially in the winter hemisphere and in the polar (high-latitude) regions.

For Earth’s atmosphere, nitric oxide (NO) in the upper atmosphere above $\sim$70 km is an essential molecule because it contributes most to the radiation balance between the Earth and outer space (e.g., Knipp et al. 2017). The amount of NO in the upper mesosphere and lower thermosphere depends (see Fig. 44) on the flux of solar X-ray and extreme ultraviolet (EUV) radiation that contributes to production of NO (e.g. Barth et al. 1988). In addition, precipitating energetic electrons including auroral particles also contribute to NO production in the polar regions (e.g., Baker et al. 2001; Barth et al. 2003) and radiation belt particles can contribute to NO production at mid-latitudes and subauroral regions (Thorne 1974; Baker et al. 1979). On the other hand, the loss process for NO is mainly due to photodissociation by ultraviolet (UV) radiation (e.g. Barth et al. 2003). Therefore, it is known that the NO amount in the polar region during the polar night reaches a maximum value due to a lack of any loss processes (e.g., Sheese et al. 2011).

Figure 45 shows L-versus-time plots of the 1.8 MeV (upper) and 4.2 MeV electron fluxes, respectively, observed with the REPT instrument. Data are shown from 1 September 2012 to 10 November 2018. An interesting feature appears during the period from October 2013 to August 2014. During this period, no significant electron fluxes at 4.2 MeV were detected above background in any of the sampled L-shells. As discussed by Baker et al. (2019a),

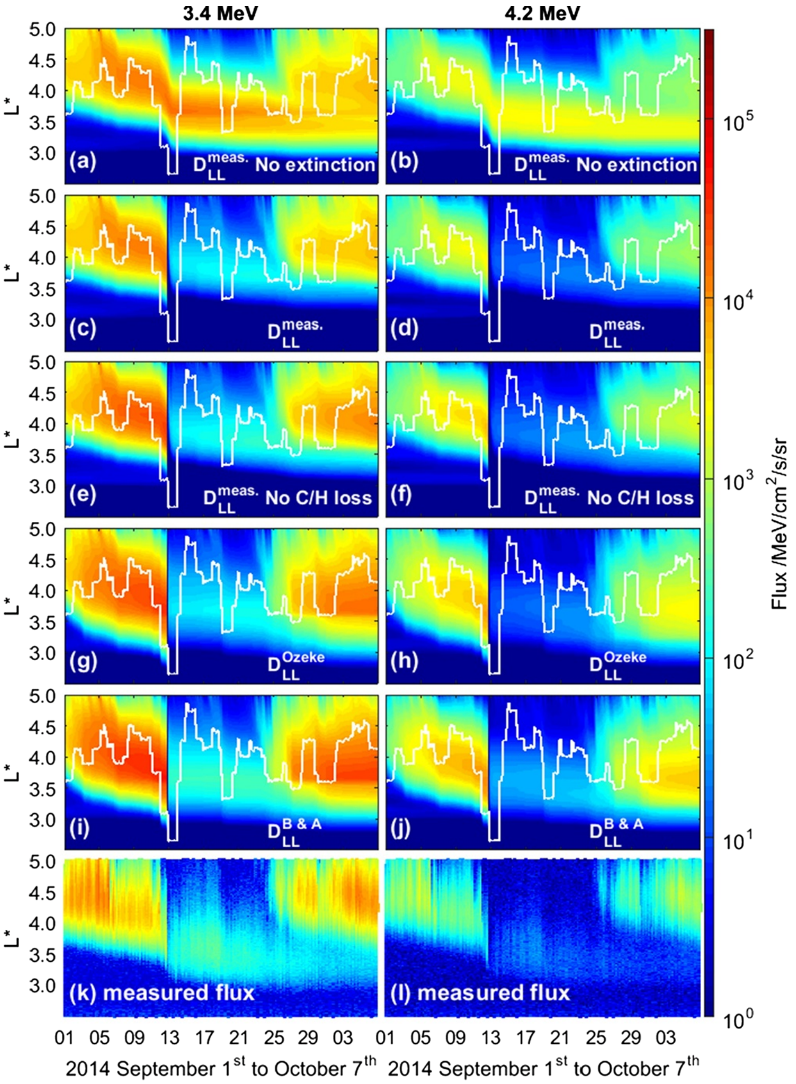

Fig. 43 Simulation of the electron extinction event occurring in September-October 2014, driven by boundary conditions at $L = 5$ and including or excluding a number of known loss mechanisms. Simulation results indicated that the diffusive action of ULF waves coupled with magnetopause shadowing may be responsible for the observed dropout (Ozeke et al. 2017)

during this entire period only some very minor short-term flux enhancement were seen. The 1.8 MeV electron flux during this 2014 period was also less than that in any other extended period of the VAP mission lifetime. Such a phenomenon (that the energetic electrons trapped in the radiation belt disappear) might more reasonably occur in the solar minimum period, but at this time, it was near the solar cycle 24 sunspot maximum. Therefore, it was an anomalous situation that the ultra-relativistic energetic electrons in the radiation belt disappeared for nearly one year in the maximum.

Fig. 44 Modeled ionization rates for various altitudes in the Earth's atmosphere due to solar photon inputs, auroral electrons, relativistic (radiation belt) electrons, solar protons, and galactic cosmic rays (as labeled). (From Baker et al. 2001)

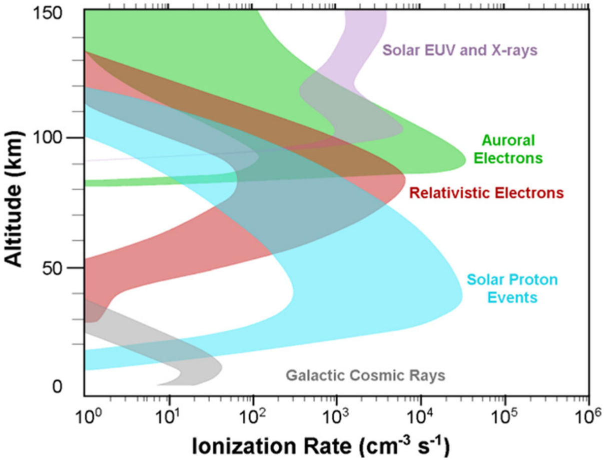

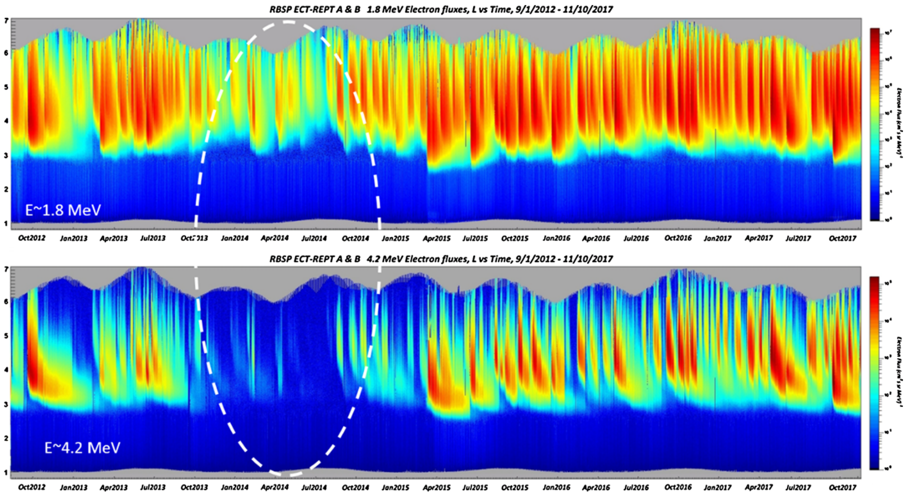

Fig. 45 Color-coded fluxes of electrons measure by REPT sensors for the five-year period from Sept. 2012 through Nov. 2017 in the L vs. time format. The upper panel shows $E = 1.8$ MeV electrons and the lower panel shows $E = 4.2$ MeV electron fluxes. The dashed oval highlights a period in late 2013 and 2014 where the relativistic electrons were essentially entirely absent in the magnetosphere

Figure 46 in its upper panel shows the time series of the observed column amount of NO over Syowa Station and its 30-day average from January 2012 to December 2017 (Nagahama et al. 2020). In this data set, the maxima in the Antarctic winter season (except for the 2014 season) clearly appears. There is no significant difference for most of the years, but during winter, the column amount of NO in winter of 2014 was significantly lower than other years. The typical value of the maximum in the 30-day average data was estimated as 2.0×10^{15} cm^{-2}. On the other hand, the value in 2014 was half as much (1.1×10^{15} cm^{-2}). In addition to the seasonal variation, there were several-day increases of the NO column amount, which are known to be associated with energetic particle precipitation events (Isono et al. 2014). The lower panels of the figure show the complete absence of the multi-MeV electrons during the austral winter of 2014.

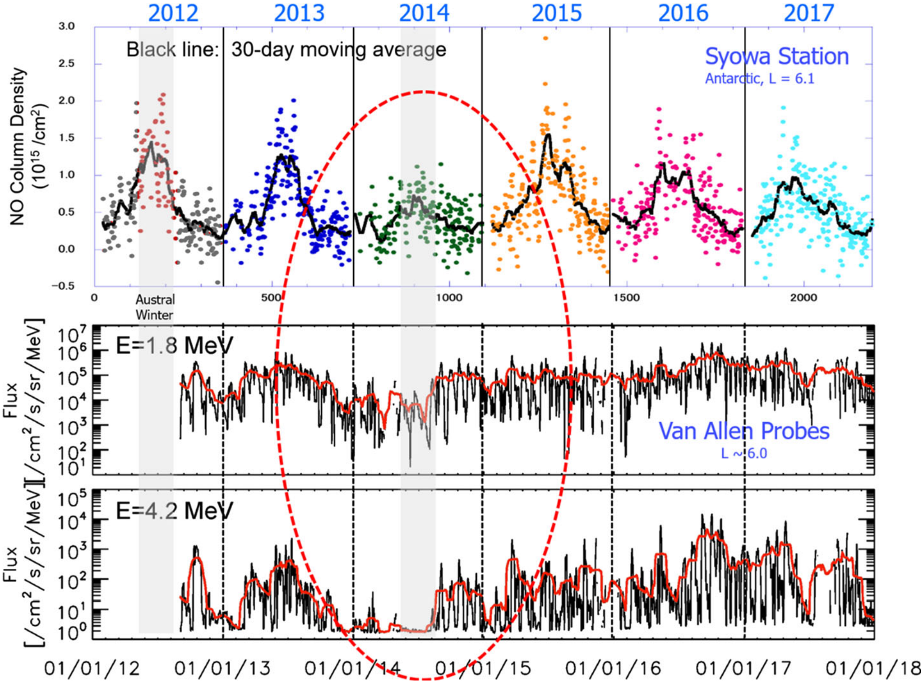

Fig. 46 The upper panel shows the time series of the observed column amount of NO over Syowa Station and its 30-day average from January 2012 to December 2017 (Nagahama et al. 2020). A maximum in the Antarctic winter season (except for the 2014 season) clearly appears. The lower panels of the figure show the complete absence of the multi-MeV electrons during the austral winter of 2014 compared to other years, indicating that the relative absence of nitric oxide above ∼70 km altitude over Antarctica in 2014 was due to paucity of relativistic electron precipitation during that time

Thus, in these recent studies, it has been shown that the anomalously low amounts of nitric oxide (NO) in the austral winter of 2014 measured at Syowa Station ($L = 6.1$) in Antarctica were probably caused by the nearly total disappearance of energetic electrons in the radiation belt for much of a year period (Nagahama et al. 2020). A decrease of the column amount of NO in the upper mesosphere and lower thermosphere occurred at the same time in the polar winter of 2014. The correlation between annual maxima of monthly means of the column amount of NO at Syowa Station and of the electron fluxes at the corresponding position in the outer radiation belt, indicates that both the NO and the electron fluxes were much smaller than those in the other winters. Thus, these rather surprising results show that multi-MeV electrons can play a controlling effect on NO even at altitudes (>70 km) in the polar winter under some conditions.

7 Science Highlights: Inner Zone

7.1 Inner Belt Morphology

The first discovery in space science, six decades ago, was the Earth's inner radiation belts, which centered near 1.5 Earth radii (R_E) from the center of the Earth at the equator and consist of high-energy protons (tens of MeV to GeV energies) and relativistic electrons.

Before the Van Allen Probes era, it had been well understood that the energetic protons in the inner belt can be produced from the decay of energetic neutrons, in a process known as Cosmic Ray Albedo Neutron Decay (CRAND). The energetic neutrons are made by the direct interaction of high-energy cosmic rays, many of which are protons likely produced by supernovae in our galaxy (e.g., Blasi 2013), with atmospheric neutral atoms, mostly nitrogen and oxygen, in the upper atmosphere. Such neutrons are also called knock-on neutrons with energies from many MeV to multiple GeV and a main source of the inner belt protons. However, a larger source of neutrons comes from the evaporation process that produces lower-energy neutrons. Such lower-energy neutrons are emitted with roughly a Maxwellian distribution peaked around 1 MeV from excited nitrogen and oxygen due to cosmic ray perturbations (e.g., Hess et al. 1961), and could be a source of the relativistic electrons in the inner belt.

Solar energetic protons (SEPs) are another source of 10s to 100s of MeV protons deep inside Earth's magnetosphere ($L < 4$) and these trapped SEPs may survive magnetospheric perturbations and diffuse inward to the inner belt. However, the relative contribution of these solar protons to the inner belt had not been well measured and was only estimated based on theoretical modeling (e.g., Selesnick et al., 2007).

The major science advancements (highlights) in the understanding of the inner radiation belts that has been associated with Van Allen Probes/REPT instrument can be summarized below:

(1) REPT measurements have put an upper limit on the >1 MeV electrons in the inner belt and this upper limit is actually lower than the AE8 and AE9 model results, which lead to the outstanding questions: (i) is this because of solar activity being low during the Van Allen Probes era? or (ii) because previous measurements on which AE8 and AE9 were based were inaccurate data (Li et al. 2015b; 2017a)?;
(2) Recent measurements from the Relativistic Electron and Proton Telescope integrated little experiment (REPTile) onboard Colorado Student Space Weather Experiment (CSSWE) CubeSat showed for the first time that CRAND (from low-energy neutrons) is actually the main source of the inner radiation belt near its inner edge (Li et al. 2017b). REPTile is simplified and miniaturized version of REPT (Li et al. 2012, 2013) (see Sect. 9 about Future Prospects);
(3) The dynamical evolution of inner belt protons and inward diffusion of SEPs were first unequivocally demonstrated with REPT measurements; and
(4) The REPT measurements have enabled, for the first time, the detailed study of the long term trends in the energetic proton population in the inner magnetosphere, which includes the inward diffusion of trapped SEPs to $L < 2$, decay at lower L (<1.3) due to atmospheric drag, and storm-time loss and recovery at higher L (>2.5).

Highlight (1): REPT (Baker et al. 2013a) and MagEIS (Blake et al. 2013) onboard Van Allen Probes are heavily shielded but are still subject to background from inner belt protons. Detailed analysis based on REPT measurements has put an upper limit on the >1 MeV electron intensities in the inner belt, which is lower than the AE8 and AE9 model results. The measured upper limit values may be due to low solar activity during the Van Allen Probes era or because previous measurements on which AE8 and AE9 were based were inaccurate (Li et al. 2015b, 2017a). However, it is known that >1 MeV electrons did penetrate into the inner belt during strong solar wind drivers before the Van Allen Probe era (Blake et al. 1992; Li et al. 1993, 2017a; Baker et al. 2004). Figure 47 shows the upper limit of the energy spectrum based REPT measurements, compared with the energy spectra from AE8 and AE9 (and other measurements).

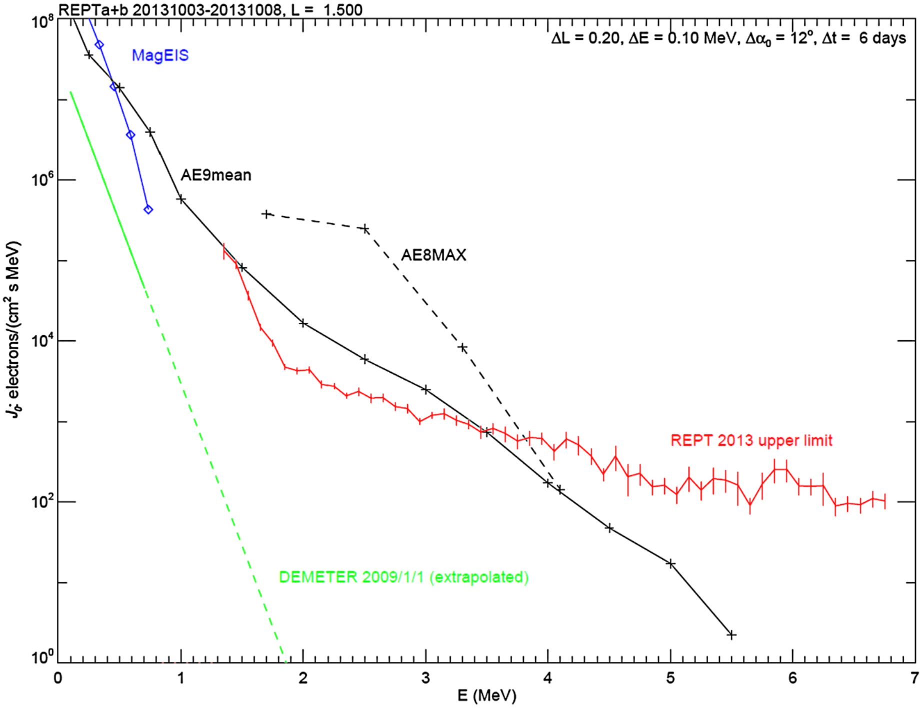

Fig. 47 Fig. 11 of (Li et al. 2017a) Omnidirectional equatorial electron energy spectra at $L = 1.5$. The average spectrum derived from REPT PHA data (red) likely results from high-energy protons rather than electrons and therefore is an upper limit on the actual electron intensity. Bin widths used in the data analysis are listed. Equivalent model spectra from AE9 VI.2 (solid black) and AE8MAX (dashed black) are shown for comparison. Also shown are MagEIS data (blue) of selected energy channels during the period of 24 February to 1 March 2013 and the exponential energy spectrum measured on the low-altitude (not equatorial) DEMETER satellite during January 2009 for $E < 0.8$ MeV (solid green) and extrapolated to higher energies (dashed green)

Highlight (2) Soon after the discovery of Earth's Van Allen radiation belts six decades ago it was recognized that the decay of the knock-on neutrons is the main source of trapped energetic (above tens of MeV) inner belt protons. It has recently been recognized that the decay of evaporation (low-energy) neutrons contributes to energetic electrons (up to 782 keV) and is the dominant source of energetic electrons at the inner edge of the inner belt (Li et al. 2017b; Zhang et al. 2019; Xiang et al. 2020). Figure 48 shows electron flux data for 0.5-MeV electrons measured from CSSWE/REPTile. The data have been divided into ranges of L. If the electrons drift around the Earth without encountering the dense atmosphere below, then they are considered stably trapped and their intensity can reach high levels. REPTile observes such stably trapped electrons only at $L > 1.15$ in the South Atlantic Anomaly (SAA), where the magnetic-field strength is weakest, as shown in Fig. 48 by the high intensity levels in the Southern Hemisphere near longitude 300° for $L > 1.15$. For $L < 1.15$ there is a gap in data coverage near longitude 300°. This is a result of electron-drift shells that attain minimum altitudes, in the SAA, below the satellite altitude. However, on each side of the gap the local magnetic field is seen to be equal to the field-line minimum value—that is, CSSWE is already at the location of the field-line minimum, a necessary consequence of the highly inclined orbit. Had any stably trapped electrons existed on these drift shells they

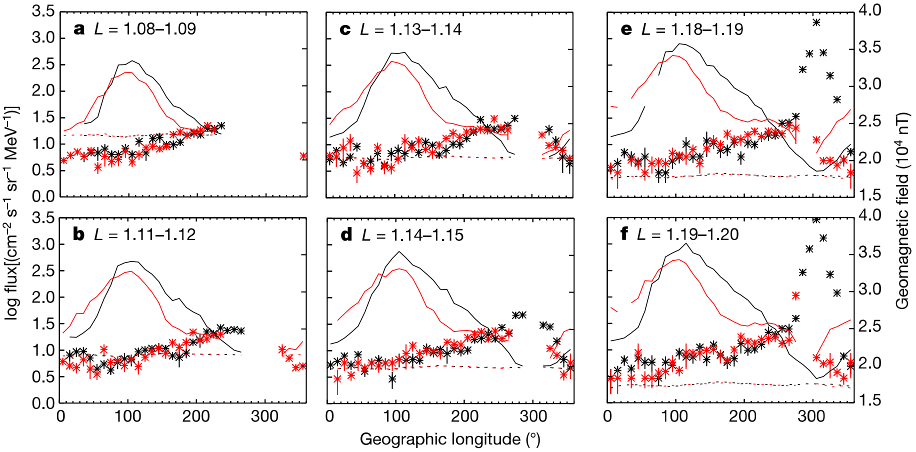

Fig. 48 Fig. 3 of (Li et al. 2017b) Electron flux as a function of longitude in different L shells for the period 7–10 October 2012. **a**–**f**, Measurements of 0.5-MeV electrons at different L values in the southern (black asterisks) and northern (red asterisks) hemispheres. Black and red lines show the local magnetic fields for the southern and northern hemispheres; the dotted line shows the minimum magnetic field along the field line on which CSSWE is located. Before averaging, data points ten times larger or smaller than the average of the two neighboring points were filtered out, amounting to 2.6% of the total data. N varies from 1 to 52 for this time period

would have been observed at the field-line minimum. Therefore, none were missed in the data gap, and the existence of the gap actually guarantees that there are no stably trapped electrons on such L shells. This suggests that all the electrons measured at $L < 1.15$ are quasi-trapped electrons, which will be lost within their drift time period, ~1.5 hours. The fact that such quasi-trapped electrons are always observed at the low L-shells suggests that there is a constant source supplying these electrons. This constant source has to be from CRAND (Li et al. 2017b) that occurs all the time.

Highlight (3) will be described in the subsections 7.3.

7.2 PHA Analysis Results

All particle events measured by REPT are pulse height-analyzed for binning into electron and proton channels that are the primary data products. A subset, namely, one event every 12 ms, are also included in another data product that includes individual pulse heights, proportional to energy deposit, from all nine REPT detectors. These “PHA data”, available starting from October 2013, are particularly useful for diagnostic purposes and for studies requiring extra care in performing background subtraction.

Measurements of inner radiation belt protons suffer from significant background due to the presence of high-energy protons that can penetrate the shielding material surrounding REPT, where they lose a significant fraction of their energy before reaching the silicon detectors, and then appear in data channels reserved for lower energy protons. The PHA data have been used to identify such high-energy protons and significantly reduce the background levels.

Only protons arriving with high incidence angles relative to the REPT axis, outside the nominal FOV 32 deg, can lose sufficient energy in shielding material to appear as lower energy protons. These are identified by estimating the incidence angle from the set of measured energy deposits using a probabilistic method based on proton straggling functions in

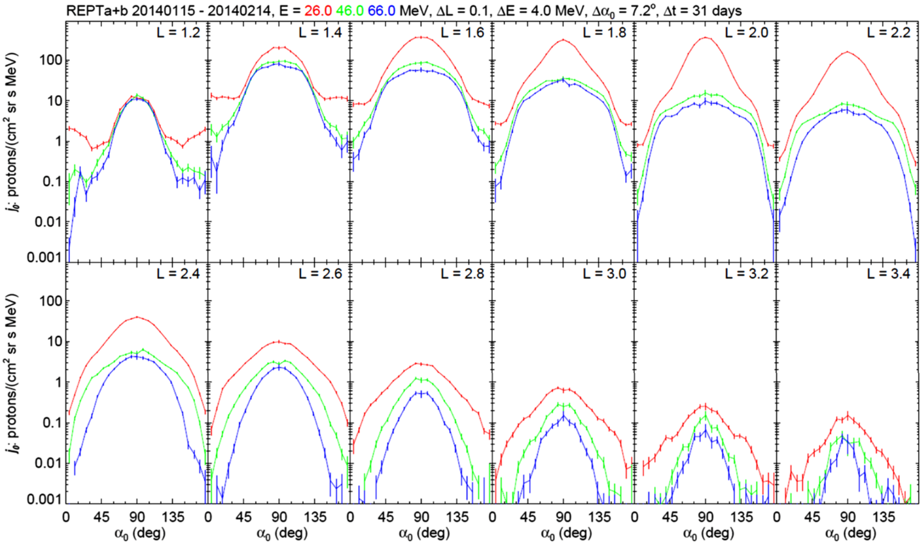

Fig. 49 Fig. 4 of Selesnick et al. (2014) Measured average proton equatorial pitch angle distributions from 15 January to 14 February 2014, at selected L values from 1.2 to 3.4, from a combination of REPT-A and REPT-B PHA data (Selesnick et al. 2014). Three proton energies, identified by color, and full bin widths are listed above. Statistical error bars are shown at the center of each pitch-angle bin

silicon (Selesnick et al. 2017). At least two energy deposits are required and the method therefore works well for protons that stop in any of detectors R2 through R9, allowing a straightforward analysis of signals from protons in the energy range 24-76 MeV.

Sample results of such analysis are illustrated in Fig. 49 (Selesnick et al. 2014). It shows equatorial pitch angle distributions of protons, measured at three selected energies and twelve selected L values. Background was particularly severe for $L < 1.5$, where intense high-energy protons are present. However, this has been reduced to the low levels shown in the loss cones, at high and low pitch angle where no stably trapped protons are expected, compared to the higher trapped-proton intensity near 90 deg. Even lower background is evident at higher L values, where loss cones are narrower.

After identifying high-energy protons from outside the FOV it was also possible to use them for extending the useful energy range of inner-belt proton data. This required computing response functions at all incidence angles while accounting for the effects of shielding material. These apply directly to the computation of high-energy proton intensity and also allow a subtraction of high-energy contamination in the lower energy proton data for which only the R1 detector is triggered, providing an extended energy range of 17–400 MeV. However, because incident energy cannot be uniquely determined for the high-energy protons, some smoothing of the resulting proton distributions is required, reducing their resolution in energy, L-shell and equatorial pitch angle. Sample results of this method are shown in Fig. 50, updated from Selesnick et al. (2018). Monthly averages of proton L-shell distributions are shown for selected energies (left) and energy spectra are shown for selected L values (right).

Electron signals in REPT are normally well separated from those of protons due to their significantly smaller energy deposits. However, the high proton intensity of the inner belt also introduces significant difficulties into inner belt electron data analysis, for two reasons: (1) energy deposits of relativistic protons and electrons are of similar magnitude; and (2) a

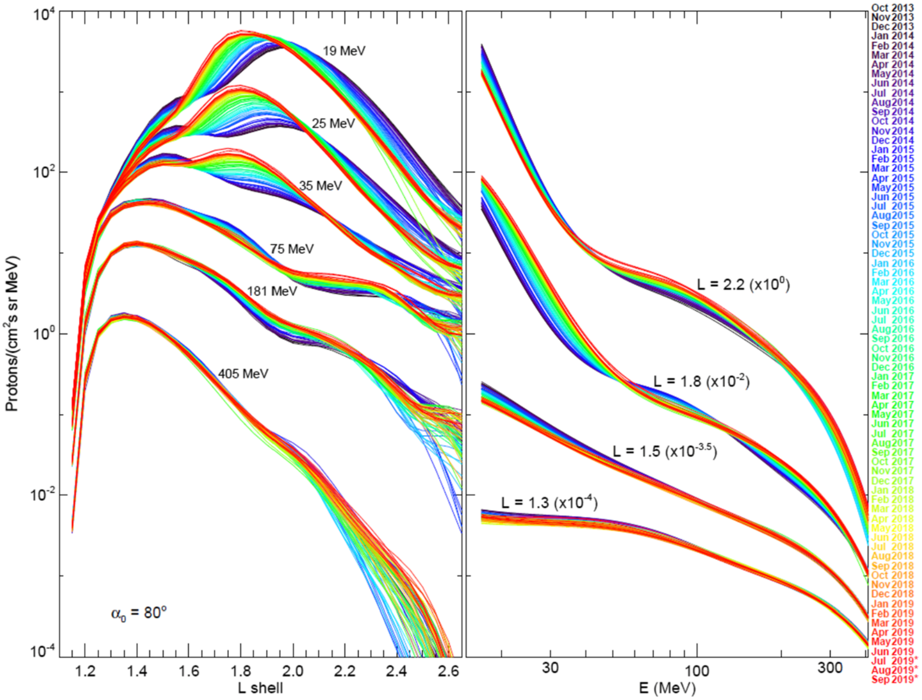

Fig. 50 Radiation belt proton modeled L shell distributions at selected energy (left) and energy spectra at selected L (right, with indicated scaling factors), at 80 deg equatorial pitch angle, derived from smoothed REPT-A and REPT-B PHA data, for color coded monthly averages (updated from Selesnick et al. (2018)); the last three months, indicated by *, are from REPT-A only)

fraction of sub-relativistic proton signals are degraded due to detector edge effects and reduced in magnitude to those of electrons. The PHA data have been used in an attempt to determine inner belt intensity of electrons with kinetic energy above 1.5 MeV but it was found that, if such electrons are present, their signals could not be separated from omnipresent proton contamination and only an upper limit could be determined (Li et al. 2015b). Accurate electron intensity measurements could be made only for $L > \sim 2.7$.

7.3 Long-Term Trends

Inner belt measurements derived from PHA data, as described in Sect. 7.2, have provided detailed trapped proton intensity distributions as a function of L shell, energy, equatorial pitch angle, and time from October 2013 to September 2019. This is a significantly longer interval than was available from CRRES, the only satellite that has provided measurements from a similar, near-equatorial orbit where the entire trapped particle population is accessible. This has enabled studies of long-term trends in the trapped proton population. Three aspects of the measured variability have been compared to theoretical expectations and model predications: inward diffusion of trapped solar protons, decay at low L due to atmospheric drag, and storm-time loss and recovery at higher L.

Inward diffusing protons are apparent from changes to the intensity peak observed at lower energies, that is rising and moving inward from $L = 2$ to $L = 1.8$, as shown in Fig. 50. These measurements are consistent with inward radial diffusion and concurrent adiabatic

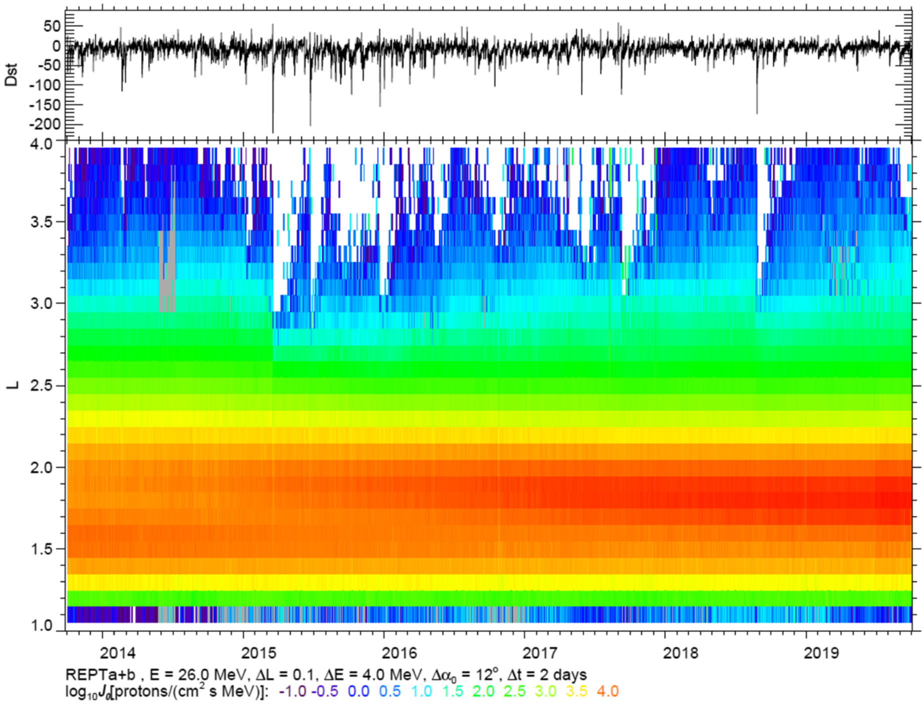

Fig. 51 Measured 2-day average equatorial differential omnidirectional intensity versus L and time from a combination of REPT-A and REPT-B PHA data (updated from Selesnick et al. (2014)). Intensity color coding and full bin widths are listed below. Geomagnetic Dst index versus time is shown above

heating during which the first two adiabatic invariants are conserved (Selesnick et al. 2016). The observed rate of change determines the required time-dependent diffusion coefficient in this region (Selesnick and Albert 2019). The source driving the inward diffusion is presumed to be a reservoir of solar protons that were trapped in the radiation belt at higher L and lower energy prior to the launch of Van Allen Probes.

In the $L < 1.6$ region, the lower energy proton intensity steadily decreased throughout the data interval, in contrast to the increasing intensity observed at immediately higher L and relatively steady intensity at low L but higher energy. The main factors expected to influence any variability at low L are slow inward diffusion, the CRAND source strength, and steady energy loss due to atmospheric and plasma drag. Evidently these factors were in near balance at higher energies but energy loss outweighed CRAND and inward diffusion at lower energies, causing the observed steady decay. However, model predictions of expected decay rates, based on known atmospheric and plasma densities combined with observed trapped proton initial conditions, were too slow compared to observed decay rates, prompting the suggestion that there may be an additional, undetermined loss mechanism for trapped protons at low L (Selesnick and Albert 2019).

At higher L values, protons are rapidly lost during magnetic storms and may also become trapped during concurrent solar proton events. Detailed observation of these processes requires a shorter time scale than the 1-month averages of Fig. 50. Omnidirectional intensity of 26-MeV trapped protons is shown as a function of L and time, with 2-day resolution, in Fig. 51 (updated from Selesnick et al. (2014) and derived directly from PHA data without the smoothing required at higher and lower energy). In this format, the steadily increasing intensity near $L = 1.8$ and decreasing intensity near $L = 1.5$ are again apparent. At $L > 2.5$, rapid loss of the lower intensity protons is concurrent with magnetic storms, as shown by the Dst index above, reaching the lowest L values during the major storms of 2015 and 2018. Observed losses during the March 2015 storm were consistent with the effects of pitch angle scattering caused by increased magnetic field-line curvature resulting from the enhanced storm-time ring current, combined with radial transport from induced electric fields, as shown by test particle simulation (Engel et al. 2016). Observed post-storm recovery of trapped proton intensity appears consistent with the steady CRAND source, as expected.

8 Space Weather Utilization

It is important to remember that the RBSP mission was a key part of NASA's Living with a Star (LWS) program. As such, RBSP payloads generally, and REPT instruments specifically, were intended to reveal space weather and space climate aspects of the Earth's space environment (Baker et al. 2018). In a very real sense, RBSP was to be a pathfinder for how to monitor the radiation belts and thereby provide situational awareness of near-Earth threats to operational space assets. An objective assessment would have to conclude that RBSP (Van Allen Probes) did a good job with this programmatic assignment (Ukhorskiy et al. 2020).

The RBSP spacecraft were outfitted with space weather "beacon" capabilities to send low data rate information continuously to any receiver that might be capable of taking the data (Mauk et al. 2013). For the beacon data stream, a few REPT integral counting rate channels were chosen to characterize the radiation belt environment (Baker et al. 2013a). These single detector rates were expected to give a "quick and dirty" look at the radiation belt properties.

Figure 52 shows about one year's worth of data from REPT relevant to the space weather (SWx) beacon performance. The beacon period covered is 1 January 2013 to 1 December 2013. The top figure panel shows REPT-A beacon data at a low-time cadence from an integral count rate stream that was responsive to electrons with $E \gtrsim 2.0$ MeV and also to protons with $E \gtrsim 20$ MeV. Data were acquired through various of the partner ground stations around the world (Mauk et al. 2013) and were then captured by the RBSP operations center at JHU/APL. As can be seen, the data were somewhat spotty and fragmented due to limited ground tracking of the real-time signals. It is also clear that inner zone energetic protons were detected strongly by the integral channel. Nonetheless, the real-time beacon data showed many fascinating outer zone electron onset events and gave a very clear picture of radiation belt structure and temporal characteristics.

For comparison, the second panel of Fig. 52 shows fully processed REPT-A data for the same general period of time (December 2012 – December 2013) as the top panel. The REPT level 2 data for the $E = 2.3$ MeV differential channel are obviously much cleaner and more continuous in time. However, from a monitoring perspective, the beacon data did a very good job of faithfully indicating radiation belt properties. As seen by the lower two panels of Fig. 52, the real-time REPT data (top panel) correspond closely to storm-time variations of Dst (third panel) and Kp (bottom panel). These results showed quite convincingly that a simple real-time monitor in an RBSP-like orbit could provide excellent situational awareness.

Because of the beacon data success, the real-time monitoring capability of REPT was used to support other NASA missions. For example, in October 2013 the Juno mission that

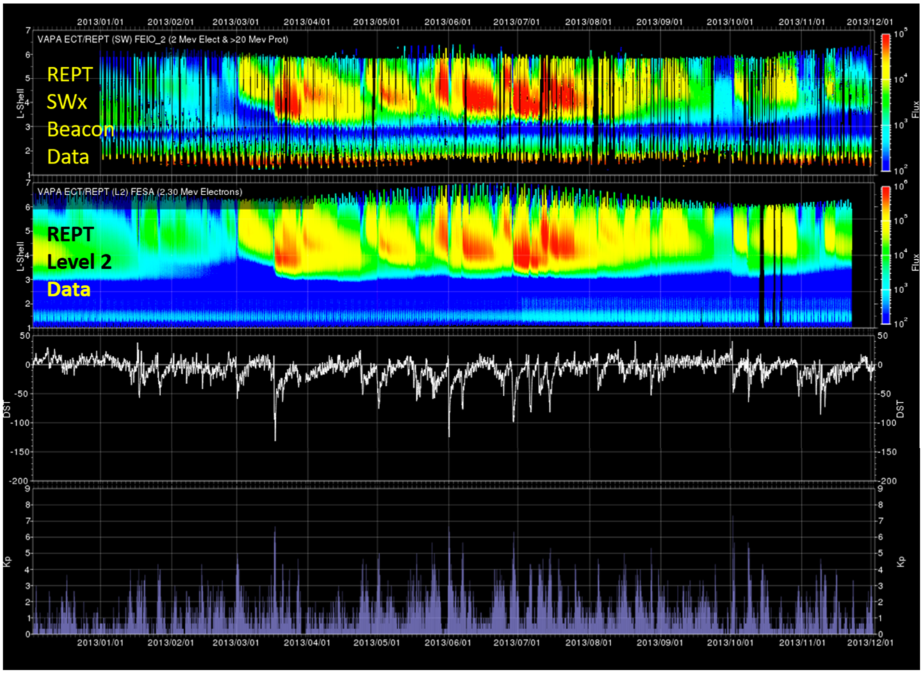

Fig. 52 Top panel: REPT real-time space weather "beacon" data in the L vs. time format for much of the year 2013. Second panel: The fully processed REPT Level-2 data for the same period as the upper panel. Lower two panels: The Dst and Kp indices, respectively, for this period. The real-time space weather beacon data give a clear picture of the radiation belt structure and time variations

was headed to Jupiter flew close by Earth for a gravitational assist "boost". The REPT real-time beacon data were employed in order to "cross-calibrate" Juno energetic electron sensors with those on RBSP – and to alert Juno operators about the space environment they would encounter during the Earth flyby. Figure 53 shows REPT-A 2 MeV, 5 MeV, and 10 MeV integral electron channels for the broad time period 11 September 2013 through 10 October 2013 (left side of figure). The Dst index is also shown at the bottom left. Interestingly, a pair of small geomagnetic storms occurred on 2 October and on 9 October. The right side of Fig. 53 shows color-coded fluxes along the RBSP-A orbit track for the REPT-A 5 MeV channel. The Juno track up to closest Earth approach on 9 October is also projected on the $(X\text{-}Y)_{\mathrm{GSE}}$ plane. Obviously, Juno flew through a fairly intense radiation belt environment on 9 October and good cross-correlating measurements were obtained from the real-time information (R. Thorne, priv. comm, 2013). The final processed REPT data for this period were used to compare with the Juno flyby data as well (however, to our knowledge these detailed results were never published).

The RBSP data, with an emphasis on REPT measurements, have been used for many other space weather and operational purposes. For example, Baker et al. (2019b) performed an extensive comparison analysis of GOES-15 data (from NOAA) with corresponding REPT-A data from RBSP. In this study, daily averages of GOES-15 electron fluxes were compared with related daily averages from REPT-A. Data for a six-year period were statistically compared. An example is shown here in Fig. 54. For this figure, RBSP-A data at $L = 6.0$ were compared with comparable energy ranges from the GOES-15 spacecraft (nominally at $L = 6.6$). The upper panel of Fig. 54 uses electron data from the MagEIS

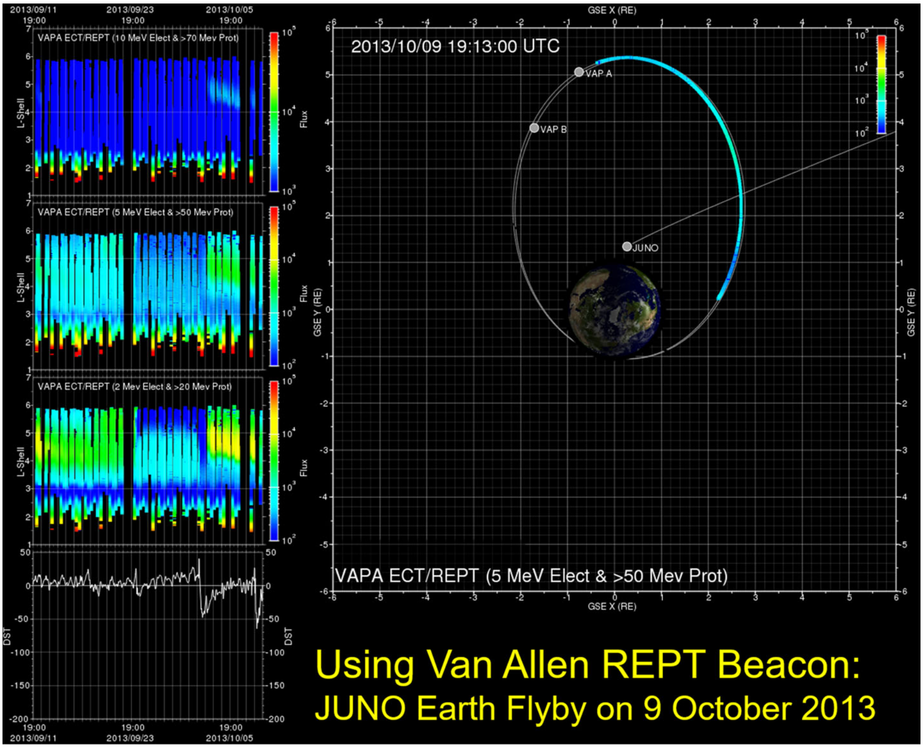

Fig. 53 Real-time REPT space-weather beacon data in several energy ranges ($E > 2$ MeV, >5 MeV, and $E > 10$ MeV) for a selected period in September and October 2013. As described in the text, the data were compared with measurements from the Juno spacecraft that flew by Earth on 9 October 2013

instrument on RBSP-A (0.8–4.0 MeV) and the lower panel uses $E > 2.0$ MeV electron data from REPT on RBSP-A.

The rather exhaustive statistical comparison of GOES and RBSP (Baker et al. 2019b) shows that the GOES spacecraft only rarely are at the nominal $L = 6.6$ location. Rather, because of local time dependencies and due to geomagnetic activity-dependent radial flux gradient effects, the GOES daily flux values are often factors of 10 to 100 lower than the corresponding RBSP measurements at true $L = 6.0$ locations. Thus, Baker et al. (2019b) concluded that space weather users must be very cautious in using GOES daily flux averages as a strict surrogate for outer radiation belt electron properties. GOES data can be used as a space weather "monitor" for regions $L \gtrsim 5.5$, but only with care.

9 Future Steps and Directions

While many aspects and dimensions of radiation belt science have been examined with the Van Allen Probes mission, it is clear that much more can – and should – be done. For the REPT domains of relativistic (and ultra-relativistic) electrons and for very energetic protons, much more extensive analyses could be performed than has been possible during the active data phase of VAP. Some specific event intervals, especially in the later mission years (2018–2019), have been only briefly examined. As described in this review, using the

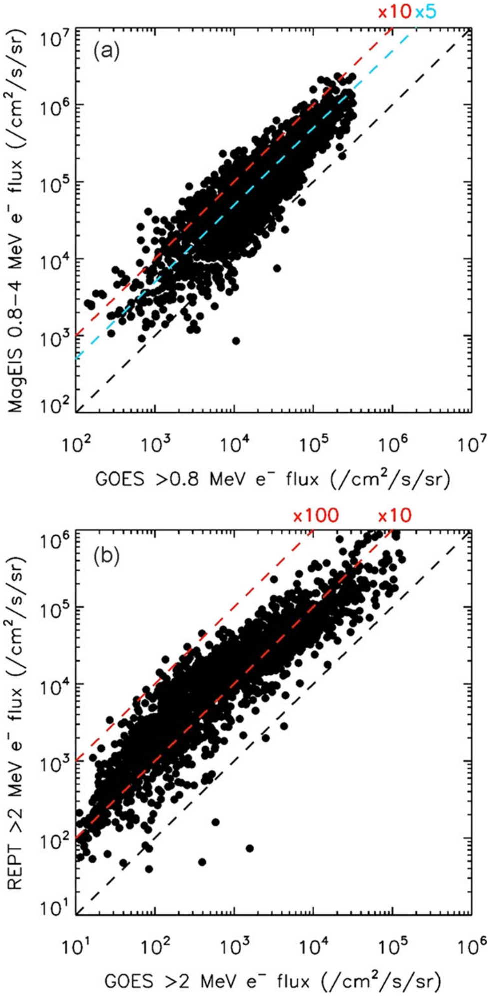

Fig. 54 Scatterplots of daily flux averages from the Van Allen Probes at $L = 6$ versus the GOES-15 "E" sensor. (**a**) Daily values of $E > 0.8$ MeV electrons from Van Allen Probes A versus comparable GOES-15 measurements. (**b**) Similar to (a) but for electrons with energies $E > 2$ MeV. Data from 1 September 2012 to 1 September 2018 are included in the plots

full instrument capabilities of REPT – as exemplified by the proton pulse-height analysis (PHA) capability – can reveal exquisite detail about spectral properties of both electron and proton populations. Using such PHA data also can allow much more highly resolved energy channel information. We can envision going from ∽20% (ΔE/E) resolution for electron spectral bands to ∽5% ($\Delta E/E$). The insights into acceleration and loss processes from such analysis could be profound.

There are other particle phenomena that probably are hidden in the REPT data streams. For example, we believe that for (certain times and under certain circumstances, the REPT telescopes should have been detecting not only protons but also very energetic alpha particles. Careful examination of rate information, along with PHA analysis, could allow examination of trapped helium nuclei or even heavier (CNO) ion species in the inner part of the magnetosphere. We are very eager to explore such possible hidden treasures. It is even possible, in principle, that REPT could have some light to shed on very energetic positrons in Earth's vicinity.

We strongly encourage scientists outside the REPT team to explore and evaluate the trove of particle data that has been acquired. Especially, a new generation of researchers may have novel ideas on what to look for beneath the surface of the data set. Certainly, the long run of high-quality data should be used to further improve models of the near-Earth space radiation environment (Baker et al. 2018). The REPT data are ripe for such applications.

We also note that the approach used by REPT for measuring energetic electrons has inspired and produced instruments like REPTile on CSSWE and MERiT (Miniaturized electron and pRoton Telescope, Kanekal et al. 2019), on CeREs (Compact Radiation belt Explorer), and the CUSP (Cubesat for study of Solar Protons). These miniaturized versions of REPT flown on CubeSats enable, for example, multipoint measurements of radiation belt electrons due to the reduced cost of CubeSat missions.

As a final point, the RBSP program has shown the high value of not only scientific but also operational benefits of having continuous, high-quality radiation belt measurements in a geostationary transfer orbit (GTO) type of configuration. While measurements in low-Earth orbit (like SAMPEX; see Baker et al. 1993, 2012) are immensely useful, they are no substitute for continuous, near-equatorial radiation belt monitoring. Although it is well known that radiation belt electron dynamics show a “global coherence” (Kanekal et al. 2001) so that LEO measurements can provide a window into the entirety of outer zone, that is limited to processes occurring over multiple drift time scales. Dynamics confined to the equatorial plane such as ultra-relativistic electron injection during the “hallow’een” 2003 event (Looper et al. 2005; Kress et al. 2007) propagate to LEO after time delays that can extend to months ($\sim$4 months during October-November 2003). Furthermore the sampling of a broader range of pitch angles at GTO (as compared to LEO) can be of critical importance in understanding of the role of wave-particle interactions, as demonstrated by, for example, Fennell et al. (2014) recently. As was also reviewed here (see Sect. 8) geostationary orbit monitors are very important for space weather operations, but they are no match for RBSP sorts of data. We implore – both for science and for operational reasons – that the agencies (civil and national security) do everything possible to emplace spacecraft in GTO that replicate a significant fraction of the RBSP detection capability. For the purposes of this review, we especially urge that relativistic electron and high-energy proton sensors be a central part of any such payloads.

10 Summary & Conclusions

This review began by remarking upon the original expressed goals for the Relativistic Electron-Proton Telescope investigations of the RBSP mission. As described here, the REPT instruments performed all their planned and assigned functions in an exemplary fashion. Both REPT-A and REPT-B operated flawlessly and continuously from 2 days after RBSP launch until each RBSP spacecraft was decommissioned and turned off. The REPT data proved to be of high quality both for scientific and for operational purposes.

The initial portions of this paper reminded readers of the REPT design and functional qualities. Many of the aspirations described in the original REPT paper (Baker et al. 2013a) have been fully achieved and validated through long years of on-orbit operation in a quite hostile space environment. For the scientific and the engineering data user of REPT results, we provided in this paper a summary of sensor operational trends and the (minor) mode changes that occurred during the mission operational phase. We also reviewed for users of the data sets the known sensor backgrounds and our presently understood correction approaches.

A substantial part of this review has been devoted to touching on highlights of the scientific results from the REPT instruments. Owing to the REPT wide energy range, excellent energy resolution, dynamic sensitivity range, and the data uniformity and continuity, many new and exciting features of radiation belt properties were uncovered. Aspects of radiation belt morphology, timing, and underlying physical causation were all made possible by having the "new" REPT eyes onboard the dual RBSP spacecraft.

As noted previously in this review, the RBSP mission had the stated and explicit goal to learn more about the near-Earth space radiation environment. The longer-term objective of this RBSP program was to deepen our physical understanding and to thereby improve our specification and forecast models of the Van Allen radiation belts. We believe that this goal was met admirably by the RBSP program. We further believe that REPT played an essential role in achieving these stated objectives.

Acknowledgements The Relativistic Electron-Proton Telescope (REPT) program involved a large, active team of skilled individuals. At the Laboratory for Atmospheric and Space Physics (LASP), Mary Bolton served admirably as Program Manager for the entire mission. Susan Batiste was the Systems Engineer prior to her retirement from LASP. Coauthor V. Hoxie was the lead electronics engineer. Supporting him in key roles were Mark Kien, Stacy Wade, Chris Belting, Karl Hubbell, Ken Stevens, Magnus Karlsson, and Beth Cervelli. Alan Yehle was the lead mechanical engineer. Bret Lamprecht was the thermal engineer. Early in the project and architecture phase, Jim Westfall was the lead engineer and architect. Ginger Drake led the detector design and development effort with Micron Semiconductor in the United Kingdom. Steve Steg provided the mechanical design for the electronics box and the challenging REPT telescope design.

The following people presently at LASP were effective and engaged members of the design, development, and testing phases of the REPT instruments: D. Bausch, S. Bramer, P. Bay, M. Bonnici, J. Brown, L. Buckhannon, J. Craft, S. Doumont, N.J. Farber, D. Farneth, B. French, S. Gurst, K. Gutierrez, J. Herring, K.F. Heuerman, A. Hoskins, L.L. Jilek, D. Judd, S. Knappmiller, E. Knehans, C. Krug, G. Lafferty, A. May, J. Methlie, S. Monk, B. Motz, G. Otzinger, C. Pankratz, N. Perish, K. Pilewskie, M. Rider, P. Sicken, R. Sood, J. Sprunck, Z. Sternovsky, G.A. Tate, T. Taylor, S.A. Tucker, G. Ucker, S. Van Dyk, T. Vincent, D. Vincent, N. White, H. Withnell, J.S. Young. The science operations team at Los Alamos National Lab (M. Henderson, R. Friedel, G. Reeves) is also thanked for its support.

The REPT science team gratefully acknowledges the helpful advice of senior colleagues as the REPT design effort was under way. These include R. Mewaldt, E. Stone, G. Ginet, J. Fennell, and B. Klecker, and the late F. B. McDonald. Two colleagues who passed away during the Van Allen Probes mission deserve special mention. Theodore Fritz (Boston U.) and Richard Thorne (UCLA) were outstanding source of knowledge and insight for the team.

The REPT program was supported by NASA Prime Contract No. NNN06AA01C from the Johns Hopkins Applied Physics Lab thru University of New Hampshire, subcontract #17-003.

References

A.F. Ali, S.R. Elkington, W. Tu, L.G. Ozeke, A.A. Chan, R.H.W. Friedel, Magnetic field power spectra and radial diffusion coefficients using CRRES magnetometer data. J. Geophys. Res. **120**, 973 (2015). https://doi.org/10.1029/2014JA020419

A.F. Ali, D.M. Malaspina, S.R. Elkington, A.N. Jaynes, A.A. Chan, J. Wygant, C.A. Kletzing, Electric and magnetic radial diffusion coefficients using the Van Allen probes data. J. Geophys. Res. Space Phys. **121**, 10 (2016). https://doi.org/10.1002/2016JA023002

N.A. Aseev, Y.Y. Shprits, D. Wang, J. Wygant, A.Y. Drozdov, A.C. Kellerman, G.D. Reeves, Transport and loss of ring current electrons inside geosynchronous orbit during the 17 March 2013 storm. J. Geophys. Res. Space Phys. **124**, 2 (2019). https://doi.org/10.1029/2018ja026031

D.N. Baker, Coupling between the solar wind, magnetosphere, ionosphere, and neutral atmosphere, in *Encyclopedia of Astronomy and Astrophysics*, ed. by P. Murdin (Institute of Physics Publishing, Bristol, 2001), pp. 2911–2914

D.N. Baker, New twists in Earth's radiation belts. Am. Sci. **102**(5), 374–381 (2014)

D.N. Baker, P.R. Higbie, R.D. Belian, E.W. Hones Jr., Do Jovian electrons influence the terrestrial outer radiation zone? Geophys. Res. Lett. **6**, 531–534 (1979). https://doi.org/10.1029/GL006i006p00531

D.N. Baker, J.B. Blake, D.J. Gorney, P.R. Higbie, R.W. Klebesadel, J.H. King, Highly relativistic magnetospheric electrons: a role in coupling to the middle atmosphere? Geophys. Res. Lett. **14**, 1027 (1987)

D.N. Baker, G.M. Mason, O. Figueroa, G. Colon, J. Watzin, R. Aleman, An overview of the SAMPEX mission. IEEE Trans. Geosci. Remote Sens. **31**, 531 (1993)

D.N. Baker, C.A. Barth, K.E. Mankoff, S.G. Kanekal, S.M. Bailey, G.M. Mason, J.E. Mazur, Relationships between precipitating auroral zone electrons and lower thermospheric nitric oxide densities: 1998–2000. J. Geophys. Res. **106**(A11), 24,465–24,480 (2001). https://doi.org/10.1029/2001JA000078

D.N. Baker, S.G. Kanekal, X. Li, S.P. Monk, J. Goldstein, J.L. Burch, An extreme distortion of the Van Allen belt arising from the "Hallowe'en" solar storm in 2003. Nature **432**, 878 (2004). https://doi.org/10.1038/nature03116

D.N. Baker, J.E. Mazur, G. Mason, SAMPEX to reenter atmosphere: twenty-year mission will end. Space Weather **10**, SO5006 (2012). https://doi.org/10.1029/2012SW000804

D.N. Baker, S.G. Kanekal, V.C. Hoxie et al., The Relativistic Electron-Proton Telescope (REPT) instrument on board the Radiation Belt Storm Probes (RBSP) spacecraft: characterization of Earth's radiation belt high-energy particle populations. Space Sci. Rev. **179**, 337–381 (2013a). https://doi.org/10.1007/s11214-012-9950-9

D.N. Baker, S.G. Kanekal, V.C. Hoxie, M.G. Henderson, X. Li, H.E. Spence, S.R. Elkington, R.H. Friedel, J. Goldstein, M.K. Hudson, G.D. Reeves, R.M. Thorne, C.A. Kletzing, S.G. Claudepierre, A long-lived relativistic electron storage ring embedded in the Earth's outer Van Allen radiation zone. Science **340**(6129), 186–190 (2013b). https://doi.org/10.1126/science.1233518

D.N. Baker, V. Hoxie, A. Jaynes, A. Kale, S.G. Kanekal, X. Li, G. Reeves, H.E. Spence, James Van Allen and his namesake NASA mission. Eos **94**(49), 469–470 (2013c)

D.N. Baker, A.N. Jaynes, X. Li, M.G. Henderson, S.G. Kanekal, G.D. Reeves, H.E. Spence, S.G. Claudepierre, J.F. Fennell, M.K. Hudson, R.M. Thorne, J.C. Foster, P.J. Erickson, D.M. Malaspina, J.R. Wygant, A. Boyd, C.A. Kletzing, A. Drozdov, Y.Y. Shprits, Gradual diffusion and punctuated phase space density enhancements of highly relativistic electrons: Van Allen Probes observations. Geophys. Res. Lett. **41**, 1351–1358 (2014a). https://doi.org/10.1002/2013GL058942

D.N. Baker, A.N. Jaynes, V.C. Hoxie, R.M. Thorne, J.C. Foster, X. Li, J.F. Fennell, J.R. Wygant, S.G. Kanekal, P.J. Erickson, W. Kurth, W. Li, Q. Ma, Q. Schiller, L. Blum, D.M. Malaspina, A. Gerrard, L.J. Lanzerotti, An impenetrable barrier to ultra-relativistic electrons in the Van Allen radiation belt. Nature **515**, 531–534 (2014b). https://doi.org/10.1038/nature13956

D.N. Baker, A.N. Jaynes, S.G. Kanekal, J.C. Foster, P.J. Erickson, J.F. Fennell, J.B. Blake, H. Zhao, X. Li, S.R. Elkington, M.G. Henderson, G.D. Reeves, H.E. Spence, C.A. Kletzing, J.R. Wygant, Highly relativistic radiation belt electron acceleration, transport, and loss: large solar storm events of March and June 2015. J. Geophys. Res. Space Phys. **121**, 6647–6660 (2016a). https://doi.org/10.1002/2016JA022502

D.N. Baker, A.N. Jaynes, D.L. Turner, R. Nakamura, D. Schmid, B. Mauk, I. Cohen, J.F. Fen-nell, J.B. Blake, R.J. Strangeway, C.T. Russell, R.B. Torbert, J.C. Dorelli, D.J. Gershman, B.L. Giles, J.L. Burch, A telescopic and microscopic examination of acceleration in the June 2015 geomagnetic storm: magnetospheric MultiScale and Van Allen Probes study of substorm particle injection. Geophys. Res. Lett. **43**(12), 6051–6059 (2016b). https://doi.org/10.1002/2016GL069643

D.N. Baker, P.J. Erickson, J.F. Fennell et al., Space weather effects in the Earth's radiation belts. Space Sci. Rev. **214**, 17 (2018). https://doi.org/10.1007/s11214-017-0452-7

D.N. Baker, V. Hoxie, H. Zhao, A.N. Jaynes, S. Kanekal, X. Li, S. Elkington, Multi-year measurements of radiation belt electrons: acceleration, transport, and loss. J. Geophys. Res. Space Phys. **124**, 2588–2602 (2019a). https://doi.org/10.1029/2018JA026259

D.N. Baker, H. Zhao, X. Li, S.G. Kanekal, A.N. Jaynes, B.T. Kress et al., Comparison of Van Allen Probes energetic electron data with corresponding GOES-15 measurements: 2012–2018. J. Geophys. Res. Space Phys. **124**, 9924–9942 (2019b). https://doi.org/10.1029/2019JA027331

C.A. Barth, W.K. Tobiska, D.E. Siskind, D.D. Cleary, Solarterrestrial coupling: low-latitude thermospheric nitric oxide. Geophys. Res. Lett. **15**(1), 92–94 (1988)

C.A. Barth, K.D. Mankoff, S.M. Bailey, S.C. Solomon, Global observations of nitric oxide in the thermosphere. J. Geophys. Res. Space Phys. **108**(A1), 1027 (2003). https://doi.org/10.1029/2002JA009458

L. Bingley, V. Angelopoulos, D. Sibeck, X. Zhang, A. Halford, The evolution of a pitch-angle "bite-out" scattering signature caused by EMIC wave activity: a case study. J. Geophys. Res. Space Phys. **124**, 5042–5055 (2019). https://doi.org/10.1029/2018JA026292

J.B. Blake, W.A. Kolasinski, R.W. Fillius, E.G. Mullen, Injection of electrons and protons with energies of tens of MeV into $L < 3$ on 24 March 1991. Geophys. Res. Lett. **19**(8), 821–824 (1992). https://doi.org/10.1029/92GL00624

J.B. Blake et al., The Magnetic Electron Ion Spectrometer (MagEIS) instruments aboard the Radiation Belt Storm Probes (RBSP) spacecraft. Space Sci. Rev. (2013). https://doi.org/10.1007/s11214-013-9991-8

P. Blasi, The origin of galactic cosmic rays. Astron. Astrophys. Rev. **21**, 70 (2013). https://doi.org/10.1007/s00159-013-0070-7. (Review article)

A.J. Boyd, G.D. Reeves, H.E. Spence, H.O. Funsten, B.A. Larsen, R.M. Skoug et al., RBSP-ECT combined spin-averaged electron flux data product. J. Geophys. Res. Space Phys. **124**, 9124–9136 (2019). https://doi.org/10.1029/2019JA026733

D.H. Brautigam, J.M. Albert, Radial diffusion analysis of outer radiation belt electrons during the October 9, 1990 magnetic storm. J. Geophys. Res. **105**(A1), 291 (2000). https://doi.org/10.1029/1999JA900344

Breneman et al., title – TBD (2020), this volume

M. Bruff, A.N. Jaynes, H. Zhao, J. Goldstein, D.M. Malaspina, D.N. Baker, S.G. Kanekal, H.E. Spence, G.D. Reeves, The role of the dynamic plasmapause in outer radiation belt electron flux enhancement. Geophys. Res. Lett. **47**, e2020GL086991 (2020). https://doi.org/10.1029/202GL086991

C.C. Chaston, J.W. Bonnell, J.R. Wygant, G.D. Reeves, D.N. Baker, D. Melrose, I. Carins, Radial transport of radiation belt electrons in kinetic field-line resonances. Geophys. Res. Lett. **44**, 16 (2017). https://doi.org/10.1002/2017gl074587

M.W. Chen, M. Schulz, L.R. Lyons, D.J. Gorney, Ion radial diffusion in an electrostatic impulse model for stormtime ring current formation. Geophys. Res. Lett. **19**, 621 (1992). https://doi.org/10.1029/92GL00392

S.G. Claudepierre, F.R. Toffoletto, M. Wiltberger, Global MHD modeling of resonant ULF waves: simulations with and without a plasmasphere. J. Geophys. Res. **121**, 1 (2016). https://doi.org/10.1002/2015JA022048

S.G. Claudepierre, T.P. O'Brien, J.F. Fennell, J.B. Blake, J.H. Clemmons, M.D. Looper, J.E. Mazur, J.L. Roeder, D.L. Turner, The hidden dynamics of relativistic electrons (0.7-1.5 MeV) in the inner zone and slot region. J. Geophys. Res. Space Phys. **122**, 3 (2017). https://doi.org/10.1002/2016ja023719

Claudepierre, J.B. Blake, A.J. Boyd, J.H. Clemmons, J.F. Fennell, C. Gabrielse, M.D. Looper, J.E. Mzaur, T.P. O'Brien, G.D. Reeves, L. Roeder, H.E. Spence, D.L. Turner, The Magnetic Electron Ion Spectrometer: a review of on-orbit sensor performance, data, operations, and science. *Space Sci. Rev.* (2020), this volume

J.M. Cornwall, Diffusion processes influenced by conjugate-point wave phenomena. Radio Sci. **3**(7), 740 (1968)

G.S. Cunningham, Radial diffusion of radiation belt particles in nondipolar magnetic fields. J. Geophys. Res. Space Phys. **121**, 6 (2016). https://doi.org/10.1002/2015ja021981

L. Dai, J.R. Wygant, C.A. Cattell, S. Thaller, K. Kersten, A. Breneman, X. Tang, R.H. Friedel, S.G. Claudepierre, X. Tao, Evidence for injection of relativistic electrons into the Earth's outer radiation belt via intense substorm electric fields. Geophys. Res. Lett. **41**, 1133–1141 (2014). https://doi.org/10.1002/2014GL059228

L. Dai, C. Wang, S. Duan, Z. He, J.R. Wygant, J.W. Bonnell, C.A. Cattell, C.A. Kletzing, D.N. Baker, X. Li, D.M. Malaspina, J.B. Blake, J.F. Fennell, S.G. Claudepierre, K. Takahashi, H.O. Funsten, G.D. Reeves, H.E. Spence, V. Angelopoulos, K.-H. Glassmeier, X. Tao, L. Chen, D.L. Turner, S.A. Thaller, A.W. Breneman, X. Tang, The near-Earth injection of MeV electrons associated with intense dipolarization electric fields: Van Allen Probes observations. Geophys. Res. Lett. **42**(15), 3170–6179 (2015a). https://doi.org/10.1002/2015GL064483

L. Dai et al., Near-Earth injection of MeV electrons associated with intense dipolarization electric fields: Van Allen Probes observations. Geophys. Res. Lett. **42**, 6170–6179 (2015b). https://doi.org/10.1002/2015GL064955

E.J. Daly, P. Buhler, M. Kruglanski, Observations of the outer radiation belt with REM and comparisons with models. IEEE Trans. Nucl. Sci. **46**(6), 1469–1474 (1999). https://doi.org/10.1109/23.819109

L. Desorgher, P. Buhler, A. Zehnder, E.O. Fluckiger, Simulations of the outer radiation belt electron flux decrease during the March 26, 1995, magnetic storm. J. Geophys. Res. **105**(A9), 21 211 (2000)

A.V. Dmitriev, A.V. Suvorova, J.-K. Chao, C.B. Wang, L. Rastaetter, M.I. Panasyuk, L.L. Lazutin, A.S. Kovtyukh, I.S. Veselovsky, I.N. Myagkova, Anomalous dynamics of the extremely compressed magnetosphere during 21 January 2005 magnetic storm. J. Geophys. Res. Space Phys. **119**, 877–896 (2014). https://doi.org/10.1002/2013JA019534

A.Y. Drozdov, Y.Y. Shprits, N.A. Aseev, A.C. Kellerman, G.D. Reeves, Dependence of radiation belt simulations to assumed radial diffusion rates tested for two empirical models of radial transport. Space Weather **15**, 1 (2017). https://doi.org/10.1002/2016SW001426

S.R. Elkington, M.K. Hudson, A.A. Chan, Acceleration of relativistic electrons via drift-resonant interaction with toroidal-mod Pc-5 ULF oscillations. Geophys. Res. Lett. **26**, 3273 (1999). https://doi.org/10.1029/1999GL003659

S.R. Elkington, M.K. Hudson, A.A. Chan, Resonant acceleration and diffusion of outer zone electrons in an asymmetric geomagnetic field. J. Geophys. Res. **108**, 1116 (2003). https://doi.org/10.1029/2003JA010368

S.R. Elkington, D.N. Baker, M. Wiltberger, Injection of energetic ions during the 31 March 0630 substorm, in *The Inner Magnetosphere: Physics and Modeling*, ed. by T.I. Pulkkinen, N.A. Tsyganenko, R.H.W. Friedel. Geophysical Monographs, vol. 155 (American Geophysical Union, Washington, D.C., 2005), p. 147. https://doi.org/10.1029/155GM17

M.J. Engebretson, J.L. Posch, A.M. Westerman, N.J. Otto, J.A. Slavin, G. Le, R.J. Strangeway, M.R. Lessard, Temporal and spatial characteristics of Pc1 waves observed by ST5. J. Geophys. Res. **113** (2008). https://doi.org/10.1029/2008JA013145

M.A. Engel, B.T. Kress, M.K. Hudson, R.S. Selesnick, Comparison of Van Allen Probes radiation belt proton data with test particle simulation for the 17 March 2015 storm. J. Geophys. Res. Space Phys. **121**, 11,035–11,041 (2016). https://doi.org/10.1002/2016JA023333

C.-G. Falthammar, Coefficients of diffusion in the outer radiation belts, in *Radiation Trapped in the Earth's Magnetic Field*, ed. by B.M. McCormac. NATO Advanced Study Institute (Reinhold Book Corp., New York, 1966), p. 398. https://doi.org/10.1007/978-94-010-3553-8_30

C.-G. Falthammar, Radial diffusion by violation of the third adiabatic invariant, in *Earth's Particles and Fields*, ed. by B.M. McCormac. NATO Advanced Study Institute (Reinhold Book Corp., New York, 1968), p. 157

Y. Fei, A.A. Chan, S.R. Elkington, M.J. Wiltberger, Radial diffusion simulation of relativistic electron transport by ULF waves in the September 1998 storm. J. Geophys. Res. **111**, A12209 (2006). https://doi.org/10.1029/2005JA011211

J.F. Fennell et al., Van Allen Probes observations of direct wave-particle interactions. Geophys. Res. Lett. **41**, 1869–1875 (2014). https://doi.org/10.1002/2013GL059165

J.F. Fennell, D.N. Baker et al., Van Allen Probes show that the inner radiation zone contains no MeV electrons: ECT/MagEIS data. Geophys. Res. Lett. **42**(5), 1283 (2015)

J. Fennell, D.N. Baker et al., Current energetic particle sensors. J. Geophys. Res. Space Phys. **121**(9), 8840–8858 (2016)

R. Filwett, Private comm. (2020)

C. Forsyth, J.I. Rae, K.R. Murphy, C.-L. Huang, A.J. Boyd, J.C. Coxon, M.P. Freeman, M.C. Jackman, M.E. Kalmoni, D.G. Sibeck, H.E. Spence, What effect do substorms have on the content of the radiation belts? J. Geophys. Res. Space Phys. **121**, 7 (2016). https://doi.org/10.1002/2016ja022620

J.C. Foster, P.J. Erickson, D.N. Baker, S.G. Claudepierre, C.A. Kletzing, W. Kurth, G.D. Reeves, S.A. Thaller, H.E. Spence, Y.Y. Shprits, J.R. Wygant, Prompt energization of relativistic and highly relativistic electrons during a substorm interval: Van Allen Probes observations. Geophys. Res. Lett. **41**, 20–25 (2014). https://doi.org/10.1002/2013gl058438

J.C. Foster, J.R. Wygant, M.K. Hudson, A.J. Boyd, D.N. Baker, P.J. Erickson, H.E. Spence, Shock-induced prompt relativistic electron acceleration in the inner magnetosphere. J. Geophys. Res. Space Phys. **120**(3), 1651–1674 (2015). https://doi.org/10.1002/2014ja020642

J.C. Foster, P.J. Erickson, D.N. Baker, A.N. Jaynes, E.V. Mishin, J.F. Fennel, X. Li, M.G. Henderson, S.G. Kanekal, Observations of the impenetrable barrier, the plasmapause, and the VLF bubble during the 17 March 2015 storm. J. Geophys. Res. Space Phys. **121**, 5537–5548 (2016). https://doi.org/10.1002/2016JA022509

J.C. Foster, P.J. Erickson, Y. Omura, D.N. Baker, C.A. Kletzing, S.G. Claudepierre, Van Allen Probes observations of prompt MeV radiation belt electron acceleration in non-linear interactions with VLF chorus. J. Geophys. Res. Space Phys. **122**(1), 324–339 (2017). https://doi.org/10.1002/2016JA023429

J.C. Foster, P.J. Erickson, Y. Omura, D.N. Baker, The impenetrable barrier: suppression of chorus wave growth by VLF transmitters. J. Geophys. Res. Space Phys. **125**, e2020JA027913 (2020). https://doi.org/10.1029/2020JA027913

Gkioulidou et al., title – TBD (2020), this volume

M. Gkioulidou, S. Ohtani, D.G. Mitchell, A.Y. Ukhorskiy, G.D. Reeves, D.L. Turner, J.W. Gjerloev, M. Nose, K. Koga, J.V. Rodriguez, L.J. Lanzerotti, Spatial structure and temporal evolution of energetic particle injections in the inner magnetosphere during the 14 July 2013 substorm event. J. Geophys. Res. Space Phys. **120**, 3 (2014). https://doi.org/10.1002/2014ja020872

J. Goldstein, M.K. Hudson, W. Lotko, Possible evidence of damped cavity mode oscillations stimulation by the January 1997 magnetic cloud event. Geophys. Res. Lett. **26**, 3589 (1999). https://doi.org/10.1029/1999GL003636

J. Goldstein, S.G. Kanekal, D.N. Baker, B.R. Sandel, Dynamic relationship between the outer radiation belt and the plasmapause during March–May 2001. Geophys. Res. Lett. **32**, L15104 (2005). https://doi.org/10.1029/2005GL023431

J. Goldstein et al., Simulation of Van Allen Probes' plasmapause encounters. J. Geophys. Res. **119**, 7464 (2014). https://doi.org/10.1002/2014JA020252

J. Goldstein et al., The relationship between the plasmapause and outer belt electrons. J. Geophys. Res. **121**, 9 (2016). https://doi.org/10.1002/2016ja023046

J. Goldstein, P.W. Valek, D.J. McComas, J. Redfern, H.E. Spence, R.M. Skoug, B.A. Larsen, G.D. Reeves, R. Nakamura, Global ENA imaging and in situ observations of substorm dipolarization on 10 August 2016. J. Geophys. Res. Space Phys. **125**(4), e2019JA027733 (2020). https://doi.org/10.1029/2019JA027733.

A.D. Greeley, S.G. Kanekal, D.N. Baker, B. Klecker, Q. Schiller, Quantifying the contribution of microbursts to global electron loss in the radiation belts. J. Geophys. Res. Space Phys. **124**(2), 1111–1124 (2019). https://doi.org/10.1029/2018JA026368

X. Gu et al., Dynamic responses of radiation belt electron fluxes to magnetic storms and their correlations with magnetospheric plasma wave activities. Astrophys. J. **891**, 127 (2020)

Y. Hao, Q.-G. Zong, Y. Wang, X.-Z. Zhou, H. Zhang, S. Fu, Z.Y. Pu, H.E. Spence, J.B. Blake, J. Bonnell, J. Wygant, C. Kletzing, Interactions of energetic electrons with ULF waves triggered by interplanetary shock: Van Allen Probes observations in the magnetotail. J. Geophys. Res. **119**, 8262–8273 (2014). https://doi.org/10.1002/2014JA020023

Y.X. Hao, Q.G. Zong, X.Z. Zhou, S.Y. Fu, R. Rankin, C.J. Yuan, A.T.Y. Lui, H.E. Spence, J.B. Blake, D.N. Baker, G.D. Reeves, Electron dropout echoes induced by interplanetary shock: Van Allen Probes observations. Geophys. Res. Lett. **43**, 11 (2016). https://doi.org/10.1002/2016gl069140

Y.X. Hao, Q.G. Zong, X.Z. Zhou, R. Rankin, X.R. Chen, Y. Liu, S.Y. Fu, H.E. Spence, J.B. Blake, G.D. Reeves, Relativistic electron dynamics produced by azimuthally localized poloidal mode ULF waves: boomerang-shaped pitch angle evolutions. Geophys. Res. Lett. **44**, 15 (2017). https://doi.org/10.1002/2017gl074006

Y.X. Hao, Q.-G. Zong, X.-Z. Zhou, R. Rankin, X.R. Chen, Y. Liu, S.Y. Fu, D.N. Baker, H.E. Spence, J.B. Blake, G.D. Reeves, S.G. Claudepierre, Global scale ULF waves associated with SSC accelerate magnetospheric ultra-relativistic electrons. J. Geophys. Res. Space Phys. **124**, 3 (2019). https://doi.org/10.1029/2018ja026134

M.D. Hartinger, S.G. Claudepierre, D.L. Turner, G.D. Reeves, A.W. Breneman, I.R. Mann, T. Peek, E. Chang, J.B. Blake, J.F. Fennell, T.P. O'Brien, M.D. Looper, Diagnosis of ULF wave-particle interactions with MeV electrons: the importance of ultra-high resolution energy channels. Geophys. Res. Lett. **45**, 20 (2018). https://doi.org/10.1029/2018gl080291

W.N. Hess, E.H. Canfield, R.E. Lingenfelter, Cosmic-ray neutron demography. J. Geophys. Res. **66**(3), 665–677 (1961). https://doi.org/10.1029/JZ066i003p00665

R.B. Horne, R.M. Thorne, S.A. Glauert, J.M. Albert, N.P. Meredith, R.R. Anderson, Timescale for radiation belt electron acceleration by whistler mode chorus waves. J. Geophys. Res. **110**, A03225 (2005). https://doi.org/10.1029/2004JA010811

R.B. Horne, R.M. Thorne, S.A. Glauert, N.P. Meredith, D. Pokhotelov, O. Santolík, Electron acceleration in the Van Allen radiation belts by fast magnetosonic waves. Geophys. Res. Lett. **34**, L17107 (2007). https://doi.org/10.1029/2007GL030267

Y.-K. Hsieh, Y. Omura, Nonlinear damping of oblique whistler mode waves via Landau resonance. J. Geophys. Res. Space Phys. **123**, 7462–7472 (2018). https://doi.org/10.1029/2018JA025848

M. Hua, B. Ni, S. Fu, X. Gu, Z. Xiang, X. Cao, W. Zhang, Y. He, H. Huang, Y. Lou, Y. Zhang, Combined scattering of outer radiation belt electrons by simultaneously occurring chorus, exohiss and magnetosonic waves. Geophys. Res. Lett. **45**, 10057–10067 (2018). https://doi.org/10.1029/2018GL079533

M. Hua, B. Ni, H. Huang, D. Summers, S. Fu, Z. Xiang, X. Gu, X. Cao, Y. Lou, Evolution of radiation belt electron pitch angle distribution due to combined scattering by plasmaspheric hiss and magnetosonic waves. Geophys. Res. Lett. **46**, 3033–3042 (2019). https://doi.org/10.1029/2018GL081828

M.K. Hudson, S.R. Elkington, J.G. Lyon, V.A. Marchenko, I. Roth, M. Temerin, J.B. Blake, M.S. Gussenhoven, J. Wygant, Simulations of radiation belt formation during storm sudden commencements. J. Geophys. Res. **102**, 13087 (1997). https://doi.org/10.1029/97JA03995

M.K. Hudson, S.R. Elkington, J.G. Lyon, C.C. Goodrich, Increase in relativistic electron flux in the inner magnetosphere: ULF wave mode structure. Adv. Space Res. **25**, 2327 (2000). https://doi.org/10.1016/S0273-1177(99)00518-9

M.K. Hudson, D.N. Baker, J. Goldstein, B.T. Kress, J. Paral, F. Toffoletto, M. Wiltburger, Simulated magnetopause losses and Van Allen Probe flux dropouts. Geophys. Res. Lett. (2014). https://doi.org/10.1002/2014gl059222

M.K. Hudson, J. Paral, B.T. Kress, M. Wiltberger, D.N. Baker, J.C. Foster, D.L. Turner, J.R. Wygant, Modeling CME-shock driven storms in 2012–2013: MHD-test particle simulations. J. Geophys. Res. Space Phys. **120**(2), 1168–1181 (2015). https://doi.org/10.1002/2014ja020833

M. Hudson, A. Jaynes, B. Kress, Z. Li, M. Patel, X. Shen, S. Thaller, M. Wiltberger, J. Wygant, Simulated prompt acceleration of multi-MeV electrons by the 17 March 2015 interplanetary shock. J. Geophys. Res. Space Phys. **122**, 10 (2017). https://doi.org/10.1002/2017ja024445

R.H.A. Iles, A.N. Fazakerley, A.D. Johnstone, N.P. Meredith, P. Bühler, The relativistic electron response in the outer radiation belt during magnetic storms. Ann. Geophys. **20**(7), 957–965 (2002). https://doi.org/10.5194/angeo-20-957-2002

J.C. Ingraham, T.E. Cayton, R.D. Belian, R.A. Christensen, R.H.W. Friedel, M.M. Meier, G.D. Reeves, M. Tuszewski, Substorm injection of relativistic electrons to geosynchronous orbit during the great magnetic storm of March 24, 1991. J. Geophys. Res. **106**(A4), 25759 (2001). https://doi.org/10.1029/2000JA000458

J.A. Jacobs, Y. Kato, S. Matsushita, V.A. Troitskaya, Classification of geomagnetic micropulsations. J. Geophys. Res. **69**, 180 (1964). https://doi.org/10.1029/JZ069i001p00180

A.N. Jaynes, D.N. Baker, H.J. Singer, J.V. Rodriguez et al., Source and seed populations for relativistic electrons: their roles in radiation belt changes. J. Geophys. Res. Space Phys. **120**, 7240–7254 (2015). https://doi.org/10.1002/2015JA021234

A.N. Jaynes, A.F. Ali, S.R. Elkington, D.M. Malaspina, D.N. Baker, X. Li et al., Fast diffusion of ultra-relativistic electrons in the outer radiation belt: 17 March 2015 storm event. Geophys. Res. Lett. **45**, 10,874–10,882 (2018). https://doi.org/10.1029/2018GL079786

S.G. Kanekal, D.N. Baker, J.B. Blake, Multisatellite measurements of relativistic electrons: global coherence. J. Geophys. Res. Space Phys. **106**(A12), 29721–29732 (2001)

S.G. Kanekal et al., Prompt acceleration of magnetospheric electrons to ultrarelativistic energies by the 17 March 2015 interplanetary shock. J. Geophys. Res. Space Phys. **121**, 7622–7635 (2016). https://doi.org/10.1002/2016JA022596

S.G. Kanekal, L. Blum, E.R. Christian, G. Crum, M. Desai, J. Dumonthier, A. Evans, A.D. Greeley, S. Guerro, S. Livi, K. LLera, J. Lucas, J. MacKinnon, J. Mukherjee, K. Ogasawara, N. Paschalidis, D. Patel, E. Pollack, S. Riall, Q. Schiller, G. Suarez, E.J. Summerlin, The MERiT onboard the CeREs: a novel instrument to study energetic particles in the Earth's radiation belts. J. Geophys. Res. Space Phys. **124**, 5734–5760 (2019). https://doi.org/10.1029/2018JA026304

C. Katsavrias, I.A. Daglis, W. Li, On the statistics of acceleration and loss of relativistic electrons in the outer radiation belt: a superposed epoch analysis. J. Geophys. Res. Space Phys. **124**, 4 (2019). https://doi.org/10.1029/2019ja026569

L.Y. Khoo et al., On the initial enhancement of energetic electrons and the innermost plasmapause locations: coronal mass ejection-driven storm periods. J. Geophys. Res. **123**, 11 (2018). https://doi.org/10.1029/2018ja026074

L.Y. Khoo, X. Li, H. Zhao, X. Chu, Z. Xiang, K. Zhang, How sudden, intense energetic electron enhancements correlate with the innermost plasmapause locations under various solar wind drivers and geomagnetic conditions. J. Geophys. Res. **124**, 11 (2019). https://doi.org/10.1029/2019ja027412

H.-J. Kim, A.A. Chan, R.A. Wolf, J. Birn, Can substorms produce relativistic electrons? J. Geophys. Res. **105**(A4), 7721 (2000). https://doi.org/10.1029/199JA9000465

K.C. Kim, D.-Y. Lee, H.-J. Kim, L.R. Lyons, E.S. Lee, M.K. Ozturk, C.R. Choi, Numerical calculations of relativistic electron drift loss effect. J. Geophys. Res. **113**, A09212 (2008). https://doi.org/10.1029/2007JA013011

Kletzing et al., title – TBD (2020), this volume

D.J. Knipp, D.V. Pette, L.M. Kilcommons, T.L. Isaacs, A.A. Cruz, M.G. Mlynczak, L.A. Hunt, C.Y. Lin, Thermospheric nitric oxide response to shock-led storms. Space Weather **15**(2), 325–342 (2017). https://doi.org/10.1002/2016SW001567

G.F. Knoll, *Radiation Detection and Measurement*, 4th edn. (Wiley & Sons, Hoboken, 2010), p. 647

B.T. Kress, M.K. Hudson, M.D. Looper, J. Albert, J.G. Lyon, C.C. Goodrich, Global MHD test particle simulations of >10 MeV radiation belt electrons during storm sudden commencement. J. Geophys. Res. **112**, A09215 (2007). https://doi.org/10.1029/2006JA012218

B.T. Kress, M.K. Hudson, J. Paral, Rebuilding of the Earth's outer electron belt during 8-10 October 2012. Geophys. Res. Lett. (2014). https://doi.org/10.1002/2013gl058588

E.A. Kronberg, E.E. Grigorenko, D.L. Turner, P.W. Daly, Y. Khotyaintsev, L. Kozak, Comparing and contrasting dispersionless injections at geosynchronous orbit during a substorm event. J. Geophys. Res. Space Phys. **122**, 3 (2017). https://doi.org/10.1002/2016ja023551

S. Lejosne, B.S.R. Kunduri, D.L. Turner, F.S. Mozer, Energetic electron injections deep into the inner magnetosphere: a result of the subauroral polarization stream (SAPS) potential drop. Geophys. Res. Lett. **45**, 9 (2018). https://doi.org/10.1029/2018GL077969

J.S. Lew, Drift rate in a dipole field. J. Geophys. Res. **66**(9), 2681–2685 (1961). https://doi.org/10.1029/JZ066i009p02681

X. Li, I. Roth, M. Temerin, J. Wygant, M.K. Hudson, J.B. Blake, Simulation of the prompt energization and transport of radiation particles during the March 24, 1991 SSC. Geophys. Res. Lett. **20**(22), 2423–2426 (1993). https://doi.org/10.1029/93GL02701

X. Li, D.N. Baker, T.P. O'Brien, L. Xie, Q.G. Zong, Correlation between the inner edge of outer radiation belt electrons and the innermost plasmapause location. Geophys. Res. Lett. **33**, L14107 (2006). https://doi.org/10.1029/2006GL026294

W. Li, Y.Y. Shpritz, R.M. Thorne, Dynamic evolution of energetic outer zone electrons due to wave-particle interactions during storms. J. Geophys. Res. **112**, A10220 (2007). https://doi.org/10.1029/2007JA012368

X. Li, S. Palo, R. Kohnert, D. Gerhardt, L. Blum, Q. Schiller, D. Turner, W. Tu, N. Sheiko, C.S. Cooper, Colorado student space weather experiment: differential flux measurements of energetic particles in a highly inclined low Earth orbit, in *Dynamics of the Earth's Radiation Belts and Inner Magnetosphere*, ed. by D. Summers. Geophys. Monogr. Ser., vol. 199 (AGU, Washington, 2012), pp. 385–404. https://doi.org/10.1029/2012GM001313

X. Li et al., First results from CSSWE CubeSat: characteristics of relativistic electrons in the near-Earth environment during the October 2012 magnetic storms. J. Geophys. Res. Space Phys. **118**, 6489–6499 (2013). https://doi.org/10.1002/2013JA019342

Z. Li, M.K. Hudson, A.N. Jaynes, A.J. Boyd, D.M. Malaspina, S.A. Thaller, J.R. Wygant, M.G. Henderson, Modeling gradual diffusion changes in radiation belt electron phase space density for the March 2013 Van Allen Probes case study. J. Geophys. Res. **119**, 3 (2014). https://doi.org/10.1002/2014JA020359

Z. Li, M. Hudson, B. Kress, J. Paral, Three-dimensional test particle simulation of the 17-18 March 2013 CME shock-driven storm. Geophys. Res. Lett. **42**, 14 (2015a). https://doi.org/10.1002/2015gl064627

X. Li, R.S. Selesnick, D.N. Baker, A.N. Jaynes, S.G. Kanekal, Q. Schiller, L. Blum, J. Fennell, J.B. Blake, Upper limit on the inner radiation belt MeV electron intensity. J. Geophys. Res. Space Phys. **120**, 1215–1228 (2015b). https://doi.org/10.1002/2014JA020777

J. Li, B. Ni, Q. Ma, L. Xie et al., Formation of energetic electron butterfly distributions by magnetosonic waves via Landau resonance. Geophys. Res. Lett. **43**, 3009–3016 (2016a). https://doi.org/10.1002/2016GL067853

J. Li, J. Bortnik, R.M. Thorne, D.N. Baker et al., Ultrarelativistic electron butterfly distributions created by parallel acceleration due to magnetosonic waves. J. Geophys. Res. Space Phys. **121**, 3212–3222 (2016b). https://doi.org/10.1002/2016JA022370

W. Li, Q. Ma, R.M. Thorne, J. Bortnik, X.-J. Zhang, J. Li, D.N. Baker, G.D. Reeves, H.E. Spence, C.A. Kletzing, W.S. Kurth, G.B. Hospodarsky, J.B. Blake, J.F. Fennell, S.G. Claudepierre, S.G. Kanekal, V. Angelopoulos, J.C. Green, J. Goldstein, Radiation belt electron acceleration during the 17 March 2015 geomagnetic storm: observations and simulations. J. Geophys. Res. Space Phys. **121**(6), 5520–5536 (2016c). https://doi.org/10.1002/2016ja022400

Z. Li, M.K. Hudson, J. Paral, M. Wiltburger, D.L. Turner, Global ULF wave analysis of radial diffusion coefficients using a global MHD model for the 17 March 2015 storm. J. Geophys. Res. Space Phys. **121**(7), 6196 (2016d). https://doi.org/10.1002/2016ja022508

X. Li, D.N. Baker, H. Zhao, K. Zhang, A.N. Jaynes, Q. Schiller, S.G. Kanekal, J.B. Blake, M. Temerin, Radiation belt electron dynamics at low L (<4): Van Allen Probes era versus previous two solar cycles. J. Geophys. Res. Space Phys. **122**(5), 5224 (2017a). https://doi.org/10.1002/2017JA023924

X. Li et al., Measurement of electrons from albedo neutron decay and neutron density in near-Earth space. Nature **552**, 382–385 (2017b). https://doi.org/10.1038/nature24642

Z. Li, M. Hudson, M. Patel, M. Wiltberger, A.J. Boyd, D. Turner, ULF wave analysis and radial diffusion calculation using a global MHD model for the 17 March 2013 and 17 March 2015 storms. J. Geophys. Res. Space Phys. **122**, 7 (2017c). https://doi.org/10.1002/2016ja023846

X. Liu, W. Liu, J.B. Cao, H.S. Fu, J. Yu, X. Li, Dynamic plasmapause model based on THEMIS measurements. J. Geophys. Res. **120**, 10543 (2015). https://doi.org/10.1002/2015JA021801

S. Liu, Q. Yan, C. Yang, Q. Zhou, Z. He, Y. He, Z. Gao, F. Xiao, Quantifying extremely rapid flux enhancements of radiation belt relativistic electrons associated with radial diffusion. Geophys. Res. Lett. **45**, 3 (2018). https://doi.org/10.1002/2017gl076513

M.D. Looper, J.B. Blake, R.A. Mewaldt, Response of the inner radiation belt to the violent Sun-Earth connection events of October–November 2003. Geophys. Res. Lett. **32**, L03S06 (2005). https://doi.org/10.1029/2004GL021502

Q. Ma, W. Li, R.M. Thorne, Y. Nishimura, X.-J. Zhang, G.D. Reeves, C.A. Kletzing, W.S. Kurth, G.B. Hospodarsky, M.G. Henderson, H.E. Spence, D.N. Baker, J.B. Blake, J.F. Fennell, V. Angelopoulos, Simulation of energy-dependent electron diffusion processes in the Earth's outer radiation belt processes in the Earth's outer radiation belt. J. Geophys. Res. Space Phys. **121**, 5 (2016). https://doi.org/10.1002/2016ja022507

Q. Ma, W. Li, R.M. Thorne, J. Bortnik, G.D. Reeves, H.E. Spence, D.L. Turner, J.B. Blake, J.F. Fennell, S.G. Claudepierre, C.A. Kletzing, W.S. Kurth, G.B. Hospodarsky, D.N. Baker, Diffusive transport of several hundred keV electrons in the Earth's slot region. J. Geophys. Res. Space Phys. **122**, 10 (2017). https://doi.org/10.1002/2017ja024452

Q. Ma, W. Li, J. Bortnik, R.M. Thorne, X. Chu, L.G. Ozeke, G.D. Reeves, C.A. Kletzing, W.S. Kurth, G.B. Hospodarsky, M.J. Engebretson, H.E. Spence, D.N. Baker, J.B. Blake, J.F. Fennell, S.G. Claudepierre, Quantitative evaluation of radial diffusion and local acceleration processes during GEM challenge events. J. Geophys. Res. Space Phys. **123**, 3 (2018). https://doi.org/10.1002/2017ja025114

D.M. Malaspina, A.N. Jaynes, C. Boulé, J. Bortnik, S.A. Thaller, R.E. Ergun, C.A. Kletzing, J.R. Wygant, The distribution of plasmaspheric hiss wave power with respect to plasmapause location. Geophys. Res. Lett. **43**, 7878–7886 (2016). https://doi.org/10.1002/2016GL069982

I.R. Mann, L.G. Ozeke, How quickly, how deeply, and how strongly can dynamical outer boundary conditions impact Van Allen radiation belt morphology? J. Geophys. Res. Space Phys. **121**, 6 (2016). https://doi.org/10.1002/2016ja022647

I.R. Mann et al., The role of ultralow frequency waves in radiation belt dynamics, in *Dynamics of the Earth's Radiation Belts and Inner Magnetosphere*. Geophys. Monogr. Ser., vol. 199, pp. 69–91 (2012). https://doi.org/10.1029/2012GM001349

I.R. Mann, L.G. Ozeke, K.R. Murphy, S.G. Claudepierre, D.L. Turner, D.N. Baker, I.J. Rae, A. Kale, D.K. Milling, A.J. Boyd, H.E. Spence, G.D. Reeves, H.J. Singer, S. Dimitrakoudis, I.A. Daglis, F. Honary, Explaining the dynamics of the ultra-relativistic third Van Allen radiation belt. Nat. Phys. **12**, 10 (2016). https://doi.org/10.1038/nphys3799

Manweiler et al., The Van Allen Probes science operations. Space Sci. Rev. (2020), this volume

B.H. Mauk, N.J. Fox, S.G. Kanekal et al., Science objectives and rationale for the radiation belt storm probes mission. Space Sci. Rev. **179**, 3–27 (2013). https://doi.org/10.1007/s11214-012-9908-y

R.L. McPherron, The role of substorms in the generation of magnetic storms, in *Magnetic Storms*, ed. by B.T. Tsurutani, W.D. Gonzalez, Y. Kamide, J.K. Arballo. Geophysical Monographs, vol. 98 (American Geophysical Union, Washington, D.C., 1997), p. 131. https://doi.org/10.1029/GM098p0131

N.P. Meredith, R.B. Horne, S.A. Glauert, R.M. Thorne, D. Summers, J.M. Alber, R.R. Anderson, Energetic outer zone electronloss timescales during low geomagnetic activity. J. Geophys. Res. **111**, A05212 (2006). https://doi.org/10.1029/2005JA011516

R.M. Millan, R.M. Thorne, Review of radiation belt relativistic electron losses. J. Atmos. Sol.-Terr. Phys. **69**, 362 (2007). https://doi.org/10.1029/2004BK000104

M. Motoki et al., Precise measurements of atmospheric muon fluxes with the BESS spectrometer. Astropart. Phys. **19**, 113–126 (2003). https://doi.org/10.1016/S0927-6505(02)00195-0

T. Nagahama, A. Mizuno, Y. Miyoshi, T. Nakajima, D.N. Baker et al., Anomalously low column density of nitric oxide in the upper mesosphere and lower thermosphere associated with the absence of energetic electrons trapped in the radiation belt during 2014. (2020), in preparation

B. Ni, J. Bortnik, R.M. Thorne, Q. Ma, L. Chen, Resonant scattering and resultant pitch angle evolution of relativistic electrons by plasmaspheric hiss. J. Geophys. Res. **118**, 7740 (2013). https://doi.org/10.1029/2008GL034032

B. Ni, X. Cao, Z. Zou, C. Zhou, X. Gu, J. Bortnik, J. Zhang, S. Fu, Z. Zhao, R. Shi, L. Xie, Resonant scattering of outer zone relativistic electrons by multi-band EMIC waves and resultant electron loss timescales. J. Geophys. Res. Space Phys. **120**, 7357–7373 (2015). https://doi.org/10.1002/2015JA021466

B. Ni, M. Hua, R. Zhou, J. Yi, S. Fu, Competition between outer zone electron scattering by plasmaspheric hiss and magnetosonic waves. Geophys. Res. Lett. **44**, 3465–3474 (2017). https://doi.org/10.1002/2017GL072989

B. Ni, H. Huang, W. Zhang, X. Gu, H. Zhao, X. Li, D. Baker, S. Fu, Z. Xiang, X. Cao, Parametric sensitivity of the formation of reversed electron energy spectrum caused by plasmaspheric hiss. Geophys. Res. Lett. **46**(8), 4134–4143 (2019). https://doi.org/10.1029/2019GL082032

B. Ni, L. Yan, S. Fu, X. Gu, X. Cao, Z. Xiang, Y. Zhang, Distinct formation and evolution characteristics of outer radiation belt electron butterfly pitch angle distributions observed by Van Allen Probes. Geophys. Res. Lett. **47**, e2019GL086487 (2020). https://doi.org/10.1029/2019GL086487

T.P. O'Brien, S.G. Claudepierre, T.B. Guild, J.F. Fennell, D.L. Turner, J.B. Blake, J.H. Clemmons, J.L. Roeder, Inner zone and slot electron radial diffusion revisited. Geophys. Res. Lett. **43**, 14 (2016). https://doi.org/10.1002/2016gl069749

L. Olifer, I.R. Mann, S.K. Morley, L.G. Ozeke, D. Choi, On the role of last closed drift shell dynamics in driving fast losses and Van Allen radiation belt extinction. J. Geophys. Res. Space Phys. **123**(5), 3692–3703 (2018). https://doi.org/10.1029/2018ja025190

L. Olifer, I.R. Mann, L.G. Ozeke, I.J. Rae, S.K. Morley, On the relative strength of electric and magnetic ULF wave radial diffusion during the March 2015 geomagnetic storm. J. Geophys. Res. Space Phys. **124**, 4 (2019). https://doi.org/10.1029/2018ja026348

Y. Omura, Y.-K. Hsieh, J.C. Foster, P.J. Erickson, C.A. Kletzing, D.N. Baker, Cyclotron acceleration of relativistic electrons through Landau resonance with obliquely propagating whistler mode chorus emissions. J. Geophys. Res. Space Phys. **124**, 2795–2810 (2019). https://doi.org/10.1029/2018JA026374

L.G. Ozeke, I.R. Mann, K.R. Murphy, I.J. Rae, D.K. Milling, Analytic expressions for ULF wave radiation belt radial diffusion coefficients. J. Geophys. Res. Space Phys. **119**, 1587–1605 (2014). https://doi.org/10.1002/2013JA019204

L.G. Ozeke, I.R. Mann, K.R. Murphy, D.G. Sibeck, D.N. Baker, Ultra-relativistic radiation belt extinction and ULF wave radial diffusion: modeling the September 2014 extended dropout event. Geophys. Res. Lett. **44**, 2624–2633 (2017). https://doi.org/10.1002/2017GL072811

L.G. Ozeke, I.R. Mann, K.R. Murphy, A.W. Degeling, S.G. Claudepierre, H.E. Spence, Explaining the apparent impenetrable barrier to ultra-relativistic electrons in the outer Van Allen belt. Nat. Commun. **9**, 1 (2018). https://doi.org/10.1038/s41467-018-04162-3

L.G. Ozeke, I.R. Mann, S.G. Claudepierre, M. Henderson, S.K. Morley, K.R. Murphy, L. Olifer, H.E. Spence, D.N. Baker, The March 2015 superstorm revisited: phase space density profiles and fast ULF wave diffusive transport. J. Geophys. Res. Space Phys. **124**, 2 (2019). https://doi.org/10.1029/2018ja026326

L.G. Ozeke, I.R. Mann, S.K.Y. Dufresne, L. Olifer, S.K. Morley, S.G. Claudepierre, K.R. Murphy, H.E. Spence, D.N. Baker, A.W. Degeling, Rapid outer radiation belt flux dropouts and fast acceleration during the March 2015 and 2013 storms: the role of ULF wave transport from a dynamic outer boundary. J. Geophys. Res. Space Phys. **125**(2), e2019JA027179 (2020). https://doi.org/10.1029/2019ja027179

M. Patel, Z. Li, M. Hudson, S. Claudepierre, J. Wygant, Simulation of prompt acceleration of radiation belt electrons during the 16 July 2017 storm. Geophys. Res. Lett. **46**, 13 (2019). https://doi.org/10.1029/2019gl083257

V.A. Pinto, J. Bortnik, P.S. Moya, L.R. Lyons, D.G. Sibeck, S.G. Kanekal, D.N. Baker, Characteristics, occurrence, and decay rates of remnant belts associated with three-belt events in the Earth's radiation belts. Geophys. Res. Lett. **45**(22), 12–099 (2018)

G.D. Reeves, M. Henderson, The storm-substorm relationship: ion injections in geosynchronous measurements and composite energetic neutral atom images. J. Geophys. Res. **106**(A4), 5833 (2001). https://doi.org/10.1029/2000JA003017

G.D. Reeves et al., Electron acceleration in the heart of the Van Allen radiation belts. Science **341**, 991–994 (2013). https://doi.org/10.1126/science.1237743

G.D. Reeves, R.H.W. Friedel, B.A. Larsen, R.M. Skoug, H.O. Funsten, S.G. Claudepierre et al., Energy-dependent dynamics of keV to MeV electrons in the inner zone, outer zone, and slot regions. J. Geophys. Res. Space Phys. **121**, 397–412 (2016). https://doi.org/10.1002/2015JA021569

J. Ren et al., A comparative study of ULF waves' role in the dynamics of charged particles in the plasmasphere: Van Allen Probes observation. J. Geophys. Res. **123**, 7 (2018). https://doi.org/10.1029/2018ja025255

P. Riley, R.A. Wolf, Comparison of diffusion and particle drift descriptions of radial transport in the Earth's inner magnetosphere. J. Geophys. Res. **97**(A11), 16865 (1992). https://doi.org/10.1029/10.1029/92JA01538

J.F. Ripoll, G. Reeves, G. Cunningham, V. Loridan, M. Denton, O. Santolík, W.S. Kurth, C.A. Kletzing, D.L. Turner, M.G. Henderson, A.Y. Ukhorskiy, Reproducing the observed energy-dependent structure of Earth's electron radiation belts during storm recovery with an event-specific diffusion model. Geophys. Res. Lett. **43**(11), 5616–5625 (2016). https://doi.org/10.1002/2016gl068869

C.J. Rodger, D.L. Turner, M.A. Clilverd, A.T. Hendry, Magnetic local time-resolved examination of radiation belt dynamics during high speed solar wind speed-triggered substorm clusters. Geophys. Res. Lett. **46**, 17–18 (2019). https://doi.org/10.1029/2019gl083712

J.G. Roederer, *Dynamics of Geomagnetically Trapped Radiation* (Springer, Berlin, 1970). https://doi.org/10.1007/978-3-642-49300-3

T.E. Sarris, X. Li, M. Temerin, H. Zhao, S. Califf, W. Liu, R. Ergun, On the relationship between electron flux oscillations and ULF wave-driven radial transport. J. Geophys. Res. Space Phys. **122**, 9 (2017). https://doi.org/10.1002/2016ja023741

T.E. Sarris, X. Li, M. Temerin, H. Zhao, L.Y. Khoo, D.L. Turner et al., Simulations of electron flux oscillations as observed by MagEIS in response to broadband ULF waves. J. Geophys. Res. Space Phys. **125**, e2020JA027798 (2020). https://doi.org/10.1029/2020JA027798

Q. Schiller, W. Tu, A.F. Ali, X. Li, H.C. Godinez, D.L. Turner, S.K. Morley, M.G. Henderson, Simultaneous event-specific estimates of transport, loss, and source rates for relativistic outer radiation belt electrons. J. Geophys. Res. Space Phys. **122**, 3 (2017). https://doi.org/10.1002/2016ja023093

Q. Schiller, S.G. Kanekal, A.J. Boyd, L. Blum, A.D. Jones, D.N. Baker, J.B. Blake, On the cause of two prompt shock-induced relativistic electron depletion events. J. Atmos. Sol.-Terr. Phys. **177**, 208–217 (2018). https://doi.org/10.1016/j.jastp.2017.08.017

M. Schulz, L.J. Lanzerotti, *Particle Diffusion in the Radiation Belts*. Physics and Chemistry in Space, vol. 7 (Springer, New York, 1974). https://doi.org/10.1007/978-3-642-65675-0

R.S. Selesnick, J.M. Albert, Variability of the proton radiation belt. J. Geophys. Res. Space Phys. **124**, 5516 (2019). https://doi.org/10.1029/2019JA026754

R.S. Selesnick, J.B. Blake, On the source location of radiation belt relativistic electrons. J. Geophys. Res. Space Phys. **105**(A2), 2607–2624 (2000). https://doi.org/10.1029/1999JA900445

R.S. Selesnick, D.N. Baker, A.N. Jaynes, X. Li, S.G. Kanekal, M.K. Hudson, B.T. Kress, Observations of the inner radiation belt: CRAND and trapped solar protons. J. Geophys. Res. Space Phys. **119**, 6541–6552 (2014). https://doi.org/10.1002/2014JA020188

R.S. Selesnick, D.N. Baker, A.N. Jaynes, X. Li, S.G. Kanekal, M.K. Hudson, B.T. Kress, Inward diffusion and loss of radiation belt protons. J. Geophys. Res. Space Phys. **121**, 1969–1978 (2016). https://doi.org/10.1002/2015JA022154

R.S. Selesnick, D.N. Baker, S.G. Kanekal, Proton straggling in thick silicon detectors. Nucl. Instrum. Methods Phys. Res. B **394**, 145–152 (2017). https://doi.org/10.1016/j.nimb.2017.01.028

R.S. Selesnick, D.N. Baker, S.G. Kanekal, V.C. Hoxie, X. Li, Modeling the proton radiation belt with Van Allen Probes relativistic electron-proton telescope data. J. Geophys. Res. Space Phys. **123**, 685–697 (2018). https://doi.org/10.1002/2017JA024661

P.E. Sheese, R.L. Gattinger, E.J. Llewellyn, C.D. Boone, K. Strong, Nighttime nitric oxide densities in the Southern Hemisphere mesosphere–lower thermosphere. Geophys. Res. Lett. **38**(15), L15812 (2011). https://doi.org/10.1029/2011GL048054

Y. Shprits, A. Drozdov, M. Spasojevic et al., Wave-induced loss of ultra-relativistic electrons in the Van Allen radiation belts. Nat. Commun. **7**, 12883 (2016). https://doi.org/10.1038/ncomms12883

Skoug et al., title – TBD (2020), this volume

Z. Su, H. Zhu, F. Xiao, Q.G. Zong, X.Z. Zhou, H. Zheng, Y. Wang, S. Wang, Y.X. Hao, Z. Gao, Z. He, D.N. Baker, H.E. Spence, G.D. Reeves, J.B. Blake, J.R. Wygant, Ultra-low-frequency wave-driven diffusion of radiation belt relativistic electrons. Nat. Commun. **6**, 10096 (2015). https://doi.org/10.1038/ncomms10096

Z. Su, Z. Gao, H. Zheng, Y. Wang, S. Wang, H.E. Spence, G.D. Reeves, D.N. Baker, J.R. Wygant, Rapid loss of radiation belt relativistic electrons by EMIC waves. J. Geophys. Res. Space Phys. **122**, 10 (2017). https://doi.org/10.1002/2017ja024169

D. Summers, R.M. Thorne, Relativistic electron pitch angle scattering by electromagnetic ion cyclotron waves during geomagnetic storms. J. Geophys. Res. **108**(A4), 1143 (2003). https://doi.org/10.1029/2002JA009489

D. Summers, R.M. Thorne, F. Xiao, Relativistic theory of wave-particle resonant diffusion with application to electron acceleration in the magnetosphere. J. Geophys. Res. **103**, 20487 (1998). https://doi.org/10.1029/98JA01740

D. Summers, B. Ni, N.P. Meredith, Timescales for radiation belt electron acceleration and loss due to resonant wave-particle interactions: 2. Evaluation for VLF chorus, ELF hiss, and electromagnetic ion cyclotron waves. J. Geophys. Res. **112**, A04207 (2007). https://doi.org/10.1029/2006JA011993

C.-L. Tang, J. Zhang, G.D. Reeves, Z. Su, D.N. Baker, H.E. Spence, H.O. Funsten, J.B. Blake, J.R. Wygant, Prompt enhancement of the Earth's outer radiation belt due to substorm electron injections. J. Geophys. Res. Space Phys. **121**, 11,826–11,838 (2016). https://doi.org/10.1002/2016ja023550

C.L. Tang, X.J. Xie, B. Ni, Z.P. Su, G.D. Reeves, J.-C. Zhang, D.N. Baker, H.E. Spence, H.O. Funsten, J.B. Blake, J.R. Wygant, G.Y. Dai, Rapid enhancements of the seed populations in the heart of the Earth's outer radiation belt: a multicase study. J. Geophys. Res. Space Phys. **123**(6), 4895–4907 (2018). https://doi.org/10.1029/2017JA025142

C.-L. Tang, X.J. Xie, B. Ni, Z. Su, G.D. Reeves, J. Zhang, D.N. Baker, H.E. Spence, H.O. Funsten, J.B. Blake, Substorm electron injections in the Earth's outer radiation belt: a statistical study. J. Geophys. Res. (2020). https://doi.org/10.1029/2019GL084344. Submitted

M. Teramoto, T. Hori, S. Saito, Y. Miyoshi, S. Kurita, N. Higashio, A. Matsuoka, Y. Kasahara, Y. Kasaba, T. Takashima, R. Nomura, M. Nosé, A. Fujimoto, Y.M. Tanaka, M. Shoji, Y. Tsugawa, M. Shinohara, I. Shinohara, J.B. Blake, J.F. Fennell, S.G. Claudepierre, D.L. Turner, C.A. Kletzing, D. Sormakov, O. Troshichev, Remote detection of drift resonance between energetic electrons and ultralow frequency waves: multisatellite coordinated observation by Arase and Van Allen Probes. Geophys. Res. Lett. **46**, 21 (2019). https://doi.org/10.1029/2019gl084379

S.S. Tetrick et al., Location of intense electromagnetic ion cyclotron (EMIC) wave events relative to the plasmapause: Van Allen Probes observations. J. Geophys. Res. **122**, 4 (2017). https://doi.org/10.1002/2016ja023392

R.M. Thorne, A possible cause of dayside relativistic electron precipitation events. J. Atmos. Terr. Phys. **36**(4), 635–645 (1974). https://doi.org/10.1016/0021-9169(74)90087-7

R.M. Thorne, Radiation belt dynamics: The importance of wave-particle interactions. Geophys. Res. Lett. **37**, L22107 (2010). https://doi.org/10.1029/2010GL044990

R.M. Thorne, E.J. Smith, R.K. Burton, R.E. Holzer, Plasmaspheric hiss. J. Geophys. Res. **78**, 1581 (1973). https://doi.org/10.1029/JA078i010p01581

R.M. Thorne, W. Li, B. Ni, Q. Ma, J. Bortnik, D.N. Baker, H.E. Spence, G.D. Reeves, M.G. Henderson, C.A. Kletzing, W.S. Kurth, G.B. Hospodarsky, D. Turner, V. Angelopoulos, Evolution and slow decay of an unusual narrow ring of relativistic electrons near $L \sim 3.2$ following the September 2012 magnetic storm. Geophys. Res. Lett. **40**(1-5), 3507–3511 (2013a). https://doi.org/10.1002/grl.50627

R.M. Thorne, W. Li, B. Ni, Q. Ma, J. Bortnik, L. Chen, D.N. Baker, H.E. Spence, G. Reeves, M. Henderson, C. Kletzing, W. Kurth, G. Hospodasky, J. Blake, J. Fennell, S. Claudepierre, S.G. Kanekal, Rapid local acceleration of relativistic radiation belt electrons by magnetospheric chorus. Nature **504**(7480), 411–414 (2013b). https://doi.org/10.1038/nature12889

W. Tu, R. Selesnick, X. Li, M. Looper, Quantification of the precipitation loss of radiation belt electrons observed by SAMPEX. J. Geophys. Res. **115**, A07210 (2010). https://doi.org/10.1029/2009JA014949

W. Tu, Z. Xiang, S.K. Morley, Modeling the magnetopause shadowing loss during the June 2015 dropout event. Geophys. Res. Lett. **46**, 16 (2019). https://doi.org/10.1029/2019gl084419

D.L. Turner, A.Y. Ukhorskiy, Outer radiation belt losses by magnetopause incursions and outward radial transport: new insight and outstanding questions from the Van Allen Probes era, in *The Dynamic Loss of Earth's Radiation Belts* (Elsevier, Amsterdam, 2020), pp. 1–28

D.L. Turner, V. Angelopoulos, S.K. Morley, M.G. Henderson, G.D. Reeves, W. Li, D.N. Baker, S.G. Claudepierre, J.B. Blake, C.-L. Huang, A.J. Boyd, H.E. Spence, J.V. Rodriguez, On the cause and extent of outer radiation belt losses during the 30 September 2012 dropout event. J. Geophys. Res. (2014). https://doi.org/10.1002/2013JA019446

D.L. Turner, S.G. Claudepierre, J.F. Fennell, T.P. O'Brien, C.L. Lemon, M. Gkioulidou, G.D. Reeves, S.A. Thaller, A.W. Breneman, J.R. Wygant, W. Li, A. Runov, V. Angelopoulos, Energetic electron injections deep into the inner magnetosphere associated with substorm activity. Geophys. Res. Lett. **42**(7), 2079–2087 (2015). https://doi.org/10.1002/2015gl063225

D.L. Turner, J.F. Fennell, J.B. Blake, S.G. Claudepierre, J.H. Clemmons, A.N. Jaynes, T. Leonard, D.N. Baker, I.J. Cohen, M. Gkioulidou, A.Y. Ukhorskiy, B.H. Mauk, C. Gabrielse, V. Angelopoulos, R.J. Strangeway, C.A. Kletzing, O. Le Contel, H.E. Spence, R.B. Torbert, J.L. Burch, G.D. Reeves, Multipoint observations of energetic particle injections and substorm activity during a conjunction between Magnetospheric Multiscale (MMS) and Van Allen Probes. J. Geophys. Res. Space Phys. **122**, 11 (2017a). https://doi.org/10.1002/2017ja024554

D.L. Turner, T.P. O'Brien, J.F. Fennell, S.G. Claudepierre, J.B. Blake, A.N. Jaynes, D.N. Baker, S. Kanekal, M. Gkioulidou, M.G. Henderson, G.D. Reeves, Investigating the source of near-relativistic and relativistic electrons in Earth's inner radiation belt. J. Geophys. Res. Space Phys. **122**, 1 (2017b). https://doi.org/10.1002/2016ja023600

Ukhorskiy et al., title – TBD (2020), this volume

J.A. Van Allen, D.N. Baker, B.A. Randall, D.D. Sentman, The magnetosphere of Jupiter as observed with Pioneer 10: 1. Instrument and principal findings. J. Geophys. Res. **79**(25), 3559–3577 (1974). https://doi.org/10.1029/JA079i025p03559

J. Wygant, F. Mozer, M. Temerin, J. Blake, N. Maynard, H. Singer, M. Smiddy, Large amplitude electric and magnetic field signatures in the inner magnetosphere during injection of 15 MeV electron drift echoes. Geophys. Res. Lett. **21**, 1739–1742 (1994). https://doi.org/10.1029/94GL00375

Z. Xiang, W. Tu, X. Li, B. Ni, S.K. Morley, D.N. Baker, Understanding the mechanisms of radiation belt dropouts observed by Van Allen Probes. J. Geophys. Res. Space Phys. **122**(10), 9858–9879 (2017). https://doi.org/10.1002/2017ja024487

Z. Xiang, W. Tu, B. Ni, M.G. Henderson, X. Cao, A statistical survey of radiation belt dropouts observed by Van Allen Probes. Geophys. Res. Lett. **45**, 16 (2018). https://doi.org/10.1029/2018gl078907

Z. Xiang, X. Li, M.A. Temerin, B. Ni, H. Zhao, K. Zhang, L.Y. Khoo, On energetic electron dynamics during geomagnetic quiet times in Earth's inner radiation belt due to atmospheric collisional loss and Cosmic Ray Albedo Neutron Decay (CRAND) as a source. J. Geophys. Res. Space Phys. **125**, 2 (2020). https://doi.org/10.1029/2019JA027678

F. Xiao, C. Yang, Z. Su et al., Wave-driven butterfly distribution of Van Allen belt relativistic electrons. Nat. Commun. **6**, 8590 (2015). https://doi.org/10.1038/ncomms9590

J. Yu, L.Y. Li, J. Cui, J.B. Cao, J. Wang, Effect of low-harmonic magnetosonic waves on the radiation belt electrons inside the plasmasphere. J. Geophys. Res. **124**, 5 (2019). https://doi.org/10.1029/2018ja026328

Z. Yuan, X. Yu, S. Huang, D. Wang, H.O. Funsten, In situ observations of magnetosonic waves modulated by background plasma density. Geophys. Res. Lett. **44**, 15 (2017). https://doi.org/10.1002/2017gl074681

C. Yue, W. Li, Y. Nishimura, Q. Zong, Q. Ma, J. Bortnik, M.J. Nicolls, Rapid enhancement of low-energy ($<$100 eV) ion flux in response to interplanetary shocks based on two Van Allen Probes case studies: implications for source regions and heating mechanisms. J. Geophys. Res. Space Phys. **121**, 6430–6443 (2016). https://doi.org/10.1002/2016JA022808

X.J. Zhang, W. Li, R.M. Thorne, V. Angelopoulos, Q. Ma, J. Li, J. Bortnik, Y. Nishimura, L. Chen, D.N. Baker, G.D. Reeves, H.E. Spence, C.A. Kletzing, W.S. Kurth, G.B. Hospodarsky, J.B. Blake, J.F. Fennell, Physical mechanism causing rapid changes in ultra-relativistic electron pitch angle distributions right after a shock arrival: evaluation of an electron dropout event. J. Geophys. Res. Space Phys. **121**(9), 8300–8316 (2016). https://doi.org/10.1002/2016ja022517

X. Zhang, D. Mourenas, A.V. Artemyev, V. Angelopoulos, R.M. Thorne, Contemporaneous EMIC and whistler mode waves: observations and consequences for MeV electron loss. Geophys. Res. Lett. **44**, 8113–8121 (2017). https://doi.org/10.1002/2017GL073886

K. Zhang, X. Li, H. Zhao, Q. Schiller, L.-Y. Khoo, Z. Xiang et al., Cosmic Ray Albedo Neutron Decay (CRAND) as a source of inner belt electrons: energy spectrum study. Geophys. Res. Lett. **46**, 544–552 (2019). https://doi.org/10.1029/2018GL080887

H. Zhao, X. Li, J.B. Blake et al., Peculiar pitch angle distribution of relativistic electrons in the inner radiation belt and slot region. Geophys. Res. Lett. **41**, 2250–2257 (2014). https://doi.org/10.1002/2014GL059725

H. Zhao, D.N. Baker, A.N. Jaynes, X. Li, S.R. Elkington, S.G. Kanekal, H.E. Spence, A.J. Boyd, C.L. Huang, C. Forsyth, On the relation between radiation belt electrons and solar wind parameters/geomagnetic indices: dependence on the first adiabatic invariant and L*. J. Geophys. Res. Space Phys. **122**, 2 (2017). https://doi.org/10.1002/2016ja023658

H. Zhao, D.N. Baker, X. Li, A.N. Jaynes, S.G. Kanekal, The acceleration of ultrarelativistic electrons during a small to moderate storm of 21 April 2017. Geophys. Res. Lett. **45**, 12 (2018). https://doi.org/10.1029/2018gl078582

H. Zhao, D.N. Baker, X. Li, A.N. Jaynes, S.G. Kanekal, The effects of geomagnetic storms and solar wind conditions on the ultrarelativistic electron flux enhancements. J. Geophys. Res. Space Phys. **124**, 3 (2019). https://doi.org/10.1029/2018ja026257

H. Zhao, D.N. Baker, X. Li, D.M. Malaspina, A.N. Jaynes, S.G. Kanekal, On the acceleration mechanism of ultrarelativistic electrons in the center of the outer radiation belt: a statistical study. J. Geophys. Res. Space Phys. **124**, 11 (2019a). https://doi.org/10.1029/2019ja027111

H. Zhao, W.R. Johnston, D.N. Baker, X. Li, B. Ni, A.N. Jaynes et al., Characterization and evolution of radiation belt electron energy spectra based on the Van Allen Probes measurements. J. Geophys. Res. Space Phys. **124**, 4217 (2019b). https://doi.org/10.1029/2019JA026697

H. Zhao, B. Ni, X. Li, D.N. Baker, W.R. Johnston, W. Zhang et al., Plasmaspheric hiss waves generate a reversed energy spectrum of radiation belt electrons. Nat. Phys. **15**(4), 367–372 (2019c). https://doi.org/10.1038/s41567-018-0391-6

Q. Zong, Y. Hao, H. Zou, S. Fu, X. Zhou, J. Ren, L. Wang, C. Yuan, Z. Liu, X. Jia, L. Quan, Y. Liu, Y. Wang, Radial propagation of magnetospheric substorm-injected energetic electrons observed using a BD-IES instrument and Van Allen Probes. Sci. China Earth Sci. **59**, 7 (2016). https://doi.org/10.1007/s11430-016-0039-0

Authors and Affiliations

Daniel N. Baker[1] · Shrikanth G. Kanekal[2] · Vaughn Hoxie[1] · Xinlin Li[1] · Allison N. Jaynes[3] · Hong Zhao[4] · Scot R. Elkington[1] · John C. Foster[5] · Richard Selesnick[6] · Binbin Ni[7] · Harlan Spence[8] · Rachel Filwett[3]

✉ D.N. Baker
daniel.baker@lasp.colorado.edu

S.G. Kanekal
shrikanth.g.kanekal@nasa.gov

V. Hoxie
Vaughn.hoxie@lasp.colorado.edu

X. Li
Xinlin.Li@lasp.colorado.edu

A.N. Jaynes
allison-n-jaynes@uiowa.edu

H. Zhao
zzh0054@auburn.edu

S.R. Elkington
scot.elkington@lasp.colorado.edu

J.C. Foster
jcfoster@mit.edu

B. Ni
bbni@whu.edu.cn

H. Spence
Harlan.Spence@unh.edu

R. Filwett
rachael-filwett@uiowa.edu

[1] Laboratory for Atmospheric and Space Physics, University of Colorado Boulder, Boulder, CO, USA

[2] Heliospheric Physics Branch, Heliophysics Division, NASA Goddard Space Flight Center, Greenbelt, MD, USA

[3] Department of Physics & Astronomy, University of Iowa, Iowa City, IA, USA

[4] Department of Physics, Auburn University, Auburn, AL, USA

[5] Haystack Observatory, Massachusetts Institute of Technology, Westford, MA, USA

[6] Space Vehicles Directorate, Air Force Research Laboratory, Kirtland AFB, NM, USA

[7] Department of Space Physics, School of Electronic Information, Wuhan University, Wuhan, Hubei 430072, China

[8] Institute for the Study of Earth, Oceans, and Space, University of New Hampshire, Durham, NH, USA